



HAL
open science

Investigation of Low-Dimensional Supramolecular Architectures by Low-Temperature Scanning Tunneling Microscopy

Sylvain Clair

► **To cite this version:**

Sylvain Clair. Investigation of Low-Dimensional Supramolecular Architectures by Low-Temperature Scanning Tunneling Microscopy. Physics [physics]. Ecole Polytechnique Fédérale de Lausanne (EPFL), 2004. English. NNT: . tel-00353672

HAL Id: tel-00353672

<https://theses.hal.science/tel-00353672>

Submitted on 16 Jan 2009

HAL is a multi-disciplinary open access archive for the deposit and dissemination of scientific research documents, whether they are published or not. The documents may come from teaching and research institutions in France or abroad, or from public or private research centers.

L'archive ouverte pluridisciplinaire **HAL**, est destinée au dépôt et à la diffusion de documents scientifiques de niveau recherche, publiés ou non, émanant des établissements d'enseignement et de recherche français ou étrangers, des laboratoires publics ou privés.

INVESTIGATION OF LOW-DIMENSIONAL SUPRAMOLECULAR ARCHITECTURES BY LOW-TEMPERATURE SCANNING TUNNELING MICROSCOPY

THÈSE N° 3080 (2004)

PRÉSENTÉE À LA FACULTÉ SCIENCES DE BASE

Institut de physique des nanostructures

SECTION DE PHYSIQUE

ÉCOLE POLYTECHNIQUE FÉDÉRALE DE LAUSANNE

POUR L'OBTENTION DU GRADE DE DOCTEUR ÈS SCIENCES

par

Sylvain CLAIR

Ingénieur de l'École Centrale Paris, France

Dipl.-Ing. TU Wien, Autriche

et de nationalité française

acceptée sur proposition du jury:

Prof. J.V. Barth, directeur de thèse

Prof. H. Brune, président du jury

Prof. M. Grätzel, rapporteur

Prof. J. I. Pascual, rapporteur

Prof. L. Porte, rapporteur

Lausanne, EPFL

Octobre 2004

Abstract

In this thesis we report investigations on supramolecular architectures assembled at well-defined metal surfaces. Supramolecular chemistry is dedicated to the study and use of non-covalent interactions to build highly organized molecular arrangements, aiming ultimately at creating systems with tailored properties and useful functions. The adaptation of its powerful principles to fabricate molecular systems at surfaces has already been proven to be very promising; the extended possibilities for the choice of on the one hand molecules with defined size, shape, symmetry and function, and on the other hand substrates with controlled composition, symmetry and patterning allow for a quasi-infinite tuning of the structure and properties of the respective assemblies.

The Scanning Tunneling Microscope (STM) is a tool particularly efficient for the nanoscale elucidation of supramolecular systems at surfaces, simultaneously providing topographic and spectroscopic information at the single-atom level. In this regard, a new Low-Temperature STM (LT-STM) operational at temperatures in the range 5 to 400 K has been constructed. A detailed description of the instrument is provided and the demonstration of its exquisite performance represents a major achievement. In addition to local STM studies, complementary experiments were performed with a synchrotron radiation source using integral techniques, namely X-ray Absorption Spectroscopy (XAS) and X-ray Magnetic Circular Dichroism (XMCD).

We present results obtained with the linear organic linker 1,4-benzenedicarboxylic acid (terephthalic acid - TPA) on the Au(111), Cu(111) and Cu(100) surfaces. The three-dimensional design principles of supramolecular chemistry could be successfully adapted to these low-dimensional systems.

TPA molecules adsorbed on Au(111) organize in two-dimensional molecular sheets, wherein the typical one-dimensional hydrogen-bonded chain motif is found. We show that the inhomogeneities induced by the surface reconstruction can be used to examine the

response of the supramolecular self-assembly. In particular, variations in the hydrogen bond length of up to 20% are encountered. On Cu(111), a strict commensurability of the supramolecular sheet to the substrate is not possible because of the reduced lattice spacing of the latter, and the creation of defects is analyzed.

Due to their peculiar reactivity, the elbow sites of the reconstructed Au(111) surface act as nucleation centers in the epitaxial growth of transition metals (Fe, Co, Ni), leading to the formation of regular arrays of nanoscale metallic islands. We take advantage of this patterning to steer the formation of metallosupramolecular nano-architectures. Co-deposited TPA molecules attack both Fe and Co clusters and metal-carboxylate linkages evolve. Depending on the deposition parameters, nanoporous grids, mesoscopically organized stripes or truly one-dimensional linkages are obtained. Furthermore, the dynamics of the formation of the nanogrids are monitored *in situ*.

Finally, we report investigations of the magnetic and electronic properties of surface-supported coordination architectures by means of XAS and XMCD. We studied Fereterephthalate systems engineered on a Cu(100) substrate. Both mononuclear $\text{Fe}(\text{TPA})_4$ compounds and diiron centers structures in 2D Fe-TPA lattices exhibit a paramagnetic behavior. Moreover, we demonstrate the decisive influence of the ligand rather than the substrate on the electronic ground state of the metal centers, thus illustrating new vistas to effectively tailor the valence state and magnetic moment of transition metal atoms at surfaces.

⁰An electronic version of this thesis is available at <http://library.epfl.ch/theses/>

Version abrégée

Dans ce rapport de thèse nous présentons les résultats obtenus avec des architectures supramoléculaires assemblées sur des surfaces de monocristaux de métaux nobles. La chimie supramoléculaire est dédiée à l'étude et à l'utilisation d'interactions non covalentes pour la fabrication de systèmes hautement organisés, avec pour but ultime la création d'assemblages fonctionnalisés aux propriétés contrôlées. L'adaptation de ses principes productifs à des molécules sur des surfaces s'est déjà avérée être très prometteuse; l'étendue des possibilités pour le choix d'une part de molécules de taille, forme, symétrie et fonctionnalité bien définies, et d'autre part d'un substrat possédant une composition, une symétrie et une texturation données, permet de diriger la structure et les propriétés de tels ensembles.

Le microscope électronique à effet tunnel (STM) est un outil particulièrement bien adapté pour l'étude nanométrique de systèmes supramoléculaires sur des surfaces, puisqu'il procure à la fois des informations topographiques et spectroscopiques au niveau de l'atome unique. Nous avons donc entrepris la construction d'un nouveau microscope opérationnel dans la gamme de température 5 à 400 K (LT-STM). La description détaillée de l'instrument est fournie, et la démonstration de ses hautes performances représente un résultat important pour cette thèse. Parallèlement aux études à l'échelle moléculaire par STM, nous avons effectué des mesures complémentaires avec deux techniques utilisant une source de rayonnement synchrotron, la spectroscopie d'absorption des rayons X (XAS) et le dichroïsme circulaire magnétique des rayons X (XMCD).

Les résultats présentés ont été obtenus avec la molécule d'acide benzène-1,4-dicarboxylique (acide téréphtalique - TPA) sur les surfaces Au(111), Cu(111) et Cu(100). Les principes d'assemblage tridimensionnel de la chimie supramoléculaire ont pu être adaptés avec succès à ces systèmes de basse dimensionnalité.

Les molécules de TPA adsorbées sur Au(111) s'organisent en couches bidimension-

nelles dans lesquelles on retrouve le motif typique de liaison par chaîne unidimensionnelle. Nous montrons que les inhomogénéités dues à la reconstruction de surface peuvent être utilisées pour étudier la réponse de l'auto-assemblage supramoléculaire. En particulier, nous trouvons des variations de la longueur des liaisons hydrogène jusqu'à 20%. Sur la surface Cu(111), qui possède un paramètre de maille réduit par rapport à Au(111), la stricte commensurabilité de la couche supramoléculaire avec le substrat n'est pas réalisée, et la formation de défauts est analysée.

Dû à leur réactivité particulière, les coins de la reconstruction de la surface Au(111) agissent comme centres de nucléation pour la croissance épitaxiale de métaux de transition, ce qui mène pour de faibles taux de couverture à la formation de réseaux réguliers d'îlots métalliques nanométriques. Nous utilisons cette structuration de surface pour diriger la fabrication de nano-architectures métallosupramoléculaires. Les molécules de TPA codéposées attaquent les agrégats de Fe et de Co pour former des liaisons metal-carboxylate. En fonction des paramètres de dépôt nous contrôlons la fabrication de grilles nano-poreuses, de bandes mésoscopiques ordonnées, ou de lignes strictement unidimensionnelles. De plus, la dynamique de formation des nano-grilles est suivie *in situ*.

Dans une dernière partie nous présentons les premières caractérisations des propriétés magnétiques et électroniques d'architectures métallosupramoléculaires sur des surfaces par XAS et XMCD. Nous avons étudié des systèmes Fe-téréphtalate réalisés sur un substrat de Cu(100). Les composés mononucléaires $\text{Fe}(\text{TPA})_4$ ainsi que les structures en réseau 2D à deux centres de Fe sont paramagnétiques. De plus, nous démontrons l'influence décisive du ligand, par comparaison au substrat, sur l'état électronique fondamental des centres métalliques. Ce résultat ouvre la voie à une grande variété de possibilités pour contrôler efficacement l'état de valence et le moment magnétique d'atomes de métaux de transition sur des surfaces.

⁰Une version électronique de cette thèse est disponible à l'adresse <http://library.epfl.ch/theses/>

Table of Contents

Abstract	i
Version abrégée	iii
Introduction	1
1 Scanning Tunneling Microscopy	7
1.1 Principles	7
1.2 Theoretical description	10
1.2.1 Bardeen approach	10
1.2.2 Tersoff-Hamann formalism	11
1.2.3 Tunneling spectroscopy	12
1.3 Imaging adsorbed molecular species	15
2 Construction of a Low-Temperature Scanning Tunneling Microscope	19
2.1 General considerations - requirements	19
2.2 The vacuum chamber	21
2.2.1 Vacuum generation	21
2.2.2 The preparation chamber	23
2.3 The cryostat	27
2.4 The STM	31
2.4.1 Description	31
2.4.2 Wiring	35
2.4.3 Mechanical stability	36
2.4.4 The STM-control electronics - recording modes	38
2.5 STM test measurements	39

3 Self-Assembly of Terephthalic Acid with Epitaxial Stress: Response of the Hydrogen Bond	43
3.1 TPA on Au(111)	44
3.1.1 Description of the self-assembly	45
3.1.2 The Au(111) surface reconstruction	49
3.1.3 The 2D gas phase	57
3.2 TPA on Cu(111)	60
3.2.1 Description of the self-assembly	60
3.2.2 Dislocations in the molecular layer	63
4 Metallosupramolecular Nanoarchitectures	67
4.1 Mesoscopic patterning of the Au(111) surface by deposition of metallic impurities	69
4.2 Exploiting the Fe,Co/Au(111) template to monitor coordination reactions .	71
4.3 Metal-organic nano-texturing	79
5 Electronic and Magnetic State of Metal Centers in Surface-Supported Coordination Architectures	85
5.1 XAS and XMCD Spectroscopy	87
5.2 XAS/XMCD of Fe-TPA coordination compounds	92
5.2.1 Description of the structures	93
5.2.2 XAS investigations	95
5.2.3 XMCD investigations	96
Conclusions and Future Directions	103
Acknowledgements	107
Bibliography	109
Curriculum Vitae	123

Introduction

The properties of condensed matter on the atomic scale are quite different from those observed in everyday life. This has been known since the development of quantum mechanics at the beginning of the 20th century. In the last two decades however, technological progress has made it possible to substantially advance control of matter at the nanometer level. Scientists are now able to arrange atoms and molecules into (nano)structures of designed shape, size, and chemical composition. Equally important, the physical properties of such structures can be studied with unprecedented sensitivity, structural and chemical detail. The entire term nanoscience (and nanotechnology) designates investigations and use of objects with dimensions smaller than 100 nm and made out of a few (up to 10^6) atoms or molecules. With regard to the nature of the systems involved and the techniques used, nanotechnology is positioned at the cross-road between physics, material science, chemistry and biology, and is therefore accumulating experience from the synergetic expertise of these disciplines (see, e.g. [1,2]). In particular, supramolecular chemistry with its profusion of molecule-based compounds and processes constitute an appealing method for engineering novel functional nanosystems [3].

The whole field of surface and nanoscale science is able to provide precise and extensive analysis on the structural, chemical and electronic state of supramolecular architectures at well-defined surfaces. However, among the various tools available, Scanning Tunneling Microscopy (STM) provides a unique and detailed knowledge in real space of low-dimensional systems, in addition to spectroscopic information on a local scale. Moreover, a legion of recent studies attest to its value for the elucidation of fundamental phenomena in surface chemistry in exquisite detail: topology of supramolecular assemblies and molecular conformations [4–11], chiral specificity [5,12–14], pathways of chemical reactions [15–20], and catalytic functionality [21,22]. Notably, when supported by computational modeling, and employed in combination with powerful integral methods like X-ray absorption or

X-ray photoemission spectroscopy, an advanced understanding of molecular nanosystems can be gained.

In order to develop a rationale for molecular engineering in two dimensions, we need a comprehensive characterization of the coupling schemes of adsorbed complex molecules mediated by their functional groups, their bonding to the employed solid substrates, and the organization principles resulting from the balance of these interactions. This understanding will pave the way towards novel bottom-up strategies for the fabrication of supramolecular nanostructures potentially useful as novel materials in molecular electronics, magneto-recording devices, nano-templating, chemical sensing schemes, host-guest interactions or catalysis. A wide range of applications is envisioned, from nano-motors, nano-devices or nano-reactors, to computational systems based on the quantum properties of individual molecules, optical components with fluorescent molecules, nano-porous materials for gas storage or drug release, etc. In addition, there is a basic interest to study local elementary processes in chemistry or complex biological systems.

Molecular self-assembly relies on interactions between complex molecules containing specific functional groups. Self-assembly is abundant in nature, where the process is used to successfully create complex functional biological structures. The molecular level design of new materials by self-assembly expanded extensively in the past decades [23–26] under the banner of the multidisciplinary fields of crystal engineering [27–29] and supramolecular chemistry [3,30,31]. If molecules are built by connecting atoms with covalent bonds, supermolecules are assembled on the next level of complexity by binding molecules together with directional intermolecular interactions, non-covalent in nature. Supramolecular species are characterized by the spatial arrangement of their components, their functionality, and the nature of the intermolecular bonds that hold these components together. Various types of interactions may be distinguished, which present different degrees of strength, directionality, and dependence on distance and angles: metal-ligand coordination, electrostatic forces, hydrogen bonding, van der Waals interactions, donor-acceptor interactions, etc. Their strengths range from weak or moderate as in hydrogen bonds, to strong or very strong for metal-ligand coordination. Intermolecular forces are generally weaker than covalent bonds, so that supramolecular species are thermodynamically less stable, kinetically more labile and dynamically more flexible than molecules. Thus, supramolecular chemistry is concerned with soft bonds and represents a chemistry "beyond the molecule" [3].

Among the various driving forces governing molecular self-assembly, hydrogen bonding attracts particular interest. It is of pivotal importance in biological systems and in organic host-guest molecular complexes: structural aspects of DNA and DNA binding agents, protein conformations and folding, or receptor functions are examples where the natural chemistry of hydrogen bonding is extensively involved [31,32]. Of all directional intermolecular interactions, hydrogen bonding is the most important and versatile one. Three-dimensional structures may be readily and specifically assembled by hydrogen bonding, incorporating a large degree of flexibility due to weak intermolecular forces holding the molecules. As the interaction is weaker than covalent bonding and in the range of thermal energies at ambient conditions, it may be reversed - an intrinsic error correction mechanism is characteristic for hydrogen-bonded assemblies, which leads ultimately to the most thermodynamically favorable structures. An important feature encountered in hydrogen bonded architectures is cooperativity - being individually weak, together H-bonds become stronger, which enables non-covalent synthesis, based on the reversible formation of multiple hydrogen bonds to be accomplished. Hydrogen bonding is responsible for the determination of molecular conformation, molecular aggregation and functionality of a vast number of supramolecular systems [3,31,33,34]. At solid substrates, particularly on single crystal metal surfaces, hydrogen bonding was successfully explored to advance supramolecular engineering, where its directionality facilitates fabrication of highly organized assemblies [6,35–41]. Due to the great flexibility of this weak interaction, employing hydrogen bonding for the fabrication of surface-supported supramolecular architectures allows deliberate design of complex topologies with possible control over the final structures and functionalities [7].

Since the introduction of the coordination concept more than a century ago [42], the use of transition metal centers and coordination chemistry for directing the formation of complex structures has evolved into one of the most widely used strategies for organizing molecular building blocks into supramolecular architectures [3,31,43,44]. The predictable and directional bonding of organic ligands allows for the engineering of supramolecular coordination complexes with extraordinary structures and properties: rotaxanes and catenanes, synthetic receptors, molecular cages, as well as multicomponent assemblies such as chains, nanoporous networks or helices are already classical examples of coordination-driven self-assembly [31,45–50]. Solid state chemistry takes advantage of the coordination

bonding approach, since rational crystal engineering of solid materials is crucially dependent on predictability and rigidity - e.g., provided by organometallic compounds, where C-moieties of organic molecules couple to a metal [51, 52]. Transition metal complexes also play a tremendous role in catalysis. The mimics of enzymatic specificity in chemical asymmetric synthesis is tentatively approached by use of transition-metal-based catalysts [53], whereas supported metal-organic catalytic materials are expected to bridge the gap between homogeneous and heterogeneous catalysis, bringing the concepts and tools of chemistry to surface science [54, 55]. Molecular magnetism constitutes another promising facet of modern coordination chemistry and in recent years the field has produced magnificent solid-state structures with intriguing magnetic properties [56]. Coordination bonds may be decisive in molecular recognition and offer an excellent means for the fabrication of surface-supported complex molecular arrangements: however, their exploration for surface supramolecular chemistry is yet in its infancy [57–59].

In this thesis we investigated molecular nanosystems at well-defined metal surfaces. For this purpose, a Low-Temperature Scanning Tunneling Microscope (LT-STM) has been constructed, which provides nanoscale insight into supramolecular architectures. The samples were prepared *in situ* in Ultra High Vacuum (UHV) conditions in order to obtain atomically clean surfaces where a precise amount of material was deposited. The direct monitoring of the two-dimensional molecular organization allows for the elucidation of some of the key principles governing self-assembly at surfaces. The molecule used (figure 1) was chosen for its simple design and its ability to form hydrogen-bond-based synthons and metal-ligand coordination.

The present report is organized as follows:

Chapter 1 is a brief introduction to the main technique used, i.e., Scanning Tunneling Microscopy (STM). A theoretical approach based on the Bardeen approximation is described, which gives the required qualitative understanding for the interpretation of STM images and Scanning Tunneling Spectroscopy (STS). Additionally, the specific issue of imaging adsorbed molecular species is raised.

Chapter 2 presents the new experimental setup, a Low-Temperature STM (LT-STM) working in Ultra-High Vacuum (UHV). The design and the construction of this system has been achieved within the framework of the present thesis. For the investigations an

outstanding thermal and mechanical stability is required. To illustrate the performance obtained, data demonstrating atomic resolution of the Ag(100) surface is shown, and spectroscopic measurements on the surface states of the Au(111) surface are presented.

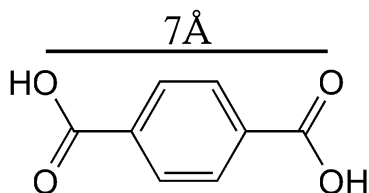


Figure 1: Molecular structure of Terephthalic Acid (TPA).

Chapter 3 details the two-dimensional self-assembly of the molecule 1,4-benzene-dicarboxylic acid (Terephthalic Acid - TPA, see figure 1) on the Au(111) and Cu(111) surfaces, which results from a subtle balance between intermolecular and molecule-surface interactions. The intermolecular attraction is mainly governed by a head-to-tail dimerization of the carboxyl groups by formation of hydrogen bonds. The molecule-surface interaction accounts for the commensurability of the supramolecular arrangement. As a consequence, the particular geometry of the substrate greatly influences the molecular superlattice. On Au(111) the surface reconstruction induces appreciable distortions in the molecular layer, in particular variations in the hydrogen bond length of up to 20%. On Cu(111), where the substrate lattice parameter is smaller but the molecular superlattice of the same symmetry, dislocations in the supramolecular sheet occur.

Chapter 4 gives insight into the intriguing engineering possibilities offered by metal-organic coordination on surfaces. TPA is deposited jointly with cobalt or iron on Au(111) and complexation occurs. The dynamics of this reaction are monitored *in situ*. The intrinsic square symmetry of the TPA-based metal-organic compounds is competing with the hexagonal symmetry of the substrate, leading to poorly ordered structures. However, by exploiting the patterning of the reconstructed Au(111) surface, mesoscopic texturing is achieved. Depending on the deposition parameters, various nano-architectures are obtained.

In chapter 5 the electronic structure and the magnetic properties of metal centers in surface-supported metal-organic networks are characterized for the first time. The use of X-ray Absorption Spectroscopy (XAS) and X-ray Magnetic Circular Dichroism (XMCD) allows unprecedented insight into the valence state and magnetic moment of the transition-metal ions. The decisive influence of the ligand rather than the substrate on their electronic ground state is demonstrated. The experiments presented were performed in the European Synchrotron Radiation Facility (ESRF) in Grenoble on Fe+TPA coordination compounds on the Cu(100) surface.

Chapter 1

Scanning Tunneling Microscopy

This chapter presents a basic introduction to Scanning Tunneling Microscopy (STM). This technique owes its immense success to its direct atomic scale imaging and manipulation capabilities coupled to the possibility of extracting information on the electronic structure of surfaces on a local scale. A theoretical approach based on the Bardeen approximation is described, which underlines the difficulty encountered when analyzing STM images, and reveals the relevant physical quantities governing Scanning Tunneling Spectroscopy (STS). In the following section the specific problem of adsorbate imaging is raised. For an overview of the STM capabilities see, e.g., Ref. [19, 60–64].

1.1 Principles

Scanning tunneling microscopy, invented by Binnig and Rohrer in 1982 [65], is a technique strongly related to classical electron tunneling experiments pioneered in the early sixties by Giaever and coworkers [66]. In both cases the quantity of interest is the electronic current I tunneling between two electrodes biased at a voltage V . The electrodes are separated by a thin insulating medium. The amount of current flowing for a given potential difference V depends on the density of electronic states (DOS) in the electrodes, and thus contains valuable information about the electronic structure of the surfaces of the electrodes. In classical planar tunnel junctions an oxide is mostly used as insulator, whereas a vacuum gap serves as tunnel barrier in STM. The gap can also consist of gaseous or liquid substances, e.g., air or electrolyte. In STM one electrode is tip shaped, i.e., microscopic, and can be positioned in three dimensions relative to the second electrode, contrary to

classical tunnel experiments where two static planar electrodes are used. Thus STM offers the advantage of performing spatially resolved tunneling experiments.

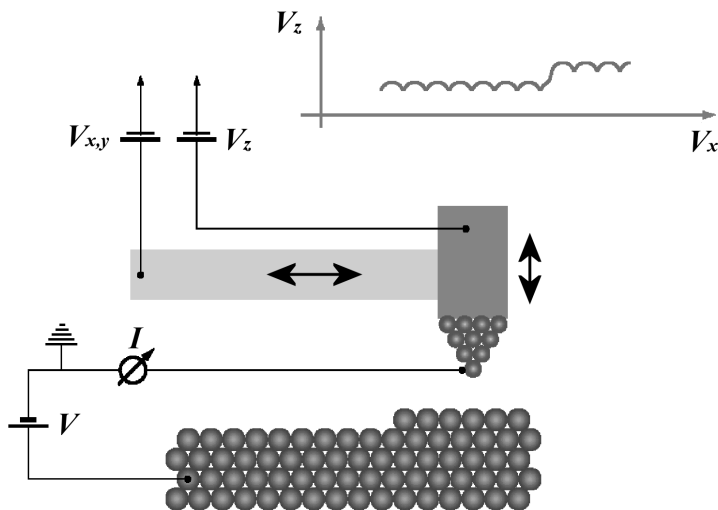


Figure 1.1: Schematic illustration of the basic principles of a Scanning Tunneling Microscope (STM). The voltages applied to piezoelectric materials allow for a fine horizontal ($V_{x,y}$) and vertical (V_z) positioning of a metallic tip relative to a conductive surface. If the tip is brought close enough to the biased sample (potential V) a tunneling current I is measured.

Figure 1.1 shows the schematics of a STM. A tip, normally a sharpened metallic wire, is brought close to the conducting surface of the sample. The lateral tip position (x and y directions) as well as the vertical (z) position relative to the sample are controlled with picometer precision by means of voltages applied to piezoelectric materials. If the tip is brought close enough to the sample (typically at about 5 - 10 Å) that the wave functions of the conduction electrons of tip and sample begin to overlap substantially, a measurable tunneling current I can flow between the biased sample (potential V) and the tip. The sign of V determines whether net tunneling occurs from the tip occupied states to the sample empty states (positive V) or vice-versa (figure 1.2).

Once the sample and the tip are brought in thermodynamical equilibrium, their chemical potentials equalize. The voltage V applied to the sample shifts its energy levels by $|eV|$ positively or negatively. Since states with the highest energy have the longest decay lengths into the vacuum, most of the tunneling current arises from electrons lying near the Fermi level of the negatively biased electrode.

The tunneling current I depends in first approximation exponentially on z (typically,

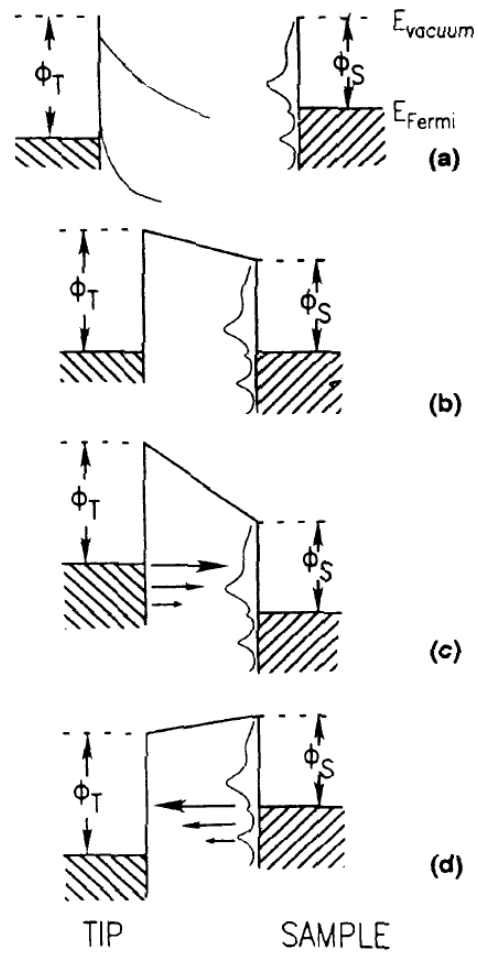


Figure 1.2: Energy level diagram of sample and tip (Φ_S and Φ_T are their respective work functions): (a) separated sample and tip; (b) sample and tip in thermal equilibrium, without applied voltage; (c) positive sample bias, electrons are tunneling from tip to sample; (d) negative sample bias, electrons are tunneling from sample to tip (from Ref. [61]).

a 1 Å displacement in z implies a ten-fold variation in I). The individual atoms or adsorbates of the sample surface give rise to substantial current variations as the tip is scanned in x and y . In the constant-current mode of operation the current I , which is typically in the range 0.1 – 5 nA for metal surfaces, is compared with a preset value I_0 in a feedback loop. The difference between I and I_0 is converted into a correction voltage and sent to the z transducer.

In this way the tunneling current is kept constant by approaching or withdrawing the tip from the sample. Recording the feedback signal as a function of the lateral tip position yields a three-dimensional (3D) map of the surface topography. More precisely $z(x, y)|_{I, V}$ represents a surface of constant local density of electron states (LDOS) of the sample at a given energy (in fact the integral of the LDOS from Fermi level to the energy considered is measured). This makes the interpretation of the data sometimes delicate, especially for non-metallic systems. A proper modeling of the tunneling process in a STM would require the knowledge of the 3D electron potential in the gap region between the tip and the sample, the description of the electronic states of both the sample and the tip, and the description of the spatial extension of the electron wave functions in the tunnel gap. The poor symmetry of the system, the unknown geometry of the tip, and tip-sample interactions make this task extremely difficult. Series of approximations are usually imposed to model the real system.

1.2 Theoretical description

1.2.1 Bardeen approach

In 1961 Bardeen proposed a formalism [67] for describing the planar geometry of the classical tunneling experiments, the so-called Hamiltonian approximation. By neglecting the interaction between the two separately described electrodes the tunneling current for weak wave function overlap is

$$I(V) = \frac{2\pi e}{\hbar} \sum_{\mu, \nu} |M_{\mu, \nu}|^2 \delta(E_\mu - eV - E_\nu) \times \left(f(E_\mu - eV, T) [1 - f(E_\nu, T)] - f(E_\nu, T) [1 - f(E_\mu - eV, T)] \right) \quad (1.1)$$

where the summation goes over all quantum eigenstates μ and ν of the independent electrodes; the eigenvalues E_μ and E_ν are given with respect to the (common) Fermi level; V is the applied voltage between the electrodes, $f(E, T)$ is the Fermi-Dirac distribution function and T is the temperature. The δ -function indicates that the tunneling electron transfer from one electrode to the other is an elastic process, whereas the Fermi-Dirac functions take into account that tunneling occurs from filled to unfilled states. In the limits of small voltage and temperature, Eq. (1.1) becomes

$$I = \frac{2\pi}{\hbar} e^2 V \sum_{\mu, \nu} |M_{\mu, \nu}|^2 \delta(E_\mu - E_F) \delta(E_\nu - E_F) \quad (1.2)$$

The matrix element $M_{\mu, \nu}$ represents the overlap in the gap region of the electrode wave functions and is given by the current density operator through a surface S lying entirely within the gap region:

$$M_{\mu, \nu} = -\frac{\hbar^2}{2m} \int_S d\vec{S} (\Psi_\mu^* \nabla \Psi_\nu - \Psi_\nu \nabla \Psi_\mu^*) \quad (1.3)$$

1.2.2 Tersoff-Hamann formalism

The planar geometry presented above is not well suited for describing a STM experiment where one of the electrodes is a tip. Tersoff and Hamann [68] proposed specific and more realistic wave functions for calculating the matrix element $M_{\mu, \nu}$.

The surface wave function Ψ_ν is described by a set of periodic surface plane wave functions decreasing exponentially in the normal direction (z):

$$\Psi_\nu = \Psi_{\vec{k}_\parallel, E}(\vec{r}) = \sum_{\vec{G}} a_{\vec{G}} \exp \left[-\sqrt{k^2 + (\vec{k}_\parallel + \vec{G})^2} \cdot z \right] \times \exp \left[i(\vec{k}_\parallel + \vec{G}) \cdot \vec{r}_\parallel \right] \quad (1.4)$$

where $k = \sqrt{\frac{2m\phi}{\hbar^2}}$ is the inverse decay length for the wave functions in vacuum, ϕ is the work function, \vec{k}_\parallel is the surface wave vector of the state, and \vec{G} is a surface reciprocal-lattice vector.

The tip is modeled as locally spherical with radius of curvature R . Its wave function is restricted to the asymptotic spherical form (s -wave)

$$\Psi_\mu = A_\mu \frac{e^{-k|\vec{r} - \vec{r}_0|}}{|\vec{r} - \vec{r}_0|} \quad (1.5)$$

where A_μ is a normalization constant, \vec{r}_0 is the position of the center of curvature of the tip and k is defined as above.

The matrix element (1.3) becomes then simply

$$M_{\mu,\nu} = -\frac{2\pi\hbar^2}{m} A_\mu \Psi_\nu(\vec{r}_0) \quad (1.6)$$

and the tunneling current (1.2) can be written as

$$I = \frac{e^2 V}{\hbar} \times \frac{(2\pi)^3 \hbar^4}{m^2} \sum_{\mu} |A_\mu|^2 \delta(E_\mu - E_F) \sum_{\nu} |\Psi_\nu(\vec{r}_0)|^2 \delta(E_\nu - E_F) \quad (1.7)$$

The relevant physical quantities here are

$$\rho_t(E_F) = \sum_{\mu} |A_\mu|^2 \delta(E_\mu - E_F) \quad (1.8)$$

the density of states of the tip at the Fermi level, and

$$\rho_s(\vec{r}_0, E_F) = \sum_{\nu} |\Psi_\nu(\vec{r}_0)|^2 \delta(E_\nu - E_F) \quad (1.9)$$

the local density of states (LDOS) of the (unperturbed) surface at the Fermi level measured at the center of curvature of the tip.

Consequently the tunneling current is:

$$I = \frac{e^2 V}{\hbar} \beta \rho_s(\vec{r}_0, E_F) \rho_t(E_F) \quad (1.10)$$

where β is a constant.

This model is only valid in the limit of low temperature and bias voltage and for a weak coupling between the electrodes, but shows that in first approximation constant-current STM topographs can be simply interpreted as contours of constant $\rho_s(E_F)$, the LDOS of the surface at the Fermi level.

1.2.3 Tunneling spectroscopy

The expression (1.10) derived by Tersoff and Hamman can be extended for higher voltage levels (but in the limits of V small in comparison with the electrode work function) [69, 70]:

$$I = \frac{e^2 V}{\hbar} \beta \int_{E_F}^{E_F + eV} dE \rho_s(\vec{r}_0, E) T(E, V, z) \rho_t(E - eV) \quad (1.11)$$

with the transmission coefficient $T(E, V, z)$ corresponding to a correcting factor accounting for the voltage drop in the vacuum region disregarding its k_{\parallel} dependence. The sample

LDOS $\rho_s(\vec{r}_{\parallel}, E)$ is taken in the surface plane right under the tip. The vertical dependence $T(E, V, z)$ is evaluated as

$$T(E, V, z) = \exp\left(-2z\sqrt{\frac{2m\bar{\Phi}}{\hbar^2}}\right) \quad (1.12)$$

with the mean barrier height being

$$\bar{\Phi} = \frac{\Phi_t + \Phi_s}{2} + \frac{eV}{2} - E \quad (1.13)$$

Equation (1.11) shows that all electronic states of energy between E_F and $E_F + eV$ are contributing to the tunneling current with varying weight. It is however possible in first approximation to extract the surface LDOS from $I(V)$.

By taking the derivative of the tunneling current (1.11) with respect to the voltage, one obtains:

$$\begin{aligned} \frac{dI}{dV} &\propto \rho_s(\vec{r}_{\parallel}, E_F + eV) T(E_F + eV, V, z) \rho_t(E_F) \\ &+ \int_{E_F}^{E_F + eV} dE \rho_s(\vec{r}_{\parallel}, E) \frac{dT(E, V, z)}{dV} \rho_t(E - eV) \\ &- e \int_{E_F}^{E_F + eV} dE \rho_s(\vec{r}_{\parallel}, E) T(E, V, z) \frac{d\rho_t(E - eV)}{dV} \end{aligned} \quad (1.14)$$

For a tip of "flat" density of states ($\rho_t(E) = \text{const.}$) we find

$$\begin{aligned} \frac{dI}{dV} &\propto \rho_s(\vec{r}_{\parallel}, E_F + eV) T(E_F + eV, V, z) \rho_t(E_F) \\ &+ \int_{E_F}^{E_F + eV} dE \rho_s(\vec{r}_{\parallel}, E) \frac{dT(E, V, z)}{dV} \rho_t(E - eV) \end{aligned} \quad (1.15)$$

The second term in equation (1.15) is negligible for small tunnel voltages or induces only small shifts in the position of the surface electronic states [69, 71], so we can write as a good approximation:

$$\frac{dI}{dV} \propto \rho_s(\vec{r}_{\parallel}, E_F + eV) T(E_F + eV, V, z) \quad (1.16)$$

The differential tunneling conductance is proportional to the local density of states for a transmission coefficient varying slowly with V .

Thermal broadening

At finite temperature the electronic state occupancies are modulated by the Fermi-Dirac function $f(E, T)$:

$$I \propto \int_{-\infty}^{+\infty} dE \rho_s(\vec{r}_{\parallel}, E) T(E, V, z) \rho_t(E - eV) f(E - eV, T_t) [1 - f(E, T_s)] \quad (1.17)$$

where the integral is now taken over an infinite energy range, and T_s and T_t are the temperatures of the sample and of the tip, respectively. In fact this is equivalent to Eq. (1.11), where in the limit of small temperature the Fermi-Dirac function is approximated as a step function.

Following the approximations leading to Eq. (1.16), the differential tunneling conductance is now

$$\frac{dI}{dV} \propto \int_{-\infty}^{+\infty} dE \frac{-df(E - eV, T_t)}{dV} \rho_s(\vec{r}_{\parallel}, E) T(E, V, z) \quad (1.18)$$

The function $\frac{-df(E - eV, T_t)}{dV}$ is similar to a Gaussian function with a full width at half maximum of about $3.5 k_B T$ [72] (where k_B is the Boltzmann constant).

This result shows that, within the Tersoff and Hamann approximations, a STS spectrum at finite temperature results from the convolution of the sample LDOS with a Gaussian function. At room temperature the broadening amounts to 90 meV and can be very limitative for studying particular electronic features. Note that in this formalism, where we consider a tip DOS without any energy dependent feature, the temperature of the tip is the relevant parameter. To increase substantially the spectroscopic resolution, it is thus necessary to cool down the STM, and especially the tip, to low temperature.

1.3 Imaging adsorbed molecular species

The interplay of topography and electronic structure becomes crucial when interpreting STM data obtained on molecular adsorbates. A well-known counterintuitive example is atomic oxygen chemisorbed on a metal surface, which appears as a depression in STM images even if the atom is positioned above the metal surface layer [15]. STM patterns of molecules often show internal structure and details but the interpretation is not straightforward due to the fact that protrusions on the STM image do not necessarily represent actual lateral position of atoms.

Before the first successful STM experiments with clearly resolved organic molecules were reported [73–75] it appeared questionable whether insulating molecules can be imaged by STM at all. As stated above, the tunneling current is proportional to the sample LDOS near the Fermi level E_F within the framework of the transfer Hamiltonian theory of STM. Most organic molecules have a large energy gap between the highest occupied (HOMO) and the lowest unoccupied (LUMO) molecular orbitals. If physisorbed on a metal surface, the molecule-related states are usually far away from the substrate Fermi energy. The HOMO- and LUMO- derived resonances are typically several eV below and above E_F , respectively. Therefore, the molecules contribution to the LDOS near E_F is rather small and at first glance one might expect organic molecules to be transparent for tunneling electrons at low bias voltage.

These considerations are of general importance for the imaging of molecules adsorbed on metal surfaces. Non-resonant tunneling occurs and the contribution of the adsorbate to the current comes from tails of molecular orbital resonances crossing the Fermi level. The DOS associated with these tails are usually rather small at the Fermi level, which explains why contributions from the substrate itself cannot be neglected, despite the appreciable difference in geometric height.

To interpret STM images of molecules the electronic structure of the adsorbate-substrate system can be calculated, whereby various levels of approximation are used ranging from Hückel calculations to first-principles self-consistent methods based mainly on the density functional theory (DFT). Again, the tunneling current is frequently reduced to the LDOS of the sample at the Fermi energy. In this approach the tip and the surface are treated separately, which neglects any interaction between them and is valid only in the limit of large tip-surface distances (similarly to the Tersoff-Hamann model,

where the electrodes are treated separately and the result is derived for small voltages, cf. section 1.2.2). Secondly, a severe approximation is made to the structure of the tip apex and any tip dependence of the image is lost. This can be accounted for by regarding p and d states as tip orbitals [76] or by describing the tip apex by a cluster of a small number of atoms [77, 78].

Another approach is the proper description of the interaction between sample and tip with a scattering theory formalism. The influence of tip-sample interactions becomes apparent in the imaging of adsorbed alkali metal atoms. Although they are known to substantially increase the LDOS at E_F , they are frequently transparent in STM data [79]. The basic idea of the scattering theory formalism is to consider the tunnel gap as a two-dimensional defect inserted between two semi-infinite periodic systems. The tunneling event is then viewed as a scattering process. An example is the electron scattering quantum chemical (ESQC) approach developed by Sautet and Joachim [80]. The tunnel junction is modeled by the approach of substrate and tip semi-infinite bulk solids. The adsorbate is chemisorbed on the substrate surface, while the tip apex, attached to the second semi-infinite solid, is modeled by a cluster of 1-15 atoms. Coupling with the tip and substrate electron reservoirs is hence fully taken into account.

Aromatic molecules represent an important group of adsorbates. Notably they can bear functional groups that can be exploited for building diverse molecular nanostructures at surfaces. Benzene was the first molecule of this class to be successfully imaged on a surface by high resolution STM: coadsorbed with CO on Rh(111) [74], benzene molecules, which are bound at threefold substrate hollow sites as determined by LEED [81], appear as three lobes forming a triangle in STM topographs. The lobes are located near the center of C-C bonds, in between underlying Rh substrate atoms as evidenced by ESQC [82]: the molecule appears to have 3-fold symmetry because molecular orbitals are hybridized with the rhodium substrate atoms below. As a consequence the STM image of benzene on a close-packed transition metal surface does not show positions of molecular C atoms but specific C-C bonds.

High-resolution STM studies, combined with calculations of LUMO and HOMO, were performed with more complex aromatic species in the early 90's. Particularly, a comparative study of naphthalene ($C_{10}H_8$) and azulene ($C_{10}H_8$) adsorption on Pt(111) demonstrates that a simple calculation methodology based on extended Hückel molecular orbital

theory adequately predicts details of internal structure [83]. Electron and hole density plots show very good agreement with the actual STM data and enable the reliable identification of molecular species.

A detailed description of several theoretical approaches to the contrast mechanism of adsorbate imaging with the scanning tunneling microscope is given in a review article by Sautet [84].

Chapter 2

Construction of a Low-Temperature Scanning Tunneling Microscope

The experimental setup that has been developed and built up in the framework of the present thesis is shown in figure 2.1. The motivation for constructing a new setup was to obtain a Scanning Tunneling Microscope (STM) working in Ultra High Vacuum (UHV) at variable temperature (in the range 5 to 400 K) with outstanding thermal and mechanical stability.

Since the discovery of STM by Binnig and Rohrer in 1982 [65] and the first developments of low temperature STM [85–87], several home-built low temperature microscopes (LT-STM) were realized (see, e.g., [88–93]). The setup presented here is mostly inspired from the work of Meyer [94], which has been commercialized [95] after the beginning of this thesis.

2.1 General considerations - requirements

A Scanning Tunneling Microscope is a tool designed for observation and manipulation of surfaces at the atomic scale. To achieve this goal, a supreme control of the conditions and the environment of the sample studied at this scale is required. The tip is positioned from 5 to 10 Å above the sample surface with a precision lower than 0.01 Å due to the exponential $I(z)$ characteristics, and laterally the position control must be a mere fraction of the interatomic spacing, which is for crystal surfaces typically around 3 Å.

The main challenge is to get rid of most of external noise. Mechanical noise comes

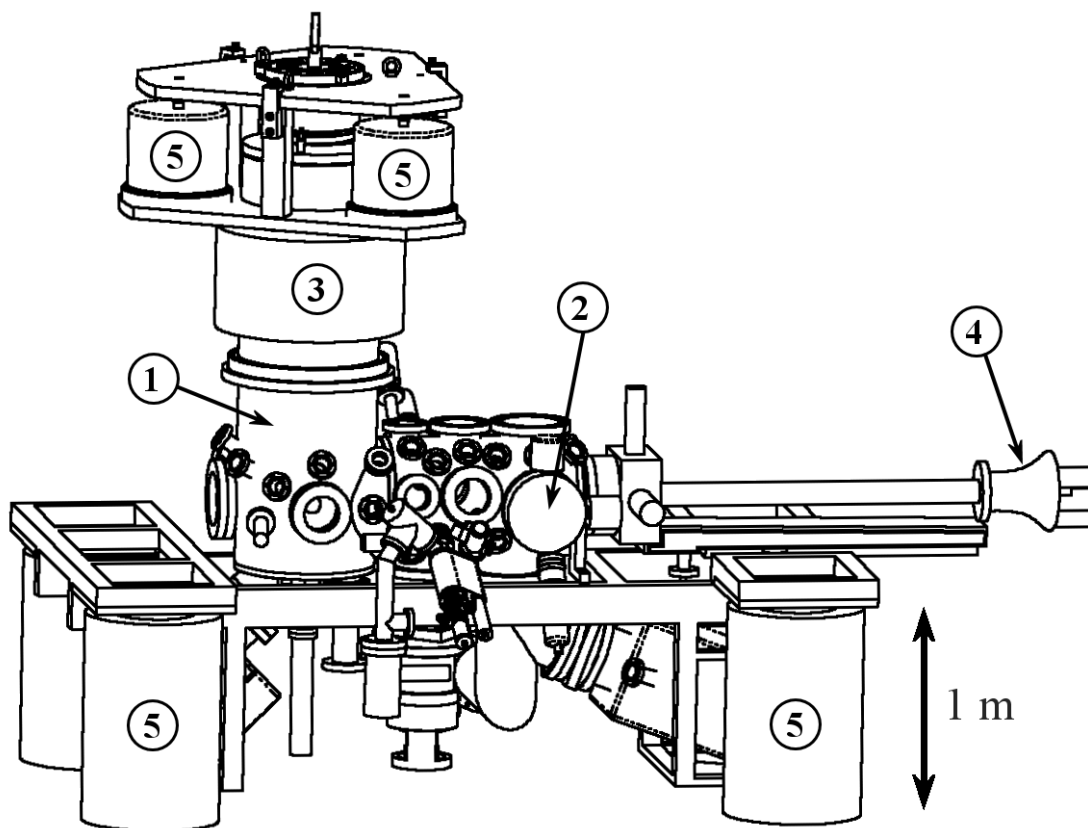


Figure 2.1: Global view of the experimental setup: (1) STM chamber, (2) Preparation chamber, (3) He bath cryostat, (4) He flux cryostat (manipulator), (5) Suspension legs. Model made with *Solidworks* [96].

from vibrations of the building as well as acoustic waves in the laboratory. Electrical noise comes from all the electromagnetic perturbations generated by the power supply network and other electronic instruments. Pneumatic suspension legs represent a good way to insulate the system from mechanical disturbances (Fig. 2.1). The whole apparatus is held on four suspension legs [97], and the entire bath cryostat sits on three more legs [98]. The STM itself is suspended by springs, and all the different parts were designed so as to make the assembly as rigid as possible. The vibration eigenfrequencies are in this manner shifted to high values and resonance phenomena are diminished.

Electromagnetical insulation is delicate. The wires transporting critical signals (tunneling current, z signal, sample bias) are carefully shielded (coaxial wires). In addition, the tunneling current signal is amplified and filtered at the exit of the vacuum chamber.

Experimenting in a vacuum chamber is an accurate way to get good control of the

sample environment, even if STM studies are also possible in air or in a liquid. The sample preparation is made *in situ* in such a way as to obtain an atomically clean and crystallographically well-defined surface where a precise amount of material can be deposited. Many complementary analysis methods are available, using electron (LEED, Auger Spectroscopy, ...) or photon (XPS, IR-spectroscopy, ...) beams.

Working at cryogenic temperature is very advantageous in terms of stability and resolution in comparison with room temperature where the surface mobility is high, thermal drift is non negligible and where the electronic properties are broadened [99, 100]. Controlled temperature allows furthermore qualitative and quantitative access to the various temperature dependent phenomena that take place on a surface, like diffusion, chemical reaction, or structural, electronic or magnetic transitions (superconductive state, charge density waves, ferro/antiferromagnetic transition, etc...).

Simultaneous achievement of on the one hand the mechanical decoupling required for the stability and on the other hand the thermal coupling required to reach low temperatures is in many ways impossible. Furthermore, the materials at disposal are restricted to UHV-compatible ones. The solutions retained are the result of a series of compromises.

2.2 The vacuum chamber

2.2.1 Vacuum generation

The vacuum chamber manufactured by the company *VAb* [101] is divided into two parts (see figure 2.2): the preparation chamber, which consists in a horizontal cylinder 300 mm in diameter, and the STM chamber, a vertical cylinder 350 mm in diameter. The two parts are separated by a gate valve welded in the chamber. By closing this valve, the sample preparation can be performed without contaminating the STM chamber, where the cold STM and bath cryostat represent very efficient cold traps.

The pumping system

The whole chamber is pumped by a 340 L/s turbomolecular pump (TMP) with magnetic suspension [102]. In the ultra-high vacuum (UHV) regime, this pump can be turned off to eliminate the (actually negligible) vibrations induced by its rotation mechanism,

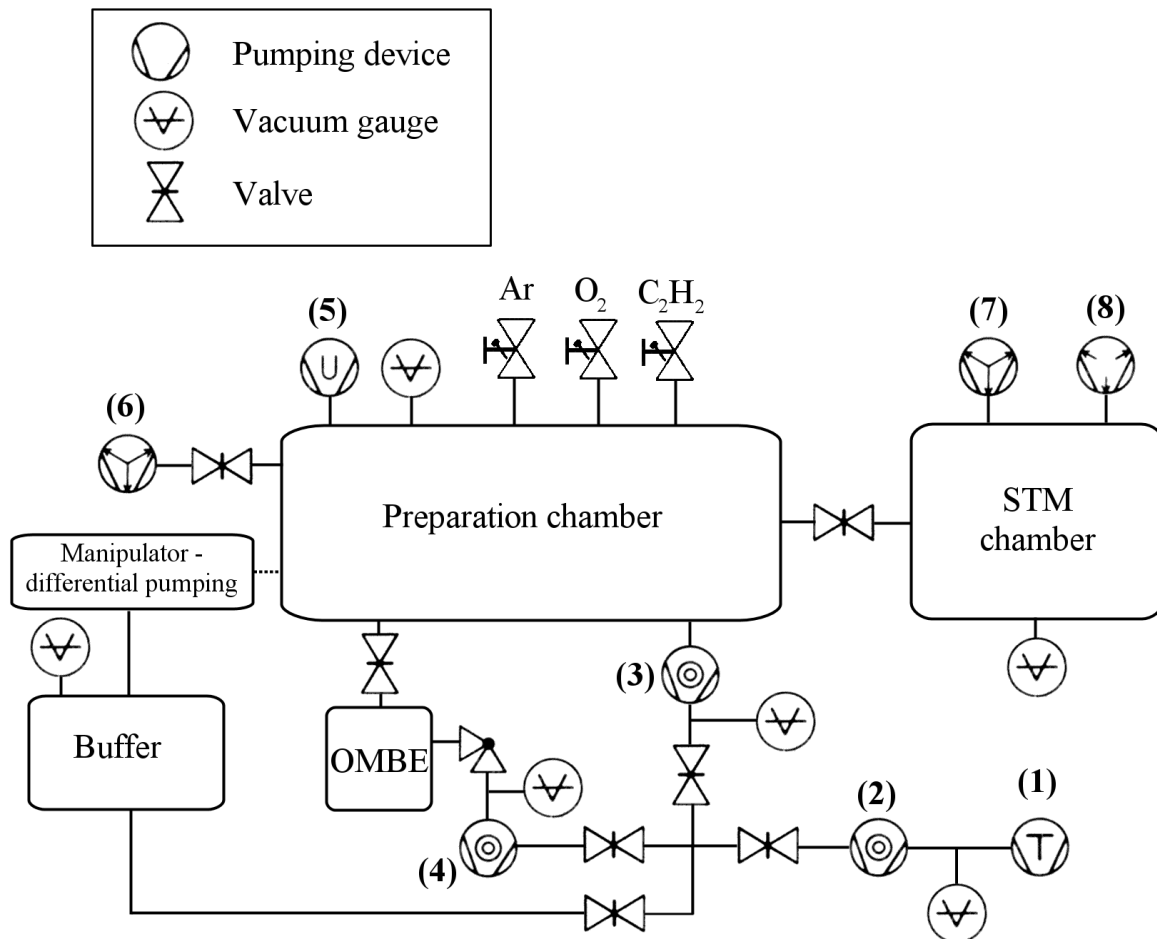


Figure 2.2: Schematic representation of the vacuum system. Pumping devices: (1) Compression piston pump, (2) Turbomolecular pump (TMP, 50 L/s), (3) Main TMP (340 L/s), (4) TMP for the OMBE chamber (50 L/s), (5) Titanium sublimation pump, (6) and (7) Ion pumps (resp. 270 and 200 L/s), (8) NEG pump.

the pumping being in this case provided by two ion pumps, one at each chamber. To increase the pumping capacity, a titanium sublimation pump (TSP) in the preparation chamber and a non-evaporable getter (NEG) pump [103] in the STM chamber are installed. Pressures down to 1×10^{-10} mbar have been reached with this design. The pressure even falls down when using the cryostat, as the large surface of the cold parts acts as a very efficient cryo pump. It is thus believed that an excellent vacuum (well below 10^{-10} mbar) is reached in the confined region of the sample and the STM in this case. Pressures in the UHV parts are measured with two cold-cathode (Penning) gauges.

The forevacuum stage consists of a small 50 L/s turbomolecular pump in series with an oil-free compression piston primary pump. A vacuum buffer of approximately 15 L has been designed between this stage and the main turbomolecular pump. This allows to shut down the primary pump, as it is the largest vibrational noise producing device, while the main TMP is still working and ejecting the pumped gas into the buffer for a certain time (up to 24 hours). The preparation of the next sample is in this way immediately possible after a short STM measurement.

2.2.2 The preparation chamber

Instrumentation

The preparation chamber includes many flanges for installing various instruments and future developments. Up to now, following devices are used:

An ion gun allows for bombarding the sample surface with argon ions of 500 to 1000 eV kinetic energy in order to sputter out the first monolayers of the surface and therefore remove the impurities. It requires an argon pressure of about 5×10^{-6} mbar in the chamber. The gate valve to the STM chamber is closed during sputtering to avoid contamination. A burst of titanium sublimation is usually performed just before operation in order to purify the noble gas which is not pumped by titanium.

The Organic Molecular Beam Epitaxy (OMBE) source consists of a stainless-steel crucible filled with the molecules to deposit (usually in powder form) and heated to some hundreds of degrees (the sublimation temperature of the molecule), depending on the material. In certain cases, it is necessary to use a gold-coated or a glass crucible

in order to avoid catalytic cracking of the molecules before they sublime. The source contains two independent crucibles, is retractable and possesses an independent pumping system so that it is possible to vent it, change the material, and pump it down again without breaking the vacuum inside the main chamber.

An e-beam Molecular Beam Epitaxy (MBE) evaporator [104] is used for the deposition of a precise amount of a metal species. This device is only suitable for certain materials with high melting point, like Fe or Co. The material to deposit is in the form of a metal rod, which is heated up by bombarding with an electron beam of typically a few mA at an energy of up to 1 keV. This leads to the evaporation of minute quantities from the top end of the rod.

Variable-leak valves allow admission of a controlled quantity (pressure) of gas for the sample preparation or the study of its adsorption and reaction with the sample surface.

The Low Energy Electron Diffractometer (LEED) is a surface analysis tool to investigate surface crystallographic structures. It is a simple and quick method to determine whether the sample surface is clean and well defined (i.e., well prepared) and whether material has been deposited on it or not. Identification of adsorbate superstructures are similarly possible.

A depot consisting of a linear feedthrough normal to the manipulator axis is included in the STM chamber. It contains up to four samples in their sample holders. A fifth place is kept for the tip changing tool (see figure 2.9). Two STM tip holders with their tips are also stored in the depot.

A load-lock for a rapid exchange of samples and tips without breaking the vacuum has been recently installed [105]. It can hold one sample and up to three tips.

Future implementations are planned allowing for example *in situ* irradiation of the sample for the study of light-induced processes, or *in situ* deposition of metal species.

The sample holder

The manipulator (see Fig. 2.1) provides translational (600 mm along the chamber axis, ± 25 mm in the two other directions) and rotational mobility (360°) to position and transfer the sample to the different preparation and measuring locations, as well as a precise control of the sample temperature in the range 40-1400 K. The rotary feedthrough requires a differential pumping which is obtained by a connection with the vacuum buffer (Fig. 2.2).

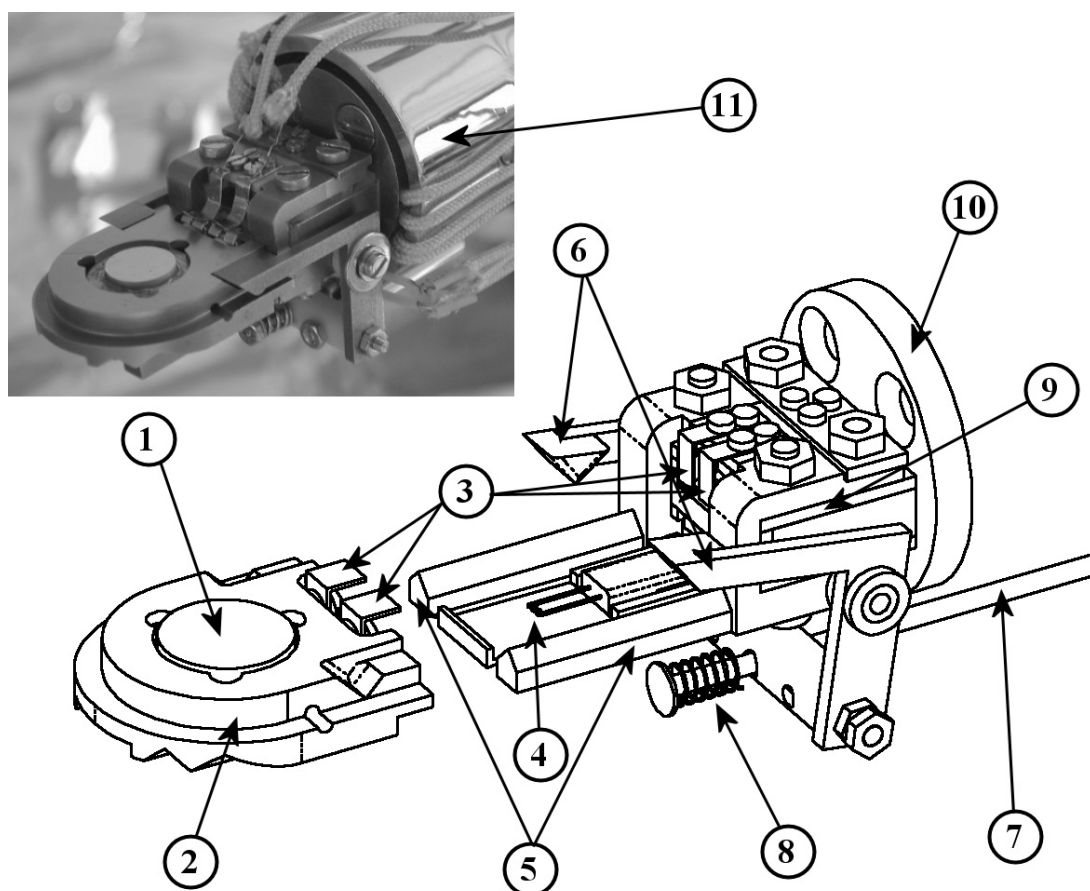


Figure 2.3: The sample holder and the manipulator head: (1) Sample (single crystal), (2) Sample holder, (3) Thermocouple, (4) Filament for e-beam heating, (5) Holding fork, (6) Fixing arms, (7) Translation rod to control the fixing arm position, (8) Return spring, (9) Insulating sapphire plate, (10) Molybdenum support screwed on the flux cryostat cold plate (11).

The sample (1) (see figure 2.3) used is typically a metallic single crystal hat-like shaped, 3 mm high and 7 mm in diameter. It is fixed in the sample holder (2) by a circlip

made out of a tungsten $\varnothing 0.6$ mm wire. A thermocouple type K (Chromel-Alumel) is positioned between the sample bottom and the circlip. Linking of the thermocouple between sample holder and manipulator is obtained through the elastically shaped strips (3). The latter are simply made out of a laminated $\varnothing 1$ mm thermocouple wire.

The sample holder has two pairs of longitudinal grooves under it, the internal one to maintain it on the manipulator, the external one to maintain it in the STM or in the depot. Here the internal grooves fit onto the manipulator fork (5). The sample holder is kept in position with the two arms (6) that can be opened or closed by translation of the rod (7). The return spring (8) applies some stress in order to keep good thermal contact, and prevents any damaging when heating or cooling down by taking over the thermal stress.

Control of the sample temperature is twofold. On the one hand it can be cooled by the manipulator head (10), connected to the cold plate (11) of a flux cryostat [106]. The temperature of the sample goes down to about 100 K when using liquid nitrogen, and down to about 40 K when using liquid helium. On the other hand heating of the sample is performed through the filament (4) located very close to the sample bottom. For low power heating (counter-heating at low temperatures), the filament is heated up by Joule effect and transfers radiational heat to the sample. For larger heating power, the filament is additionally brought to a negative high voltage (700–1000 V) and produces high energy electrons attracted to the nearest zero-potential part, i.e., the sample, to which they deliver their heat converted energy. Temperatures of up to 1400 K can be reached.

The sample holder, the fork and the fixing arms are electrically insulated, allowing for the monitoring of the flowing electron current and thus the heating power. Insulation of the fork (5) is obtained through sapphire plates (9) which are good thermal conductor at low temperature; insulation of the arm (6) is obtained through standard ceramic parts.

All sample-holder metallic and ceramic custom parts were fabricated at the workshop of the Institute of Nanostructure Physics (IPN) of the Swiss Federal Institute of Technology (EPFL). Sapphire parts were procured from the company Kyburz [107].

Sample preparation

The experiments described in the following chapters were performed on various surface orientations of noble-metal single crystals: Ag(100), Au(111), Cu(111) and Cu(100). They were cleaned *in situ* under UHV conditions by sequential cycles of Ar⁺ sputtering at 300 K (typically 20 minutes with a 5 $\mu\text{A}/\text{cm}^2$ ion beam of 900 eV energy and an incident angle of 45°) and subsequent annealing (900 K for Cu and Au, and 700 K for Ag). The pressure while annealing was always below 2×10^{-9} mbar. The procedure resulted in atomically clean and flat surfaces with regions showing terraces of more than 100 nm in width.

The TPA molecules (from the company Fluka, purity >99%) were first outgassed in vacuum for several hours and then evaporated from the OMBE cell at 150°C onto the substrate. This provides a deposition rate of about one monolayer (ML) per minute. For the deposition of metal (Co and Fe) typically a deposition rate of 0.1 ML per minute was used.

Tip preparation

The tips used are made out of a Platinum-Iridium (PtIr) alloy or Tungsten (W) $\varnothing 0.25$ mm wire. PtIr-tips are obtained by manual cutting and are directly usable. W tips are obtained by electrochemical etching but usually oxidize and require *in situ* preparation, like field emission treatment or ion bombardment [60–62]. The tip is magnetically maintained in the STM by its tip holder and can be easily exchanged (see Fig. 2.9).

2.3 The cryostat

The bath cryostat, as designed by the company *Cryovac* [106], is shown schematically in figure 2.4. It consists of a liquid helium tank (2) surrounded by a liquid nitrogen tank (1). The STM is fixed on the cold plate (5). Nitrogen refill is needed every 60 hours (two days and a half) whereas a helium filling lasts for more than three days.

Theoretical considerations

In vacuum, heat can be transmitted by conduction and radiation. The radiative power emitted from a surface is proportional to the material emissivity and to the fourth power of

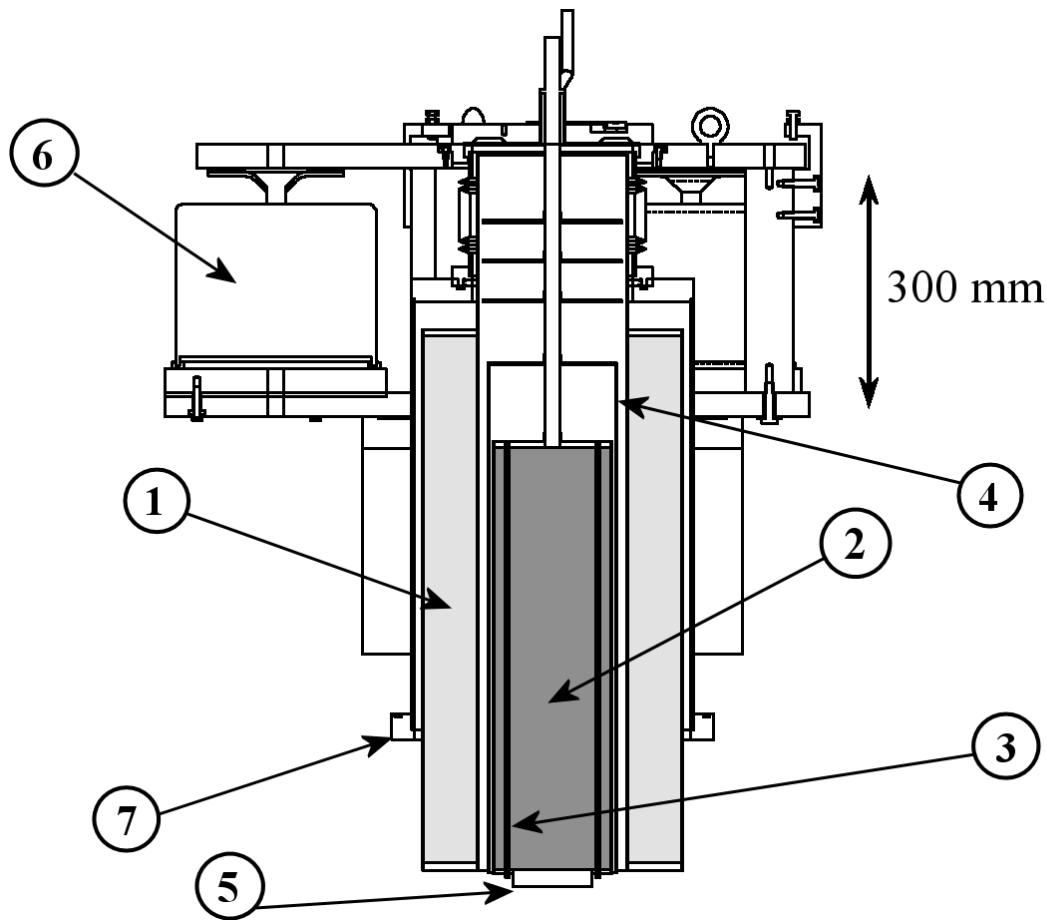


Figure 2.4: Vertical cross section through the bath cryostat: (1) Liquid nitrogen tank (36 L), (2) Liquid helium tank (9.3 L), (3) Feedthrough tube for the wires, (4) Radiation shield, (5) Cold plate, (6) Suspension leg, (7) COF350 flange for fixing on the vacuum chamber.

the temperature: $P_{rad} = \varepsilon A \sigma (T_{ext}^4 - T^4)$, where σ is the Stefan constant, A the radiative area, ε the material emissivity, T_{ext} the surrounding temperature and T the material temperature. For a fixed design (for a given A), it is therefore very efficient to place the low temperature parts in a liquid nitrogen cooled environment, as going from a temperature of 300 K down to 77 K (liquid nitrogen temperature) reduces the radiative power by a factor of $(300/77)^4 \approx 230$. This is the purpose of the liquid nitrogen bath.

The surface of the cryostat is specially treated (polished or gold-plated) to enhance its reflectivity in order to reduce the radiation absorption. The STM is screwed on the cryostat cold plate ((5) Fig. 2.4). Directly around it a radiation shield (see figure 2.5) kept at liquid helium temperature is mounted, surrounded by a second radiation shield in thermal contact with the liquid nitrogen tank. The shields are made out of gold-

plated copper (for a high emissivity and a good thermal conductivity). Each of them consists in a pair of cylinders with a series of apertures used for visualizing (through sapphire windows), transferring the sample and for a direct access to the sample surface for evaporating material on it or irradiating it with light. On each pair one cylinder can rotate around its symmetry axis by means of a ball bearing in order to open or close the different apertures. The rotation is obtained by coupling with a linear feedthrough manipulated from outside of the vacuum chamber. In STM measuring position, the shields are carefully closed in order to reach the lowest temperature, avoid thermal drift and liquid helium loss.

Conductive heat is mainly transmitted through the electrical wires and follows the Fourier law $P_{cond} = \frac{\pi d^2}{4} \lambda \frac{\Delta T}{L}$, where d is the wire diameter, λ the heat conductivity, $\frac{\Delta T}{L}$ the temperature gradient along the wire of length L . To keep it as low as possible, and for a given design (for a given L), the wires are chosen as thin as possible and made out of a poorly conductive material (stainless steel). They are also carefully thermally anchored at various stages to reduce the temperature gradient along them, especially close to the STM (see section 2.4.2). But this anchoring is not sufficient and a non negligible conductive heating power remains. In order to counter it, a copper braid ((21) Fig. 2.8) connects thermally the STM to the cryostat. Without this braid, the lowest temperature reached is not less than about 14 K, whereas 5 K is obtained with it.

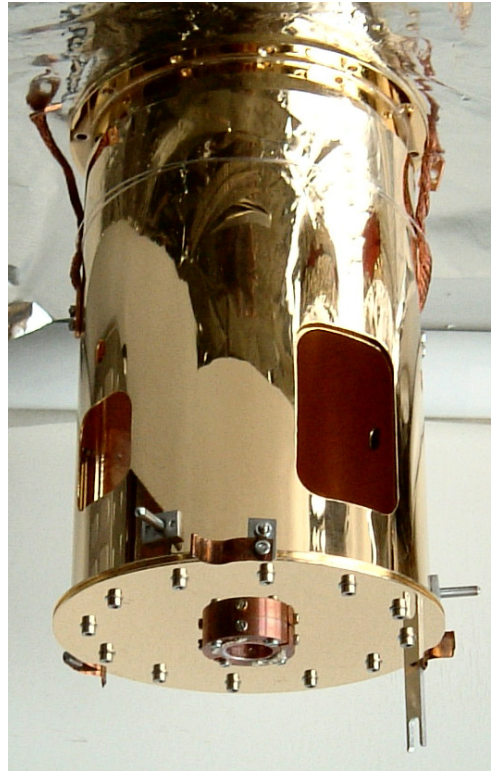


Figure 2.5: Cryostat shield made out of gold-plated copper.

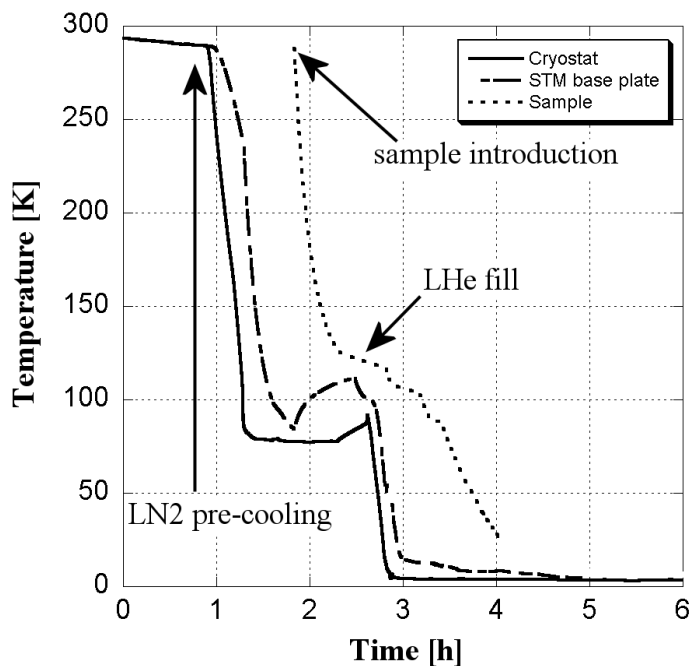


Figure 2.6: Cooling of the STM. At $t=0$ the external tank is filled with liquid nitrogen (LN_2). Then LN_2 is also introduced into the central tank to pre-cool it. When the cryostat has reached 77 K, the sample (at room temperature) is introduced in the STM, whose temperature then slightly increases. Filling of the central tank with liquid helium starts at $t=2:30$. Equilibrium temperature (5.0 K) is reached after about 6 hours. The temperatures indicated by the Si-diodes on the cryostat and on the STM base plate, as well as by the thermocouple on the sample are reported. No data for the sample thermocouple is shown for low temperatures because of its poor reliability.

Temperature measurement

The type K thermocouple installed on the sample holder (Fig. 2.3) can also be used when the sample is positioned in the STM. It gives a good indication when working in variable-temperature mode, but its precision at very low temperature is poor. Therefore a Silicon Diode (model DT-470-12 from the company Lakeshore [108]) is fixed on the STM base plate ((10) Fig. 2.8). This temperature sensor type exhibits its highest sensitivity in the low-temperature range and has a very good reproducibility. A second Si-diode (model DT-470-13) is fixed on the cryostat cold plate. The temperature of the tip cannot be determined directly. Its value is crucial for the thermal broadening of the spectroscopic features. The tip is however believed to be in thermal equilibrium with its environment

because it is entirely surrounded by low-temperature parts and all the cables connected to the scan piezo are properly thermalized (cf. sec. 2.4).

Cooling

The cooling down of the cryostat starts with the filling of the external tank with liquid nitrogen (see figure 2.6). Before introducing liquid helium, the central tank is pre-cooled with liquid nitrogen down to 77 K in order to avoid unnecessary use of liquid helium. The equilibrium temperature is reached after a few hours. The Si-diode on the STM plate indicates 5.0 K. The right positioning of the closed cryostat radiation shields is crucial for the final temperature as well as for the liquid helium consumption. Any other temperature between 5 K and 400 K can be reached by counter-heating with a Zener diode (variable-temperature mode).

2.4 The STM

The design of the STM is based on the Besocke beetle type (figure 2.7) [109, 110]. This design was adopted because of its relative simplicity and reliability, its compact size and its mechanical stiffness, and because its symmetry makes it less susceptible to thermal drift. The thermal dilatation of the scan piezo is indeed first-order compensated by the external piezos. The difference with a standard Besocke type is that here the approach ramp is located around the scan piezo and maintained by its own weight on the top of the external piezos [90]. The sample is mounted in between the external piezos, what provides good thermal contact between the sample and the STM base plate, an easier access for transferring the sample, and more flexibility in the design of the sample holder.

All STM custom parts were fabricated at the workshop of the Institute of Nanostructure Physics (IPN) of the Swiss Federal Institute of Technology (EPFL). For the assembly UHV-welding and gluing with UHV-compatible epoxy (Epo-tek H77 and H27D [111]) are used.

2.4.1 Description

The STM is described in figure 2.8. It comprises a central piezo scantube (9) controlling the tip position in x , y , and z directions, and three external piezo tubes (8) symmet-

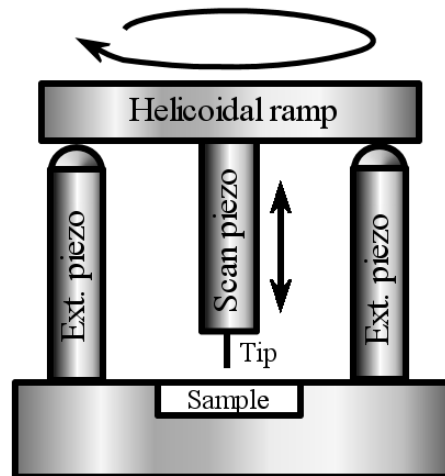


Figure 2.7: Schematics of the modified beetle-type STM design employed for the present setup. Three symmetrically positioned external piezotubes are used for the coarse approach. By periodic tangential slip-stick motion the ramp is rotated and the helicoidal shape generates vertical motion.

rically disposed around it for the coarse approach of the tip to the tunneling position. The piezotubes are made out of material EBL#2 from the company Staveley [112]. The external piezos are terminated by sapphire half spheres (6) that come in contact with a molybdenum ramp (5). The ramp is divided on its lower side in three helicoidal sectors. By periodic tangential slip-stick motion of the external piezos the ramp is rotated and the helicoidal shape generates vertical motion. As the scan piezo is glued to the ramp, the tip is macroscopically approached or retracted. For a maximum rotation of 120° the z translation amounts 0.5 mm.

The sample holder is positioned on a fork-shaped drawer (14). It is pressed against the base plate by the return springs (15). The electrical potential of the sample is thus that of the base plate.

The whole STM is suspended from the top plate (1) (which is screwed to the cryostat cold plate) by three Inconel springs (2) [113]. In its measuring position the STM hangs freely. It behaves therefore as an harmonic oscillator with an eigenfrequency of about 2 Hz. These low frequency oscillations are damped by an eddy current system consisting of four CoSm magnets (17) surrounded by copper flaps (18).

A bayonet tool mounted on a rotary-linear feedthrough and manipulated from outside

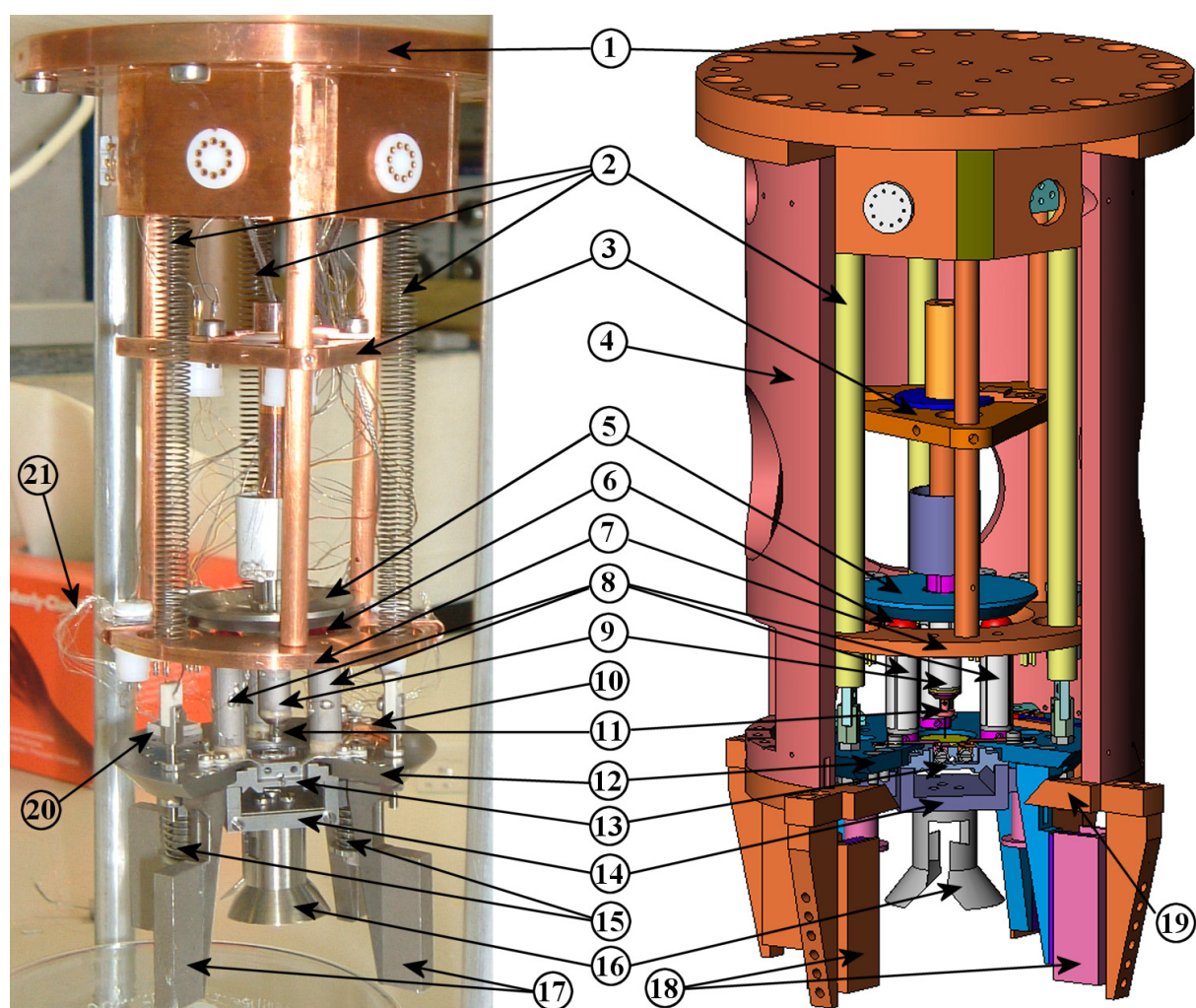


Figure 2.8: View of the STM: photograph (left) and CAD model (right). Total height 180 mm. (1) Top plate (screwed on the cryostat cold plate), (2) Hanging springs, (3) Connector stage #2, (4) Copper support cylinder (front part transparent in CAD drawing, removed for taking the photograph), (5) Molybdenum ramp, (6) Sapphire half-spheres, (7) Copper ring - connector stage #1, (8) External piezos (coarse approach), (9) Central piezo (scan piezo), (10) Si-diode temperature sensor, (11) Tip holder, (12) Base plate, (13) Sample holder, (14) Drawer, (15) Return springs, (16) Bayonet counter-part, (17) CoSm magnets, (18) Copper eddy-current flaps, (19) Conical shape for establishing of thermal contact with the base plate (12), (20) Sapphire squares, (21) Braid for thermalization of the base plate (12).

of the vacuum chamber can be inserted in the counter-piece (16) in order to pull down the STM. During this procedure the Mo-ramp (5) first sits on the copper ring (7), then the base plate (12) comes in contact with the copper part (19). This position is ideal for cooling down the STM, as the conical shape provides a non-negligible contact area and a compressive stress can be applied. Furthermore the conical shape is self-centering, which is important in particular to reposition the Mo-ramp, as it can swing macroscopically in x and y directions. A further pull-down of the bayonet tool will compress the return springs (15) (which are much stiffer than the springs (2)) and release the drawer (14) so that the sample holder can be transferred to or out of the STM.

The STM is incorporated in a copper cylinder (4) providing some holes for direct access from the outside. The purpose of this part is to maintain the eddy current flaps (18), and to establish good thermal and mechanical contact with the base plate (12) via the conical shape (19) when it is in the cooling or transferring position.

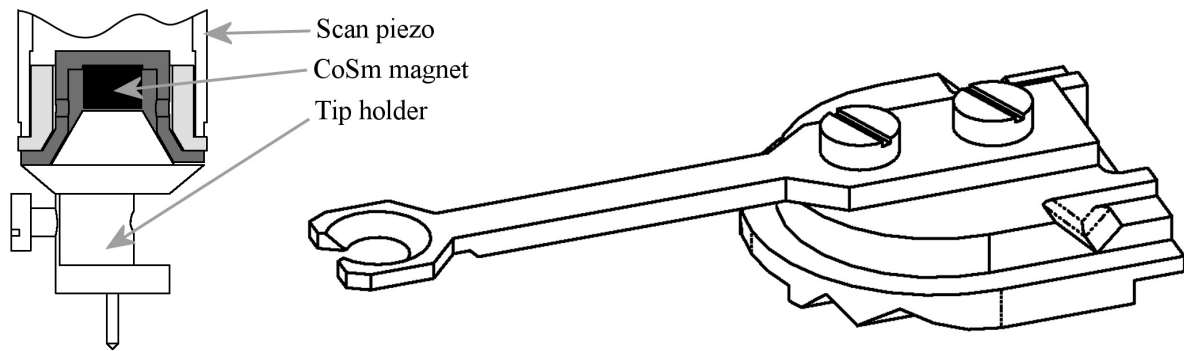


Figure 2.9: (left) Anchoring of the STM tip holder inside the scan piezo (cross section). On the right the specially designed tip exchange tool.

A Silicon diode (10) for measuring the temperature is screwed on the base plate. For a better thermalization when the STM is in measuring position two braids (21) made out of about 2×20 thin ($\varnothing 0.05$ mm) silver-coated copper wires are connecting the base plate to the copper ring (7). They are squeezed between two sapphire squares (20) to ensure electrical insulation as well as a good thermal conduction. A Zener diode type BZY93C75 (not visible, located in the back side) is screwed on the base plate. When desired, a current flowing through it produces the necessary heating power to reach any temperature in the range 5-400 K (variable-temperature mode). A significant heating

power is obtained with a relatively low current because of the high threshold potential of the diode (75 V).

The tip holder (11) made out of steel is maintained in position inside the central piezo by a CoSm magnet. Tips can therefore be exchanged or treated *in situ*. For this purpose a specially designed tip exchange tool is used (see figure 2.9).

2.4.2 Wiring

The requirements needed for a proper wiring of the STM head are listed below.

Around the STM: The main requirement for the wires connected directly to the STM is a high flexibility for avoiding the transmission of vibrations. Kapton coated $\varnothing 50 \mu\text{m}$ copper wires are used. 23 cables are connected to connector stage #1, 9 to connector stage #2 (figure 2.8). This second stage delivers all the signals for the central piezo. Special connectors made with sapphires plates are used here to ensure proper thermalization of the cables and therefore of the entire piezo (especially the tip). The connectors are positioned for an easy mounting/dismounting of the base plate and the central piezo. A last set of connectors on the top plate ((1) Fig. 2.8) allows for dismounting of the whole STM out of the cryostat.

Inside the cryostat: Here the thermal properties are decisive. The heat conducted from the room temperature parts to the liquid helium temperature core must be minimized. A poor conductive material is used (stainless steel, teflon coated [114]) in combination with a rather small diameter (0.1 mm). To avoid electromagnetic noise coaxial cables are necessary for the tunneling current, the sample bias, and the z -electrode signals. The capacitance of the coaxial cables is of great importance as it will set the upper limit for the frequency response of the feedback loop. Coaxial cables type SS from the company Lakeshore [108] are used ($\varnothing 1 \text{ mm}$, capacitance 0.17 nF/m). Phosphor-bronze twisted wire pairs are used to minimize the pickup noise for the four-points temperature measurement of the Si-diodes.

Thermal anchoring consisting in winding around heat sinks is implemented for all the cables at the bottom of the liquid helium tank (at 4.2 K) as well as above it at $\sim 20 \text{ K}$. In between, the cables are passing in the feedthrough tubes (3) of Fig. 2.4

through the liquid helium tank.

Outside of the vacuum chamber: Here standard cables are used. Coaxial BNC cables are connecting all the scan piezo electrodes, as well as the sample bias. The tunneling current preamplifier is connected directly at the exit of the vacuum chamber.

2.4.3 Mechanical stability

STM measurements require a great stability (the resolution in z must be $<0.01 \text{ \AA}$). It is therefore crucial to know the mechanical characteristics of the STM head and its frequency dependent behavior, and to get rid of external vibrations by use of appropriate damping. The external noise sources are principally the building oscillations and the acoustic waves. Building oscillations are typically in the range 1 to 30 Hz and are partially damped (figure 2.10) by the pneumatic legs holding the whole apparatus (see Fig. 2.1). The second pneumatic isolator stage ((6) Fig. 2.4) decouples further the He-bath cryostat and limits transmission of eigenfrequencies from the rest of the vacuum chamber, as well as the vibrations coming from the bubbling of liquid nitrogen. The STM itself is then held on three springs that act as a low-pass filter with an eigenfrequency of about 2 Hz. To prevent long time oscillations at this frequency, eddy current damping is installed (figure 2.8).

Calculation of eigenfrequencies

The beetle-type STM can be modeled as a disk of mass M sitting on three massless piezo tubes (see Fig. 2.7) with spring constants K_{\perp} and K_{\parallel} for bending and stretching motions, respectively. For a tube with length l , inner diameter d , outer diameter D , and Young modulus E , the spring constants are [115]:

$$K_{\perp} = \frac{3\pi}{64} E \frac{D^4 - d^4}{l^3} \quad \text{and} \quad K_{\parallel} = \frac{\pi}{4} E \frac{D^2 - d^2}{l}$$

If we assume that the legs are fixed to the ramp we can calculate the resonance frequency for the three different modes horizontal translation (H), vertical translation (V)

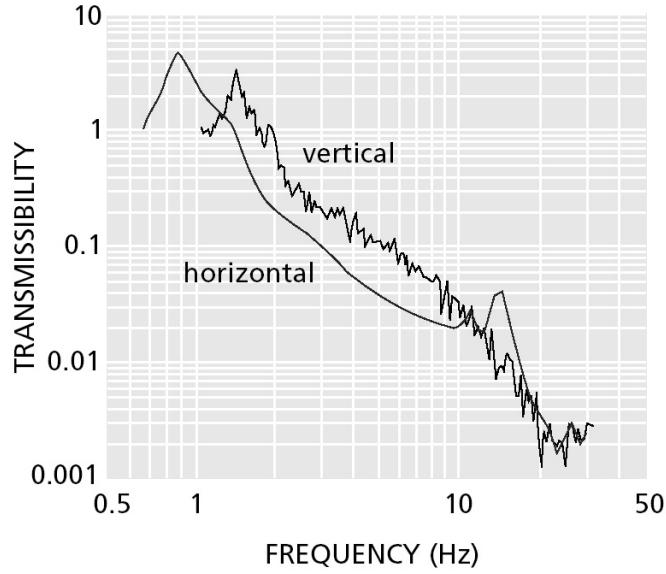


Figure 2.10: Typical frequency response of a pneumatic vibration isolator (from [97]).

and rotation (R) around the symmetry axis:

$$f_H = \frac{1}{2\pi} \sqrt{\frac{3K_{\perp}}{M}}$$

$$f_R = \frac{1}{2\pi} \sqrt{\frac{6K_{\perp}}{M}} = \sqrt{2} f_H$$

$$f_V = \frac{1}{2\pi} \sqrt{\frac{3K_{\parallel}}{M}}$$

When replacing with the actual values $l=18$ mm, $D=6.3$ mm, $d=5.7$ mm, $E=6.3 \times 10^{10}$ N/m² [112] and $M=30$ g one obtains $f_H = 1.5$ kHz, $f_R = 2.1$ kHz and $f_V = 7.1$ kHz.

The measured frequency response of the STM is shown in figure 2.11. The different modes are not easily distinguishable and the proposed model seems to be too simplistic for describing the real system. Furthermore, resonances corresponding to the so-called rattling motion are measured. These are related to the microscopic contact between the ramp and the sapphire balls and depend on the local friction and adhesion properties. The lowest substantial resonance frequency is ~ 1.1 kHz. The periodic motion of the scan-piezo must be therefore performed at a frequency much lower than this value.

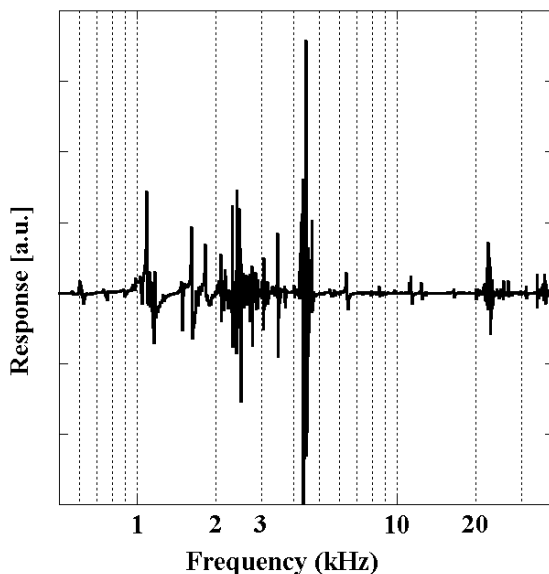


Figure 2.11: Resonance spectrum of the STM (semi-log representation). An external force is simulated by applying a sinusoidal voltage ($1 V_{rms}$) to an electrode of one of the coarse-approach piezos, the mechanical frequency dependent response of the system is obtained by monitoring the harmonic signal picked up on the $+x$ electrode of the scan-piezo.

2.4.4 The STM-control electronics - recording modes

The scan head is controlled by the commercial unit SPM100 developed by RHK [116]. The high voltage delivered is ± 130 V. The maximal scan range achieved is about $5 \mu\text{m}$ when operating at room temperature and $1 \mu\text{m}$ when operating at 5 K (due to the temperature dependence of the piezoelectric coefficients). The xy -scan signal is digitally generated. Data is transferred to a PC through a 150 kHz I/O board and a 12 bit A/D converter. The preamplifier used (RHK-IVP 200) has an amplification factor of 10^8 A/V. A multigain post-preamplifier allows for further amplification ($\times 1$, $\times 10$ or $\times 100$) and low pass filtering of the signal (usually with a cutting frequency of 1 kHz). Image processing was performed with the user-friendly public domain software *WSxM* [117].

The images acquired in constant current mode are obtained by recording the z signal while scanning over the surface. The feedback loop acts on the z voltage to maintain the tunneling current equal to the set value. By fast recording several frames on the same location at a given periodicity (movie mode) it is possible to follow the kinetics of surface physical or chemical processes (diffusion, reaction, etc...).

For spectroscopy measurements the tip is moved to the desired location and the feedback loop is opened, so that the tip position is kept constant. The bias voltage is then ramped. The tunneling current is recorded and its numerical derivative with respect to the bias voltage delivers the requested dI/dV spectrum. Another possibility is to add a small ac modulation in the bias voltage at a given frequency. By means of a lock-in amplifier the related harmonics in the tunneling current are extracted. The first harmonic is proportional to dI/dV , and the second to d^2I/dV^2 .

2.5 STM test measurements

The first measurements performed with the new experimental setup described in this chapter demonstrate its ability to investigate surfaces with high resolution. In particular, the observation of the very low corrugated standing waves on Au(111) is a confirmation of the overall excellent stability of the STM down to a temperature of 5 K.

Atomic resolution on Ag(100)

Figure 2.12 is a STM image of a Ag(100) surface revealing atomic resolution and the corresponding square crystallographic structure. The atomic corrugation is about $\approx 0.1 \text{ \AA}$, the noise amplitude is close to 0.03 \AA .

Surface states on Au(111)

Densely packed $fcc(111)$ noble metal surfaces exhibit Shockley-type surface states. These electronic states are located energetically in the partial gap of the bulk states. Their wave functions peak near the surface and decay exponentially both into the vacuum and into the bulk of the solid. Parallel to the surface they behave as a two-dimensional (2D) free electron gas characterized by \vec{k}_{\parallel} , the wave vector parallel to the surface. The surface-state dispersion is thus expected to be parabolic and isotropic in the center of the surface Brillouin zone $\bar{\Gamma}$:

$$E = E_{\bar{\Gamma}} + \frac{\hbar^2}{2m^*} k_{\parallel}^2. \quad (2.1)$$

Here $E_{\bar{\Gamma}}$ is the surface-state band edge energy and m^* the effective mass. The density of states of a free 2D electron gas is a constant above the onset at $E_{\bar{\Gamma}}$.

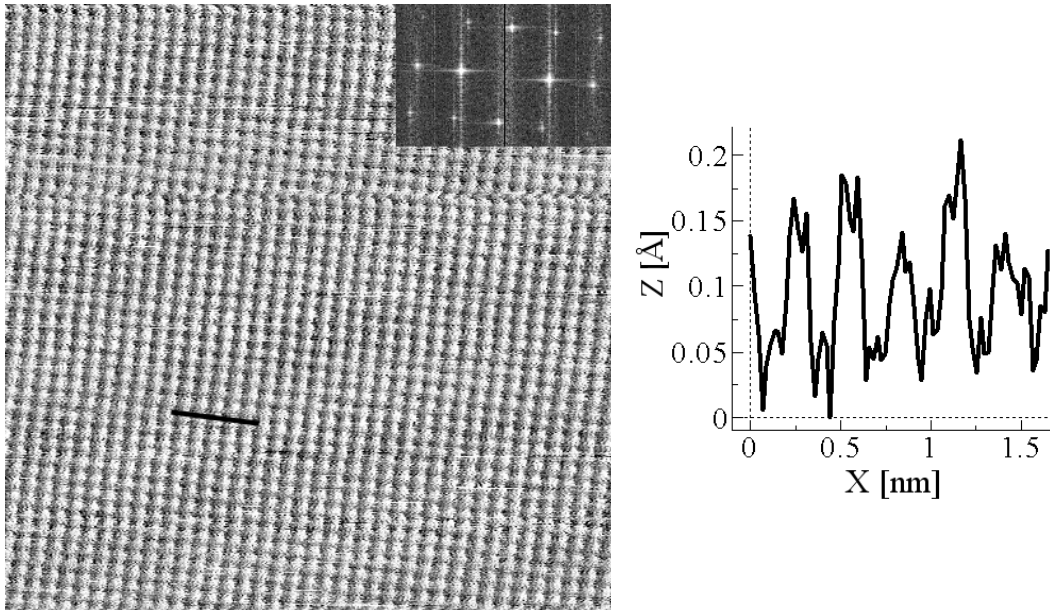


Figure 2.12: Raw data demonstrating atomic resolution of the Ag(100) surface at room temperature (STM in constant current mode, image size $11 \times 11 \text{ nm}^2$, $I=0.8 \text{ nA}$, $V=-1.5 \text{ mV}$). Inset: The Fourier transform reveals the square structure. Right: contour line along the black bar. The atomic corrugation amounts $\approx 0.1 \text{ \AA}$, the noise level is about 0.03 \AA .

The current understanding of the surface states is mostly due to photoemission studies which have been the standard technique of their investigation for over twenty years [118]. Nevertheless they have been also observed by STM on Au(111) and other noble metal and transition metal surfaces [72, 119–122].

Figure 2.13 (a) shows a Scanning Tunneling Spectrum (STS) acquired on the bare Au(111) surface at 5 K. The surface state signature is the strong increase of the tunneling conductance at the energy of its band edge. The measured onset energy for the surface state peak is -510 meV . The density of states differs from an ideal step function expected for the LDOS of a two-dimensional electron gas. This is due to the facts that the states of larger k_{\parallel} provide smaller contribution to the spectrum [71], and that the surface state is slightly delocalized into the bulk for higher energies [123].

The scattering of the 2D electron gas at step edges and impurities produces interferences between incoming and reflected electronic states. These interferences lead to modulations in the LDOS at the Fermi level close to the defects and formation of a standing wave pattern. At low sample bias the latter is directly visible in the STM image

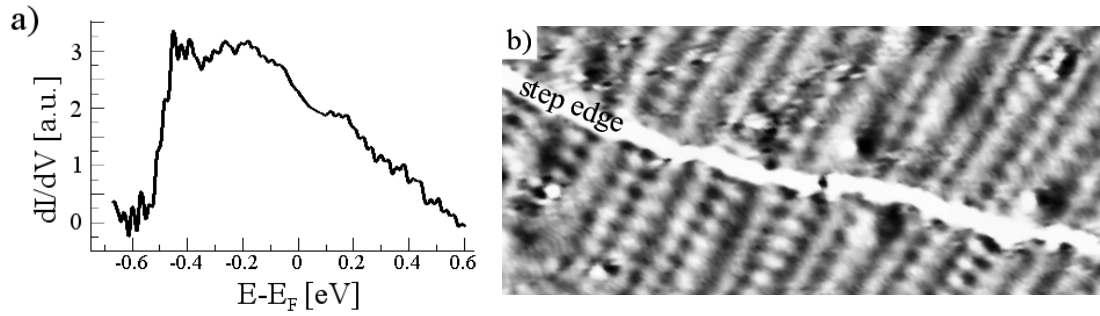


Figure 2.13: Surface states on Au(111). a) STS spectrum (numerical derivative of $I(V)$). b) Standing wave pattern caused by scattering of the surface state electrons at a step edge and at impurities. The surface reconstruction lines are also visible perpendicular to the step edge. The derivative of the topographic data is shown for better contrast (STM image size $55 \times 25 \text{ nm}^2$, $I=0.4 \text{ nA}$, $V=-10 \text{ mV}$, $T=5 \text{ K}$).

topography (see chapter 1). Figure 2.13 (b) reports such a standing wave pattern in the vicinity of a step edge. The corrugation of the waves amounts about 0.05 \AA . The wave length measured is $18.3 \pm 0.5 \text{ \AA}$ and corresponds to half of the wave length¹ of the surface state at the Fermi energy [72].

¹The factor two comes from the fact that electron densities are measured and not directly their wave function.

Chapter 3

Self-Assembly of Terephthalic Acid with Epitaxial Stress: Response of the Hydrogen Bond

In this chapter we report STM investigations addressing the bonding and supramolecular self-assembly of the molecule 1,4-benzenedicarboxylic acid (terephthalic acid - TPA) on the reconstructed Au(111) and on the Cu(111) surfaces at ambient temperature under ultra-high-vacuum (UHV) conditions. TPA belongs to the family of aromatic molecules with exodentate carboxyl functionalities, which are frequently employed in three-dimensional (3D) crystal engineering [27,124] and have proven to be appropriate for supramolecular architecture at surfaces [125–130]. In the TPA bulk structure the H-bonded chains typical for linear dicarboxylic acids are found, resulting from a dimerization of the self-complementary carboxyl groups (figure 3.1) [131,132]. It is of interest to find out whether this coupling scheme can be maintained in surface-supported arrangements.

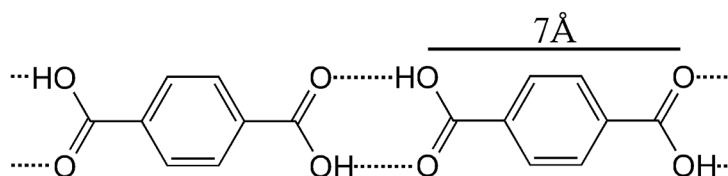


Figure 3.1: Typical linear motif resulting from the dimerization of the carboxyl groups of TPA molecules and formation of twofold hydrogen bonds.

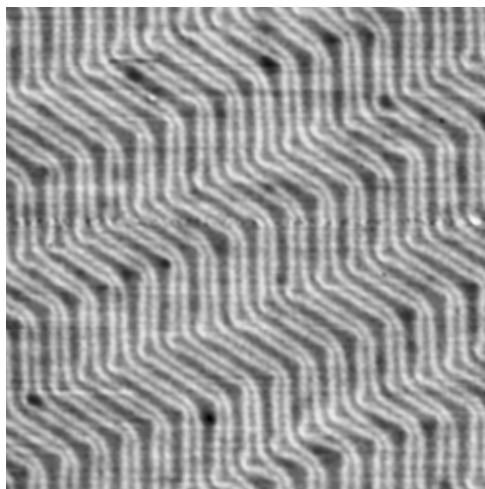


Figure 3.2: The chevron structure of the reconstructed ($22 \times \sqrt{3}$) Au(111) surface (STM image size $70 \times 70 \text{ nm}^2$, $I=1.0 \text{ nA}$, $V=-800 \text{ mV}$).

As a substrate we have chosen first the close-packed Au(111) surface, which provides small atomic corrugation and low chemical reactivity. Thus the carboxylic acid groups are expected to be preserved at ambient temperature [133]. Moreover, the Au(111) chevron reconstruction [134] accounts for a substrate with natural dislocation pattern (Fig. 3.2) and varying interatomic spacing, which allows for an investigation of the response of hydrogen-bonded systems to such features [5, 37]. The second substrate chosen, Cu(111), extends this investigation to a substrate with homogeneous but comparatively reduced interatomic distances. With this system no regular packing is encountered and dislocations in the molecular layer occur. In contrast to carboxylate formation encountered on the more reactive Cu(110) and Cu(100) surfaces [126, 127, 135, 136], the carboxylic acid group is also expected to be mostly preserved on Cu(111).

The STM data presented in this chapter was measured at room temperature.

3.1 TPA on Au(111)

In this section the adsorption and supramolecular ordering of TPA on the reconstructed Au(111) surface is discussed. Two-dimensional (2D) self-assembled domains evolve, wherein the well-known one-dimensional (1D) carboxyl H-bond pairing scheme is identified. Since the individual molecules occupy a distinct adsorption site and the supramolecular

ordering usually extends over several substrate reconstruction domains, the inhomogeneous distortions of the latter induce significant variations in hydrogen bond lengths, which illustrates the versatility of hydrogen bridges in molecular engineering at surfaces. *Ab initio* calculations for a 1D H-bonded molecular chain provide insight into the limited geometric response of the molecules in different local environments. At small concentrations adsorbed TPA is highly mobile and induces an increased mobility of substrate atomic steps.

3.1.1 Description of the self-assembly

Samples with a coverage of one monolayer or less were prepared. One monolayer (ML) refers to a complete layer of the dense hydrogen-bonded phase described below. At small concentrations it is difficult to determine the exact coverage by STM at room temperature because the molecules are very mobile on the gold surface and form a two-dimensional molecular gas phase where the molecules cannot be imaged individually. Upon increasing the density beyond about 0.5 ML the molecules condense into large compact well ordered domains. However, these domains can be easily perturbed by lowering the tunnel resistance (approximately under 10 M Ω).

The adsorption of aromatic molecules on transition and noble metal surfaces is mainly directed by the interaction of the π -orbitals of the aromatic ring with the d -orbitals of the substrate (see, e.g., Ref. [137]). On Au(111), the physisorption of TPA is strong enough to keep the molecules on the surface up to about 430 K, the temperature at which they start to desorb. This temperature corresponds to an activation energy for desorption of roughly 1 eV [138]. For comparison, the adsorption energy of benzene on Au(111) amounts 0.6 eV (60 kJ/mol) [139]. However, the surface diffusion barrier of TPA is low and therefore the molecular diffusivity is high at room temperature. It should be pointed out that, although the substrate appears thus rather flat with regard to the 2D diffusion, the modulations in the surface potential due to the atomic periodicity are sufficiently strong to determine the commensurability of the adsorbed supramolecular sheet, as we will show below.

Figure 3.3 shows the typical organization of a TPA layer. The chevron reconstruction of the Au(111) surface [134] is clearly visible in the upper part, where very mobile molecules are present, as well as in the lower part underneath the TPA layer. The layer imaging height is 0.8 ± 0.1 Å above the surface covered by the 2D gas phase, the intralayer

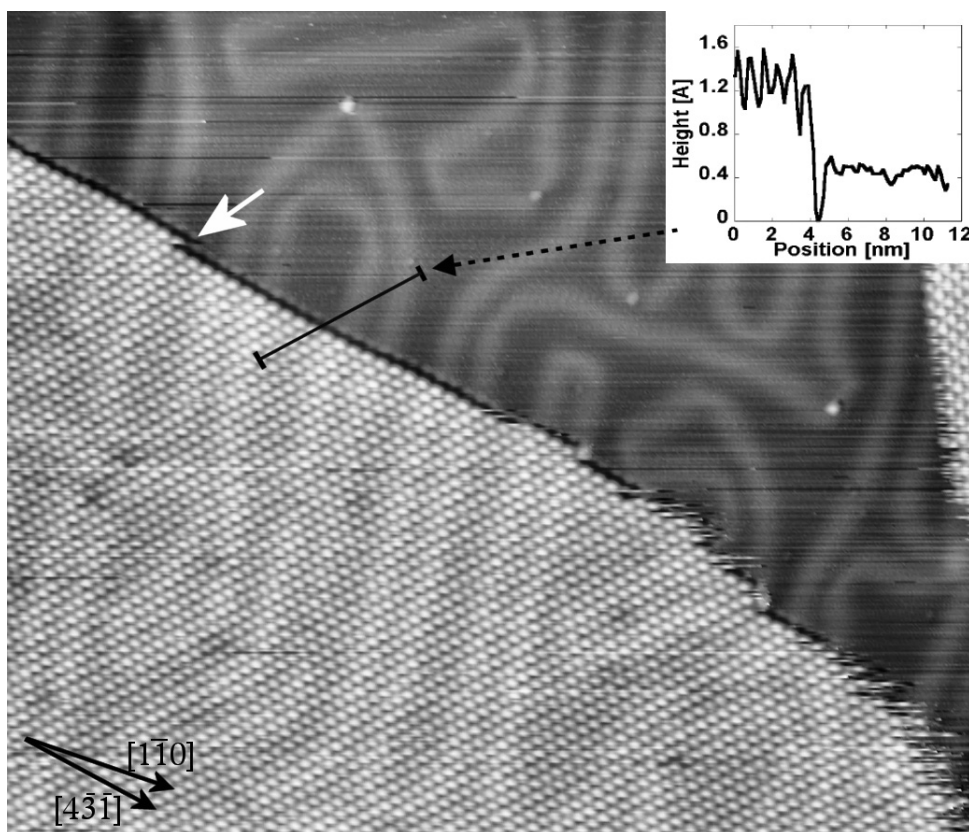


Figure 3.3: Typical organization of a hydrogen-bonded TPA layer on Au(111). The surface reconstruction is clearly visible in the entire imaged area. The inset shows a contour line along the indicated bar. The white arrow points to a site appearing as a kink (see discussion in text). (STM image size $58 \times 50 \text{ nm}^2$, $I=0.4 \text{ nA}$, $V=-470 \text{ mV}$, TPA coverage 0.8 ML)

molecular corrugation is $0.4 \pm 0.1 \text{ \AA}$. At the domain edge typically a gap of $0.2 \pm 0.1 \text{ \AA}$ in depth occurs. The domain looks blurred on some parts of its border due to molecules that moved during the scan. We cannot discern whether this motion is diffusion along the boundary or an exchange with the 2D gas phase by evaporation and recondensation. Kinks such as the one indicated by the white arrow in figure 3.3 are rare, domains are usually terminated by a complete row of molecules. We believe that this feature is not a real kink, rather presumably a complete row having evaporated into the 2D gas phase when tip was at this position. The domain edge here, along the $[4\bar{3}\bar{1}]$ direction, is much better defined than that in the lower right hand part of the island, where the border appears frizzled. The higher stability of the $[4\bar{3}\bar{1}]$ edge direction reflects the anisotropic longitudinal/lateral intermolecular interactions. The individual TPA are imaged as flat

rod-like protrusions (about $7 \text{ \AA} \times 5 \text{ \AA}$) aligned with the $[\overline{43}1]$ direction. Their dimension is fitting well with the size of a flat lying molecule. The observation of a preferred direction both on an individual molecular basis and arising from the domain stability determines the orientation of the molecules relative to each other, which is governed by the carboxylic acid dimerization via hydrogen bonding, as expected from the shape and functionality of the molecule (figure 3.1). The formation of 2D molecular sheets furthermore suggests a lateral coupling between the 1D TPA chains, which is presumably mediated by weak hydrogen bonds or electrostatic interactions. The observed structure is similar to the one of TPA bulk and in agreement with investigations of related systems [11, 125, 127, 128]. Apart from the reconstruction pattern of the underlying gold substrate no long range corrugation (indicative of a Moiré or a dislocation pattern) of the TPA sheets could be seen. Therefore we deduce that the molecular layer is commensurate with the substrate and that the individual TPA reside at a distinct adsorption site. The actual adsorption site could not be identified on the basis of the present experiments.

The TPA molecules arrange in a quasi-hexagonal lattice with different orientations relative to the substrate. Figure 3.4 shows four coexisting rotational domains. The rectangular shape delimiting a region covered by the 2D gas phase is at first glance unexpected on a surface with hexagonal symmetry but can be easily explained by the molecular superstructure. We observed in total six equivalent orientational domains. The unit cell parameters measured are $8.3 \pm 0.3 \text{ \AA}$ (along $[0\overline{1}1]$) and $10.0 \pm 0.3 \text{ \AA}$ with an angle of $45^\circ \pm 3^\circ$. The quasi right angle between the domains thus results from two adjacent mirror domains leading to an overall rotation of the molecular chains by $2 \times 45^\circ$.

We propose the following matrices to describe the commensurate superstructure: $\begin{pmatrix} 3 & 0 \\ 1 & 3 \end{pmatrix}$ and its mirror symmetry $\begin{pmatrix} 3 & -3 \\ -2 & -1 \end{pmatrix}$. Note that this superstructure is referred to an ideal (111) plane; the exact superstructure matrix should also include the $(22 \times \sqrt{3})$ gold reconstruction. Figure 3.5 shows the proposed model for the unit cell. For simplicity we first consider the Au(111) surface plane as perfectly hexagonal (as the surface is reconstructed this is not exactly true; this point will be discussed below). Three rotational domains exist reflecting the substrate symmetry. In addition, since the molecular lattice is not exactly hexagonal, within each rotational domain two chiral arrangements related by a mirror symmetry exist. The molecule itself is not chiral, neither in the gas

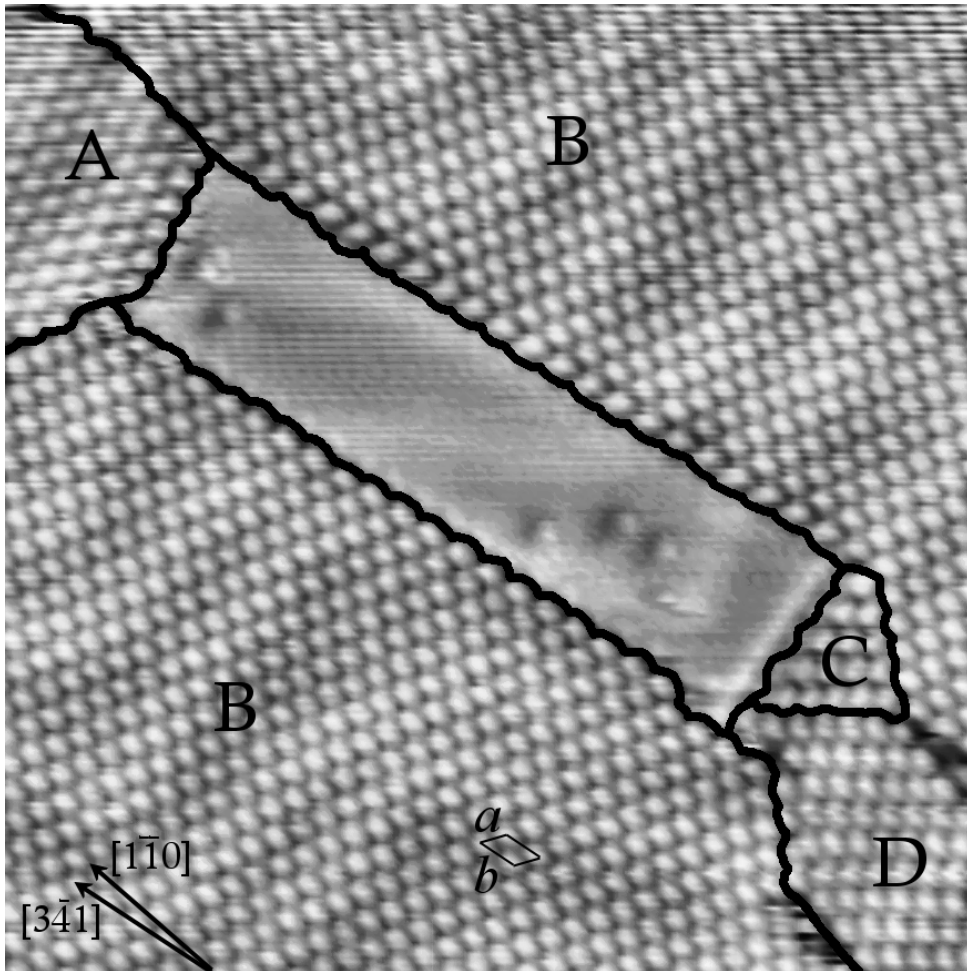


Figure 3.4: Coexistence of different TPA rotational domains on Au(111). Four orientations are present in this image: A, C and D are rotated by 120° relative to each other; B represents the mirror symmetric arrangement of D with respect to $[1\bar{1}0]$. B is similarly the chiral counterpart to the domain in figure 3.3 (STM image size $28 \times 28 \text{ nm}^2$, $I=0.5 \text{ nA}$, $V=-20 \text{ mV}$).

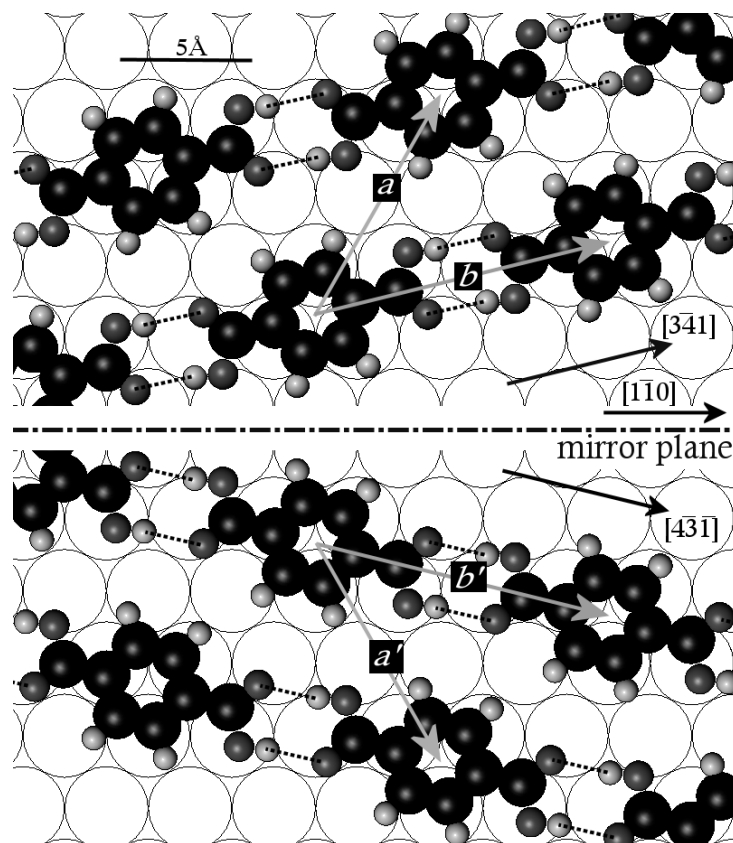


Figure 3.5: Model for the molecular superstructure; \mathbf{a} (along the $[0\bar{1}1]$ direction) and \mathbf{b} (along the $[3\bar{4}1]$ direction) are the lattice vectors. The oblique shape of the unit cell induces a chiral symmetry break: the mirror symmetric is an equivalent but not superimposable superstructure (lattice vectors \mathbf{a}' and \mathbf{b}'). The hydrogen bonds are indicated by dashed lines. For simplicity the Au(111) substrate is modeled here as perfectly hexagonal. The molecule adsorption site is arbitrary.

phase nor in the adsorbed geometry. The specific adsorption site within the molecular lattice is neither chiral. The chiral symmetry break is induced exclusively from the oblique shape of the unit cell of the supramolecular 2D assembly representing an enantiomorphous entity.

3.1.2 The Au(111) surface reconstruction

The actually reconstructed Au(111) surface as shown in Fig. 3.2 is not perfectly hexagonal, rather it is locally contracted in a $\langle 1\bar{1}0 \rangle$ direction [134]. The contraction direction does not extend over long distances, and a mesoscopic chevron arrangement with an alter-

nating sequence of two rotational domains occurs at large terraces [134, 140, 141]. As the intermolecular distance is much smaller than the extension of these domains the molecular superstructure should be influenced by the distorted surface (analogous to simple superlattices on reconstructed Au(111), see [142]).

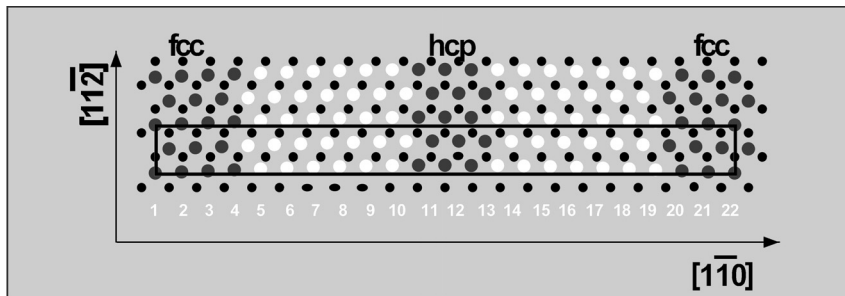


Figure 3.6: Model showing the atomic positions of the surface layer on Au(111) and the $(22 \times \sqrt{3})$ unit cell; small circles: atoms of the second layer; large circles: atoms of the top layer; white: transition region (corrugation lines).

Description

The uniaxial contraction results in a $(22 \times \sqrt{3})$ unit cell where surface Au atoms reside on *fcc*, *hcp* and bridge-type stacking positions on the second layer. The corrugation lines separate the *fcc* from the *hcp* regions (figure 3.6). The distance between two adjacent lines is 44 Å, the neighbored line pairs are 63 Å apart. The reconstruction corrugation typically amounts up to 0.2 Å over a distance of $\frac{44}{2}$ Å, which gives an out-of-plane correction of about 0.5° . The *fcc* to *hcp* site modulation produces a curvature in the lateral atomic alignment of the order of 0.8 Å over a distance of $\frac{63}{2}$ Å, which gives an in-plane correction of about 1.5° . These two effects give a correction for the intermolecular distances in the adsorbed layer of the order of $a(1 - \cos \alpha) \approx 0.5$ pm and are neglected.

Therefore we model the reconstructed surface as a uniaxially and homogeneously contracted hexagonal plane. In the contraction direction we take a constant interatomic distance of 2.75 Å (the bulk interatomic distance is 2.88 Å). Note that in reality this distance oscillates around this value with an amplitude of ± 0.1 Å over the period of the reconstruction (23 surface atomic spacings). In the two other close-packed directions the interatomic distance is assumed to be 2.85 Å.

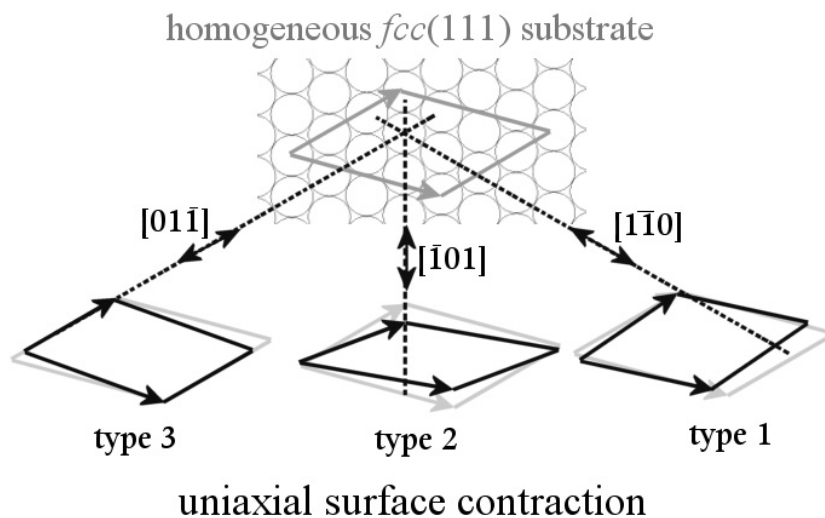


Figure 3.7: The effect of the Au(111) substrate reconstruction on the molecular lattice, and the dependence on the contraction direction. In grey is shown the molecular cell corresponding to a perfectly hexagonal substrate, in black the molecular cell uniaxially contracted along the direction indicated by the double arrow. The type numbers refer to table 3.1.

Influence on the molecular layer

The distortion of the reconstructed surface is transmitted into the molecular lattice, as shown schematically in figure 3.7. Depending on its orientation relative to the surface contraction direction, we find three different unit cells, labeled type 1, 2 and 3, whose parameters are indicated in table 3.1. Although these differences are close to the experimental error we could find direct evidence. Figure 3.8 shows a single molecular domain extending over two gold reconstruction domains. The upper region of the domain is of type 1 while the lower region is of type 2. As shown in the Fourier transform of the two regions, the respective lattice parameters have distinct differences. To explain these differences in more details, the molecular domains are modeled in figure 3.9. The contraction direction, varying from $[1\bar{1}0]$ to $[\bar{1}01]$ influences directly the intermolecular distances (and the hydrogen bond lengths), and induces also small differences in the lattice orientation.

We never obtained sufficiently high resolution in the STM images to resolve the individual functional groups of the molecule. This is generally the case in UHV studies, in agreement with the current theoretical understanding in STM imaging of organic

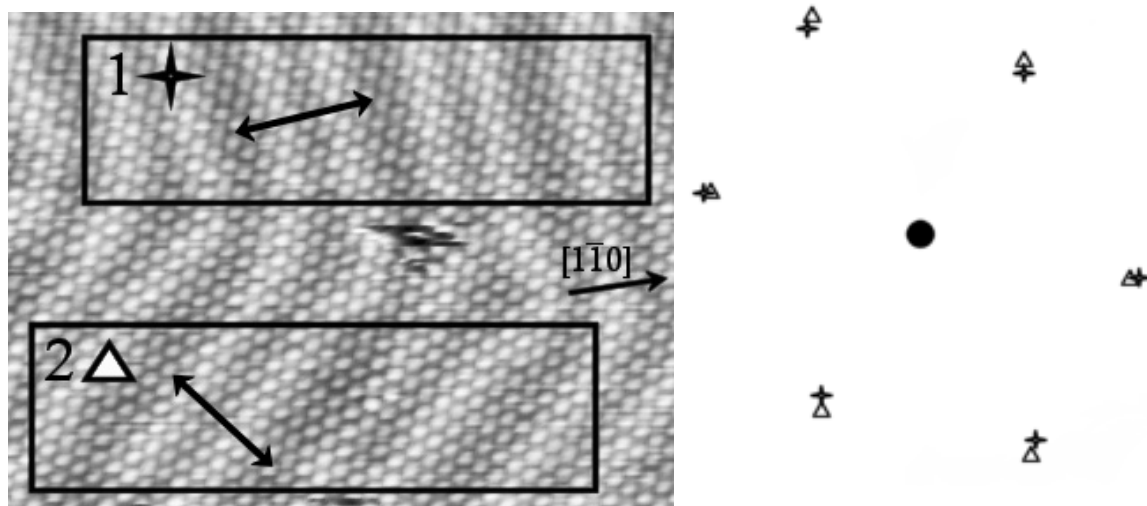


Figure 3.8: Left: STM image of a single molecular domain extending over two substrate reconstruction domains. The respective contraction directions are indicated by the double arrows. (image size $35 \times 22 \text{ nm}^2$, $I=0.4 \text{ nA}$, $V=-400 \text{ mV}$). Right: Fourier transform of the two regions marked 1 and 2, corresponding to the two orientations of the reconstruction detailed in table 3.1 and modeled in figure 3.9. While the intermolecular coupling scheme is maintained in the entire molecular layer, it adapts locally to the reconstructed gold lattice so that slightly different unit cell parameters are found in the two regions. Note that the Fourier image refers to the center of the spots which are in reality smeared because - apart from the experimental error - the local variations of the contracted interatomic distance around its mean value induces local variations of the intermolecular distances up to a few %.

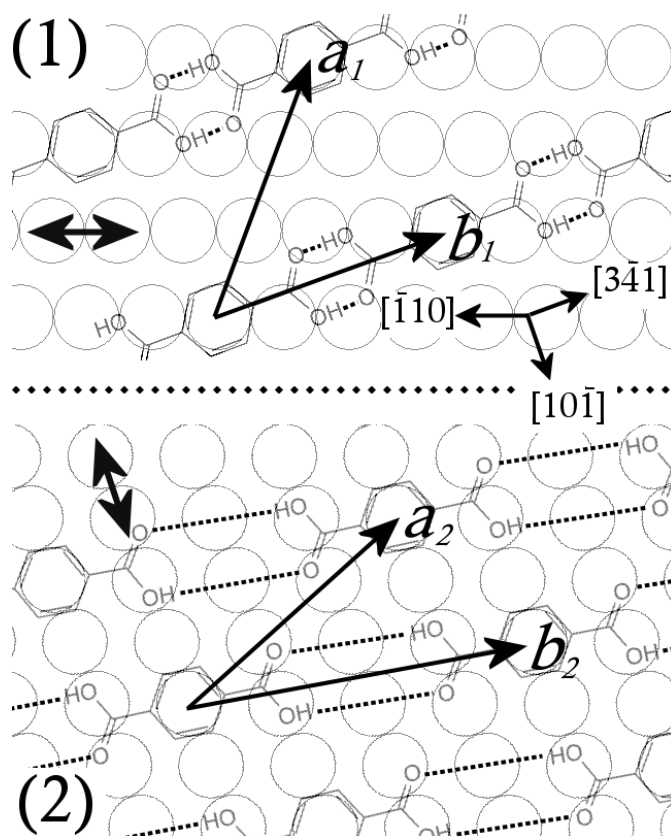


Figure 3.9: Model showing the effect of the uniaxial contraction of the $(22 \times \sqrt{3})$ reconstruction on the molecular superlattice. Note the differences in the H-bond lengths and in the molecular orientation. Domain types (1) and (2) correspond to those in table 3.1 and in the STM image of figure 3.8. The substrate atomic distances are greatly exaggerated to emphasize the differences in the molecular lattice. The contraction direction is indicated by a double arrow ($[\bar{1}\bar{1}0]$ in domain (1), $[\bar{1}01]$ in domain (2)). The complex structure of the substrate domain boundary is not represented.

type	reconstr.	a [Å]	b [Å]	γ	H-bond [Å]
1	$[\bar{1}\bar{1}0]$	$8.5^{\pm 0.1}$	$9.9^{\pm 0.3}$	46.5°	2.9 ± 0.3
2	$[\bar{1}01]$	$8.5^{\pm 0.1}$	$10.3^{\pm 0.1}$	44.4°	3.3 ± 0.1
3	$[01\bar{1}]$	$8.2^{\pm 0.3}$	$10.1^{\pm 0.2}$	47.3°	3.1 ± 0.2
bulk					2.6 [131]
TPA					2.7 [132]

Table 3.1: The dimensions of the molecular unit cell depend on its orientation relative to the substrate reconstruction. As a consequence variations of the respective model-derived H-bond distances are encountered. The error margin comes from the local modulation of the contracted interatomic distance around its mean value. a is parallel to the $[01\bar{1}]$ direction (see figures 3.4 and 3.9). The reconstruction indicates the contraction direction. For comparison, values from the bulk organic crystal are indicated.

molecules [84]. The situation is different for images acquired in solution as in Ref. [125] where various and not well understood effects may interfere. The resolution obtained in this case is still subjected to discussion [143]. Nevertheless it is possible for our system to characterize the hydrogen bond lengths between the molecules by analyzing the modeled superstructure. The three unit cells of table 3.1 give three different values for the distance between the oxygen atoms in the hydrogen bond. These are respectively 2.9 Å, 3.3 Å and 3.1 Å. While the contraction of the reconstructed substrate amounts locally to 4-6%, the differences in the hydrogen bond reaches up to 20% since a molecule extends over several gold atomic distances. These values (and similarly the lattice parameters a and b) are subject to further variations (up to about ± 0.3 Å) due to the periodic oscillations of the contracted interatomic distance around its mean value. The experimental verification of these substantial variations is hard to achieve on the molecular scale as they occur locally (changing from one molecule to its neighbor) and hardly can be measured. Only the mean global variations from one domain to the other can be clearly determined (Fig. 3.8), as in this case it is possible to average the distances over several molecular strides and hence reduce the error.

The presented values are calculated on the basis of the projected molecular length

of 7.02 Å (distance between the two extreme oxygen atoms, cf. figure 3.1) in the bulk phase [132]. For an adsorbed geometry the molecule is probably slightly distorted and the covalent bonds elongated [137, 144, 145]. As a comparison the stretching is ~ 0.2 Å for 4-[pyrid-4-yl-ethynyl] benzoic acid (PEBA) on Ag(111), a 13 Å long organic molecule containing two aromatic rings [146]. Furthermore the relaxation and therefore the equilibrium shape of the molecules within the superlattice may differ when the intermolecular distances are changed. Both effects can lead to modulations of the hydrogen bond length and induce a correction, which is however expected to be small.

DFT calculations

To examine the molecular distortions in more detail, DFT calculations were performed on a free one-dimensional molecular chain by A. Seitsonen from the University Zürich [147]. The system was taken as a free chain because the interaction of benzene-derived molecules (π -bonded) with noble metal surfaces is weak and poorly described by the exchange correlation functionals in the Kohn-Sham method [148]. Also since the adsorption on Au(111) proved to be especially weak the effect of the substrate on the molecules is small. The Vienna *ab initio* simulation package [149] was used, and the electron-ion interaction was described using the projector augmented wave method [150, 151]. A Generalized Gradient Approximation (GGA) was employed in the Kohn-Sham equations.

The DFT results are shown in figure 3.10. The maximum elongation calculated for the different domain configurations is of the order of +0.1 Å, whereby the main response pertains to the C-C bond between the carboxylic acid group and the aromatic ring. This value is fairly less than the variations reported in table 3.1. The calculations thus confirm that substantial distortions in the molecular layer occur. Furthermore, it appears that the H-bond lengths found are appreciably larger than in the TPA bulk phase. This difference suggest a moderate to weak character of the H-bridge in the adsorbed phase [152–154]. These findings are in agreement with the trend emerging for hydrogen-bonded systems at surfaces, where typically increased H-bond lengths occur [41, 146, 155].

Variations in the H-bond lengths are similarly encountered in the relaxation of TPA sheets at intralayer defects. As an example figure 3.11 shows such a long range relaxation of the molecular film in the vicinity of an edge dislocation. Note that the dislocation

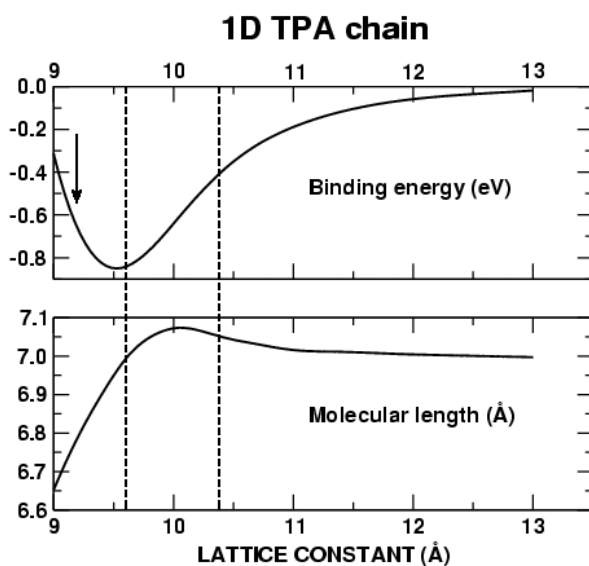


Figure 3.10: DFT calculations on a free 1D molecular chain illustrating the variations in the intermolecular binding energy (upper part) and in the molecular length (lower part) when varying the intermolecular distance. The dashed lines delimitate the lattice parameter range found in table 3.1. The arrow points to the expected lattice constant for TPA on Cu(111) (section 3.2). The results indicate minor variations in the molecular lengths. The variations in the binding energy (calculated per molecule) is only indicative, as the interaction with the substrate is not included in the calculations.

does not induce any change in the molecular organization of the surrounding area which consists of a single domain.

We could find no evidence in the STM data for a favored orientational domain as one could expect from the different hydrogen bonding characteristics. In order to find the domain of lowest energy we annealed the sample up to 350 K, but we could observe no apparent change in the layer. It is very difficult to gather correct statistics on the basis of the STM images because on the one hand a reconstruction domain can include several non-equivalent TPA domains and on the other hand a TPA domain can cover several reconstruction domains. In this case the complex structure of the substrate reconstruction domain boundary induces local distortions in the molecular superstructure which probably account for a soft transition from one domain type to the other. Nevertheless there is a correlation between reconstruction and molecular domain boundary as shown in figure 3.12. The molecular domain boundary usually follows the underlying reconstruction

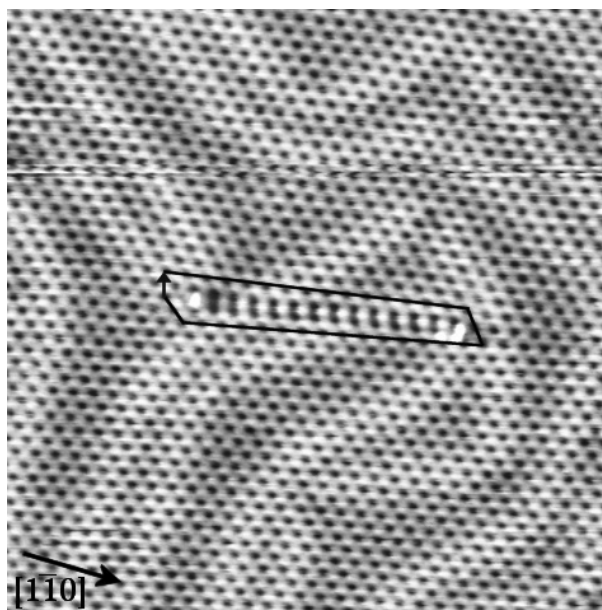


Figure 3.11: Edge dislocation in the molecular film; the Burger's vector is indicated. The contrast is reversed and the molecules are imaged as depressions (STM image size $27 \times 27 \text{ nm}^2$, $I=1.0 \text{ nA}$, $V=-360 \text{ mV}$).

boundary. The reason for a change in the molecular orientation from one domain to the other is not clear, and is not directly related to an optimization of the H-bond length, as every combination between the three possible types occur.

3.1.3 The 2D gas phase

Until now we described the dense phase formed by TPA on Au(111). As already mentioned this supramolecular ordering can also evolve locally for submonolayer coverages in arrangements that can be easily perturbed by the STM tip. TPA condensation does not occur for coverages below $\sim 0.5 \text{ ML}$, where the molecules are very mobile. However, they strongly influence the stability of substrate step atoms and consequently the surface reconstruction.

Figure 3.13 shows four STM images taken at time intervals of 4 to 10 minutes. The images are very noisy due to the molecules moving at a speed exceeding that of the scanning tip. The Au(111) surface and its step edges are known to be stable at room temperature [134], but here we observe fluctuating atomic steps reflecting an increased mobility of the edge atoms. The STM tip influence on step edge mobility cannot be excluded

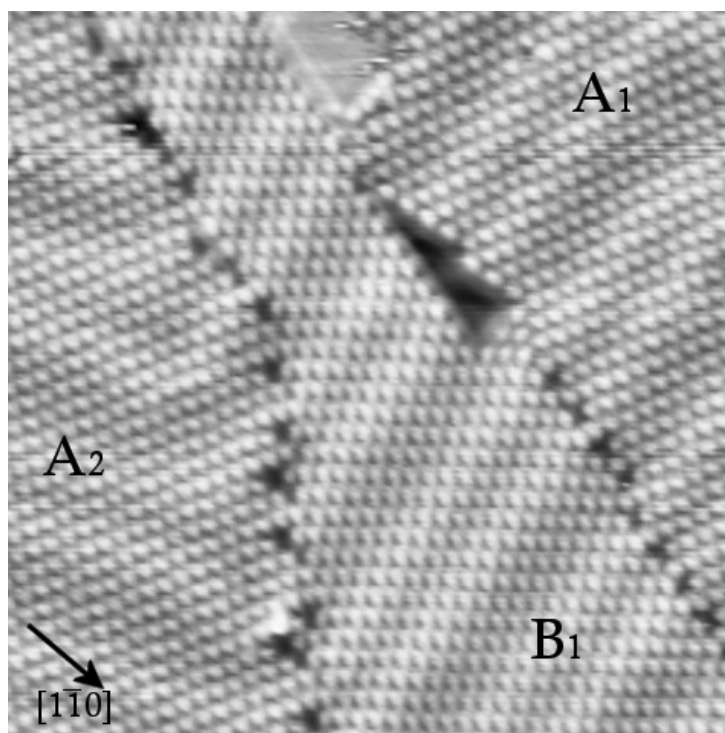


Figure 3.12: STM image illustrating the correlation between the Au(111) reconstruction domains and the molecular domain boundary. Different domains are labeled. The letter refers to the absolute orientation, the numerical index refers to the domain type detailed in table 3.1, i.e., the orientation relative to the underlying reconstruction domain (image size 29×29 nm², $I=0.5$ nA, $V=-180$ mV).

but is certainly not the decisive factor, as the tunneling resistance is not particularly low (180 M Ω) and the mobility observed is not related to the STM scan direction.

The increased step mobility is associated with a weakening of the lateral coupling of Au step atoms due to the presence of the molecular layer, analogous to the effect of small concentrations of alkali metals adsorbed on Au(111) [142, 156] and to the effect of the adsorption large molecules on other surfaces (see, e.g., Ref. [157]).

The reconstruction pattern which normally rearranges in the vicinity of the step edge is also influenced by this mobility. In figure 3.13 the reconstruction lines on the higher terrace tend to pass the step edge perpendicularly. As the step edge moves and changes shape and orientation, the reconstruction is modified in order to adapt the edge direction. In the last image the position of the step edge is not optimal (not fully aligned with preferred $\langle 1\bar{1}0 \rangle$ direction) and the reconstruction pattern still looks disordered. This

”moving reconstruction” is only visible in the vicinity of step edges: the molecules do not influence the gold surface and its reconstruction on large terraces.

The images shown here were acquired right after the sample preparation and the effect was similarly observable after one day, indicating that this is an equilibrium property of the system.

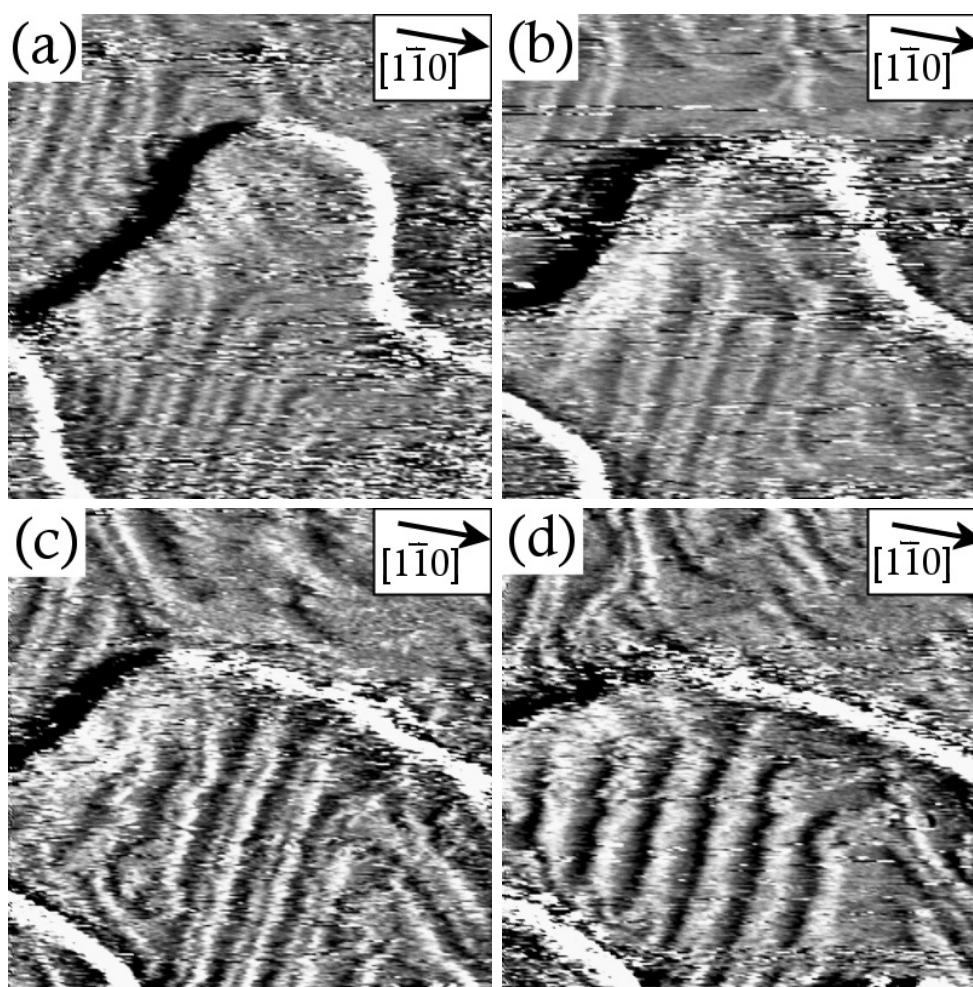


Figure 3.13: Series of STM images taken consecutively at the same area showing TPA-induced step edge mobility and related reconstruction rearrangements. The derivative of the topographic data is shown for better contrast. Time lap between the images: 4, 10 and 7 minutes, respectively (image size $62 \times 62 \text{ nm}^2$, $I=0.6 \text{ nA}$, $V=-110 \text{ mV}$, TPA coverage 0.5 ML, room temperature).

3.2 TPA on Cu(111)

We have shown that for the system TPA on Au(111) the local substrate geometry strongly influences the molecular superstructure, whereas the superlattice is always the same relative to the substrate atomic positions. As the surface contraction due to the reconstruction is in average equivalent in every rotational domain, the mean area of the molecular repeat unit is independent of its orientation relative to the substrate. Accordingly, the mean space available for a flat-lying molecule is unique for this system. It is thus interesting to vary this available space by changing the mean substrate interatomic distance. In comparison with an interatomic spacing of 2.84 \AA (2.75 \AA in the contracted direction) for the Au(111) surface, this distance amounts 2.56 \AA for Cu(111), an homogeneous metal surface with similar crystallographic symmetry. In fact, for the self-assembly of TPA on this surface, the molecular superlattice symmetry is identical and therefore the unit cell is smaller. As a consequence, the molecules lie too close to each other resulting in a compressive stress, and dislocations in the molecular layer occur.



Figure 3.14: Large scale image of the clean Cu(111) surface (STM image size $190 \times 100 \text{ nm}^2$, $I=0.2 \text{ nA}$, $V=-40 \text{ mV}$).

3.2.1 Description of the self-assembly

At submonolayer coverage, the TPA layer typically organizes on the Cu(111) surface as shown in figure 3.15. The molecular mobility at room temperature is much smaller than on the Au(111) surface and most of the molecules are imaged by STM. This is consistent

with the fact that Cu is more reactive than Au and with previous work on TPA on Cu(100) [130,158]. The molecules condense in large dense well-organized domains with a quasi-hexagonal lattice symmetry. The layer is imaged at a mean height equal to the bare substrate level, and the intralayer molecular corrugation is ~ 1.1 Å. Six different orientations of the domains are observed.

The molecules are responsible for a faceting of the copper surface (as compared with the typical morphology of clean Cu(111) as shown in figure 3.14). TPA interacts strongly with the step edges which are therefore normally decorated by a double row of molecules. The carboxyl group in the vicinity of a step edge is probably deprotonated to allow for the formation of a strong metal-carboxylate bond. The induced charge transfer modifies the electronic configuration of the molecule and the second carboxyl group is probably more reactive for the formation of a hydrogen bond, and therefore always bond to a second molecule [159].

Carboxylic acids frequently deprotonate upon deposition on a copper surface at room temperature, leading even in some cases to an upright orientation of the molecules [135, 158,160,161]. On Cu(110), TPA molecules are deprotonated and lying flat at low coverage or standing upright at higher coverage [135]. On Cu(100) the TPA are also deprotonated but are lying flat at any coverage (submonolayer) [158]. The present observations suggest that on Cu(111) the TPA molecules are lying flat and are not deprotonated in the domain phase. The oval shape of the molecules in the STM images, their longitudinal regular alignment inside the domains and the intermolecular distances measured constitute coherent indications for the formation of flat-lying hydrogen-bonded linear motifs (Fig. 3.1). Deprotonation occurs probably only for the carboxyl groups directly in contact with step edges and not for the molecules on terraces. This statement is consistent with the fact that a *fcc*(111) surface is more inert than the (100) orientation. However, this could not be unambiguously demonstrated on the basis of the STM data, and further experiments with X-ray Photoelectron Spectroscopy (XPS) and Near-Edge X-ray Absorption Fine Structure (NEXAFS) techniques are in preparation for conclusive confirmation.

The substrate step edge directions do not reflect the threefold (111)-surface symmetry but are parallel to one of the possible molecular lattice axes. It is thus the orientation of the molecular "domain" (which can be reduced to a seed of two rows) that determines the step edge orientation through one of its high-symmetry directions. This is illustrated in

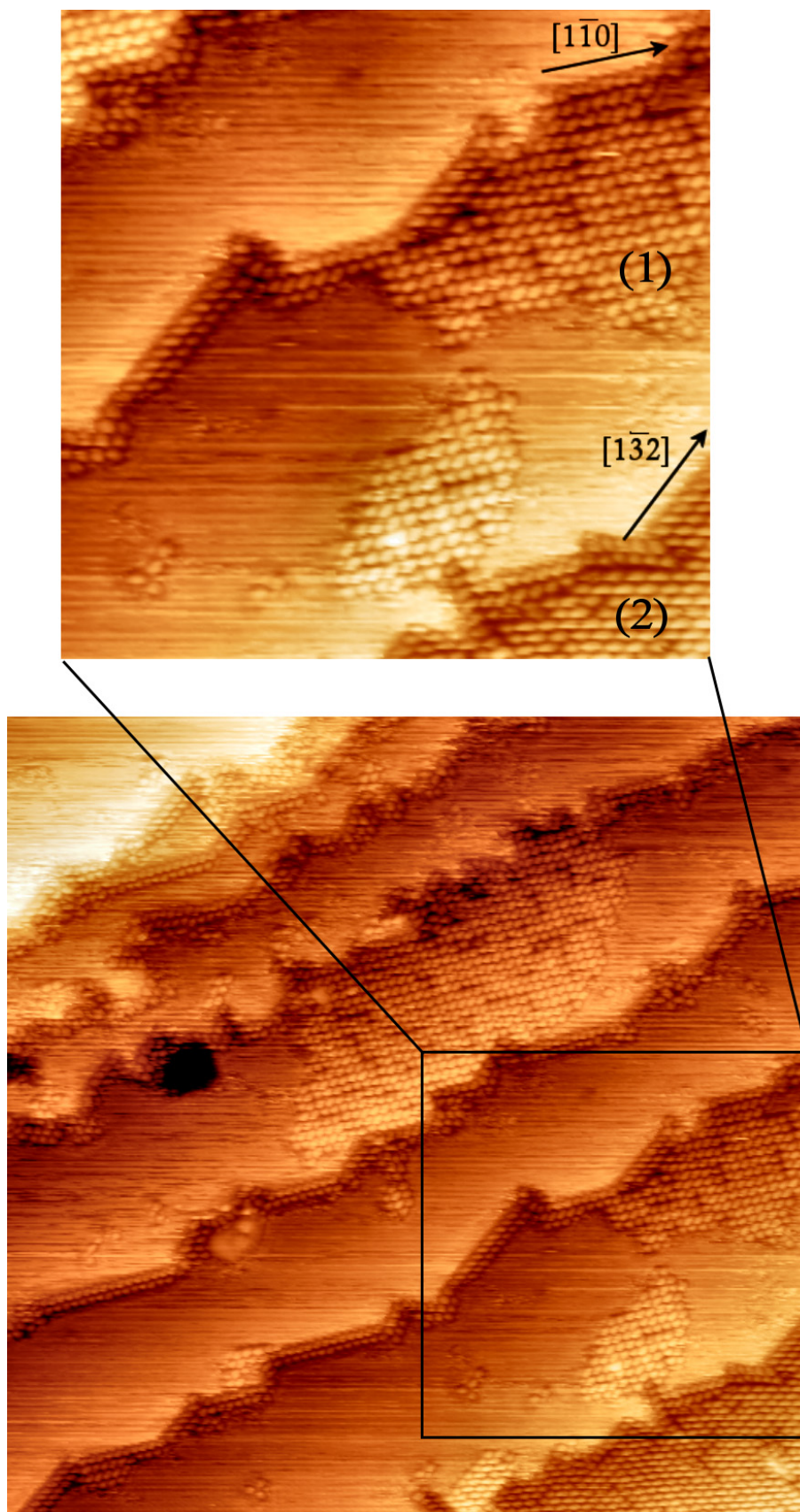


Figure 3.15: Typical organization of TPA on the Cu(111) surface. The substrate step edges are decorated by two rows of molecules which drive local faceting orientation (see text) (STM image size $60 \times 60 \text{ nm}^2$, $I=0.5 \text{ nA}$, $V=-0.5 \text{ V}$).

Fig. 3.15 where the domain labeled (1) induces the $[1\bar{1}0]$ -orientation of the step edge (which corresponds actually also to the close-packed direction of the substrate), whereas $[1\bar{3}2]$ -step edges correspond to the molecular orientation of the domain labeled (2). Similar surface faceting induced by organic adsorbates has been already reported on various systems, especially on (110)-oriented metal substrates [157, 159, 162–165].

3.2.2 Dislocations in the molecular layer

Similar to TPA on Au(111) we can model the TPA adsorption on Cu(111) by a commensurate quasi-hexagonal superstructure. The model is obtained by seeking a commensurate superlattice fitting best to the mean intermolecular distances and angles measured in the STM images. The superlattice thus retained is shown in figure 3.16, any other possible superstructure being rejected because of too large discrepancy with regard to the one observed. The molecular periodicity found relative to the substrate atomic lattice is actually identical to the case TPA/Au(111) (Fig. 3.5), and the same characteristics are encountered, i.e., the presence of three rotational domains for each chiral species that define six distinct domain orientations. However, on Cu(111) the ideal superlattice would be more dense due to the smaller substrate interatomic distances, leading to too small intermolecular distances. This model is thus idealized and does not reflect the exact supramolecular arrangement.

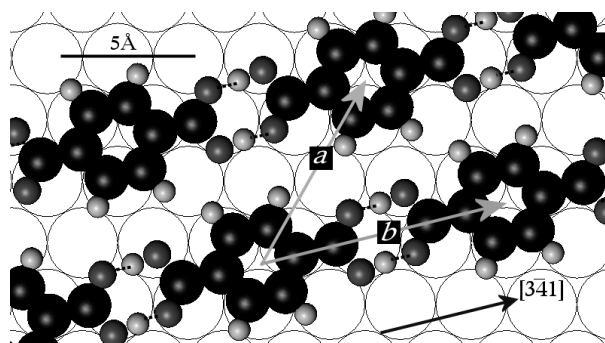


Figure 3.16: Model for an idealized molecular superlattice of TPA on the Cu(111) surface. The molecules are obviously lying too close to each other, resulting to dislocations in the real case.

By carefully looking at the molecular domains one observes dark spots in the layer corresponding to a larger intermolecular distance along the $\langle 3\bar{4}1 \rangle$ (longitudinal) direction. The difference corresponds to a few substrate atomic periodicities. One of the two

molecules neighboring the vacancy can hop into it, resulting in a quasi-linear diffusion of the defect. At room temperature the diffusion time constant is close to STM imaging time, so that it is possible to observe the motion of the vacancies. Figure 3.17 shows two images of a molecular domain taken at a 2 minutes time interval, illustrating this diffusion.

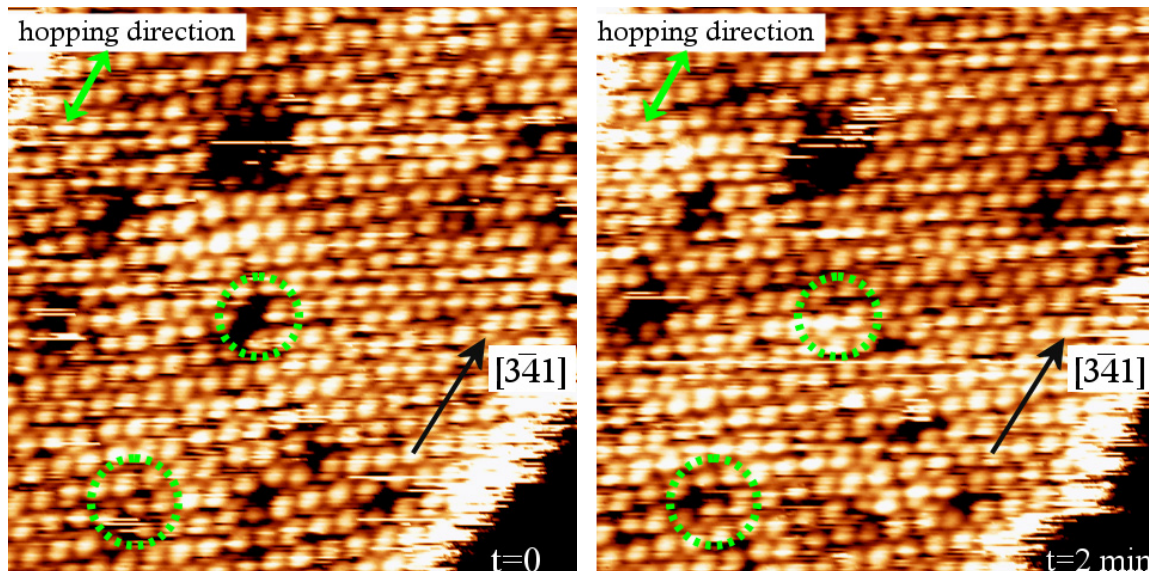


Figure 3.17: Moving dislocations in TPA/Cu(111). The green circles indicate positions where free room inside a molecular row is created or annihilated by hopping of the neighboring molecules in the $\langle 3\bar{4}1 \rangle$ direction. Note that the molecular layer is apparently not flat and exhibits a long-range irregular height-modulation of about 0.1 \AA which is also changing position with time (STM image size $15 \times 15 \text{ nm}^2$, $I=0.3 \text{ nA}$, $V=-0.4 \text{ V}$, time between the two frames: 2 minutes).

The intermolecular distances for a perfect (defect-free) layer are reported in table 3.2 and compared with the case TPA/Au(111) and TPA in the bulk phase. Note that the lattice parameter a and therefore the unit cell area are irrelevant in the case of bulk TPA because the 3D phase does not simply consist in a stacking of 2D sheets [132]. It comes out clearly that the commensurate defect-free structure would result in a much too dense layer with intermolecular repulsion (see Fig. 3.10, for a free chain with a longitudinal lattice constant of 9.2 \AA the hydrogen bond is repulsive). The layer relaxes by creating defects in the $\langle 3\bar{4}1 \rangle$ direction. However, this relaxation is not sufficient to compensate completely the stress as the defect concentration is low. The remaining compressive stress probably causes the large and irregular brighter areas of Fig. 3.17 corresponding to an

	a [Å]	b [Å]	γ	Area [Å ²]	H-bond [Å]
TPA/Cu(111)	7.7	9.2	46.1	51	(2.2)
TPA/Au(111)	7.9–8.6	9.6–10.3		59–64	2.6–3.4
TPA/Pt(111) [125]	7.3	9.6	49.1	53	2.6
bulk TPA [132]		9.7			2.7

Table 3.2: The dimensions of the molecular unit cell for a virtual defect-free layer of TPA on Cu(111). The area of the unit cell represents the available 2D space per molecule. The hydrogen bond length is calculated on a basis of an undistorted molecule. The results are compared with the case of the layer phase on Au(111) (the two extreme values found locally in the different domains are given, see table 3.1) and on Pt(111) from Ref. [125], and with the bulk phase. The density is too high on Cu(111), and defects are created.

increase of about 0.1 Å in the apparent molecular layer height. The high symmetry bonding site is possibly not strictly retained, leading to minute out-of-plane rotations of the molecules, or to the formation of an irregular Moiré pattern reflecting occupations of different substrate sites. The diffusive motion of these bright areas is complex and not obviously related to the motion of the point defects. Furthermore, the motion of a molecule in a $\langle 3\bar{4}1 \rangle$ (longitudinal) direction is probably not strictly linear, thus leading to simultaneous lateral rearrangement. The relaxation of the stress corresponds therefore to a global and collective reorganization of the molecular sheet.

With the system TPA on the Cu(111) surface we thus encounter the unusual situation that the balance of molecule-substrate and intermolecular lateral interactions does not account for a regular ordering in the organic layer.

Chapter 4

Metallosupramolecular Nanoarchitectures

In this chapter we address metal-ligand interactions to link organic species to transition metal centers and construct metallosupramolecular architectures at surfaces. These interactions are characterized by intermediate strength relative to weak interactions (as hydrogen bonding) and strong covalent bonds (e.g., carbon-carbon) of most organic compounds [166]. Therefore the structures obtained are generally more robust than the supramolecular assemblies presented in chapter 3, but with appropriate systems their formation reaction may still easily proceed at room temperature [126].

Metal-organic coordination networks (MOCN) have been realized in three-dimensional bulk materials [28, 47, 48, 124, 167–170]. Their synthesis is motivated by the rational design principle, i.e., assembling well-defined and rigid molecular building blocks into predesigned ordered structures. These materials have gained wide attentions because of their high stability, tunable dimensions, (nano)porosity and chemical functionality, and may find various applications in molecular recognition, catalysis, gas storage and separation, etc. For many of these applications, the controlled nanoscale fabrication of functional molecular architectures at solid substrates is desirable [171–173]. However, little is known on the handling and assembly of such systems on surfaces [57–59].

Here we use as a linker again the molecule Terephthalic Acid - TPA (see Fig. 1 page 5), and cobalt and iron as metal centers. In the presence of transition metals carboxylic acids usually undergo deprotonation and a metal-carboxylate bond is formed, representing the basic step for the construction of coordination structures. The system Fe-TPA

has been extensively studied on the Cu(100) surface [130]. It organizes in various well-ordered phases with square or rectangular unit cells, forming a variety of low-dimensional arrangements including MOCN. Here the substrate used is Au(111). The peculiar symmetry of the compounds obtained does not match with the substrate symmetry, and their ordering is consequently poor. On the other hand *in situ* observation of the dynamics of Fe-TPA and Co-TPA network formation is possible. Furthermore, the use of Au(111) is of interest because its surface reconstruction provides a regular mesoscopic patterning which drives the large-scale organization of the metal-organic structures. Specific patterns directly related to the inhomogeneities of the reconstructed Au(111) were already obtained by molecular self-assembly by other groups [5, 7, 37], where the intermolecular driving force consists of hydrogen bonding or weak interaction. We report micro- and mesoscopic arrangements obtained by strong metal-ligand bonds, and where the influence of the Au(111) chevron structure is straightforward.

In the following one monolayer (ML) refers to a complete monoatomic layer of Fe and to half of a biatomic layer of Co on Au(111). For TPA, one monolayer refers to a complete layer of the dense hydrogen-bonded phase.

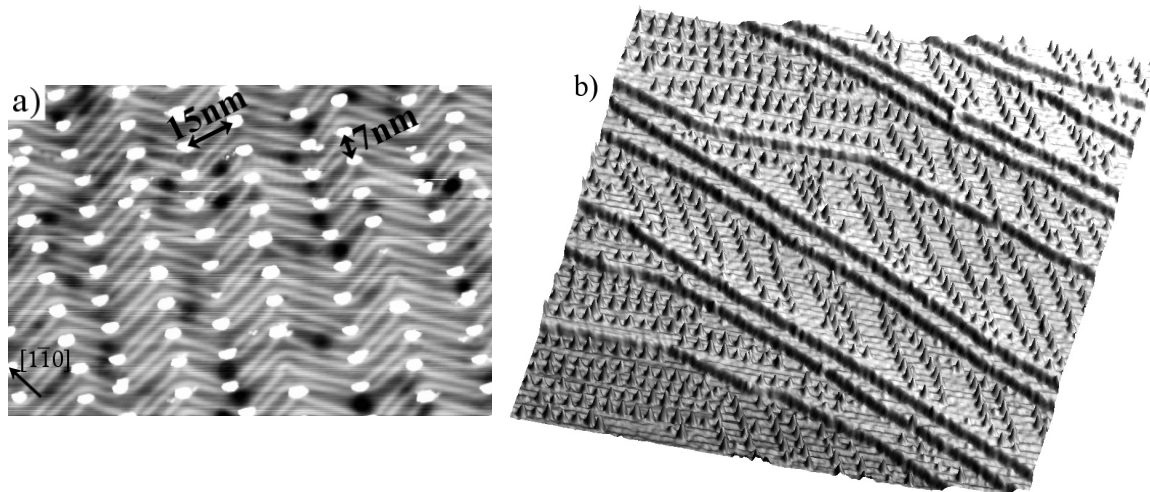


Figure 4.1: a) Deposition of 0.07 ML of Fe on the Au(111) surface at room temperature. The impurity atoms segregate at the elbow sites of the surface reconstruction pattern to form a regular mesoscopic array of monolayer islands. (STM image size $100 \times 80 \text{ nm}^2$, $I=1.3 \text{ nA}$, $V=20 \text{ mV}$). b) Large scale image of 0.14 ML of Co deposited on Au(111). The islands are bilayered (STM image size $300 \times 300 \text{ nm}^2$, $I=0.8 \text{ nA}$, $V=-25 \text{ mV}$).

4.1 Mesoscopic patterning of the Au(111) surface by deposition of metallic impurities

The reconstructed ($22 \times \sqrt{3}$) Au(111) surface as described section 3.1.2 page 49 and the regular pattern formed by the chevron structure can be used as a template for epitaxial growth. The complex atomic structure of the turns in the reconstruction lines (the elbows) causes atoms with decreased (5) or increased (7) surface coordination as compared to an ideal hexagonal lattice (6). These sites have thus a particular reactivity [174] and show a preferential nucleation for impurities. Adatoms like Co, Fe or Ni deposited on Au(111) nucleate at the elbow sites of the surface reconstruction to build monolayer (Fe [175] and Ni [176]) or bilayer (Co [177]) regularly distributed islands at room temperature (see figure 4.1). The lattice unit is close to rectangular with dimensions about $7 \times 15 \text{ nm}^2$, but is not homogeneous over the whole surface and follows the orientation of the reconstruction domains. Hence defects occur, especially in the vicinity of step edges. A deposition of 0.1 ML produces islands consisting of in average about 140 atoms.

Surface states

For the surface state electrons of the Au(111) surface the metallic clusters as described above act as specific scattering centers, in addition to step edges and lattice defects. This leads to interferences between the incoming and the reflected 2D electronic states and to the formation of a complex standing wave pattern. The resulting modulations of the LDOS at the Fermi level are visible by STM at low sample bias (see section 2.5 page 39 for further details). Figure 4.2 shows a STM image obtained at a temperature of 5 K on Au(111) where Fe was previously deposited. The Fe islands are hardly visible on the image because the derivative of the topographic data is reported in order to enhance contrast on the standing waves. Nevertheless, the topography is very similar to what is shown Fig. 4.1 (a). The centrosymmetry of the Fourier transform of the image (inset) reveals the isotropy of the surface state in the surface plane. We measured an electron wave length at the Fermi level of $36.5 \pm 1.0 \text{ \AA}$, in agreement with previous work on pure Au(111) surface [72].

The oscillatory behavior of the electronic properties due to the interferences of the surface state produces oscillations in the potential energy of the surface, i.e., a defined

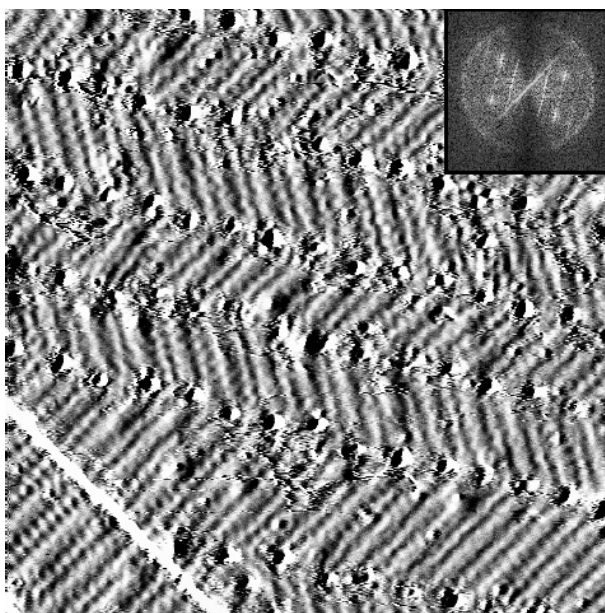


Figure 4.2: Standing waves on Au(111) in the presence of adsorbed Fe (same preparation conditions as in Fig. 4.1 (a)). The interference pattern is caused by scattering of the surface state electrons at step edges and at Fe islands located at the elbows sites of the reconstruction. The derivative of the topographic data is shown for better contrast. Inset: the circle obtained in the Fourier transform corresponds to the Fermi surface of the Shockley surface state, and the dots to the surface reconstruction pattern (STM image size $100 \times 100 \text{ nm}^2$, $I=0.4 \text{ nA}$, $V=-10 \text{ mV}$, $T=5 \text{ K}$, Fe coverage 0.05 ML).

periodicity in potential wells, which mediates long-range interactions between adsorbates [178, 179]. In certain cases this can lead to the formation of well-ordered superlattices of adatoms at low temperature [180]. With the system Co or Fe on Au(111) these interactions are much too weak in comparison with the modifications of the surface atom reactivity due to the surface reconstruction. For a deposition at room temperature we did not observe any correlation neither between the standing wave pattern and the metallic cluster superstructure, nor with the molecular assembly described below.

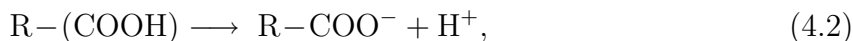
4.2 Exploiting the Fe,Co/Au(111) template to monitor coordination reactions

Gold is a rather poorly reactive substrate, and iron and cobalt are good candidates for carboxylate engineering [59,181]. Therefore, the metallic islands of Fig. 4.1 can be seen as *in situ* nano-reservoirs for the molecules deposited on this surface to form metal-organic architectures. Figure 4.3 (a) shows the structure obtained after deposition of 0.3 ML of TPA on 0.08 ML of Co on Au(111) at room temperature. Each Co cluster contained initially about 110 atoms. Two distinct phases are observed. In the lower part of the image a large close-packed organic domain is formed, whose structure is identical to that of the domains obtained with only TPA on Au(111), featuring similarly the characteristic height modulation of the surface reconstruction (see Fig. 3.3). Here the complexation did not occur and the intermolecular cohesion is governed by hydrogen bonding, the Co islands being simply trapped in the layer. By contrast, in the upper part of the image, a different open network structure is emerging, where the size of the Co islands is reduced, providing evidence for their dissolution and the formation of metal-organic compounds. The latter decorate the Co dots and irregular clusters are formed. In between, highly mobile molecules in a 2D gas phase create the noisy background observed. Molecules may stick to the border of these clusters or be released by formation/dissociation of lateral linkages. The kinetics of this reaction provides a time constant of the order of a minute at room temperature. The shape of the clusters is thus changing from frame to frame while imaging it with STM. In particular, figure 4.3 (b) shows one of these clusters evolving with time. In frame #2 (after 10 minutes) the size (brightness) of the metallic core is decreased, and more metal-organic complexes are anchored to it, thus revealing that a coordination reaction occurred. In frame #3 (after further 15 minutes), however, the clusters contains less complexes indicating that dissociation or diffusion occurred.

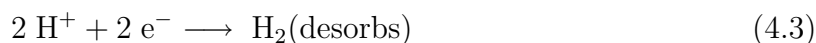
The presence of coordination structures gives evidence for the deprotonation of the molecular carboxyl groups. While on pure Au(111) the acidic character is preserved and allows for the formation of H-bridges, in the presence of Co adatoms TPA readily reacts to form diterephthalate, which is engaged in the formation of metal-ligand bonds. This chemical reaction can be represented by the following equation:



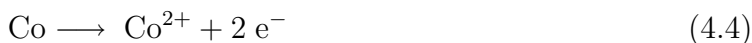
Atomic hydrogen is not stable on a noble metal surface at room temperature and recombines into molecular hydrogen which desorbs [182]. The thermodynamical equilibrium state of reaction (4.1) is therefore highly displaced to the right due to the disappearance of one of its products. From the formal point of view of electron transfer, the desorbed hydrogen molecule takes over the electrical charge which is necessary for the oxidation of the metal center. After deprotonation of the carboxyl group



the formal redox semi-equations can be represented as



and



The oxidation state Co^{II} proposed is at this point only indicative. Its proper determination is the subject of the next chapter. Furthermore, depending on the structure obtained the stoichiometry may vary, as it must be the case for the true 1D link presented in section 4.3. The mechanism described above provides therefore a simple and general picture which does not take into account the influence of the substrate. The latter may be significant, in particular concerning charge transfer and the participation of formally charged species (terephthalate).

The nanoporous networks show a characteristic decoration at their borders where the grid motif of the interior is not continued. This phenomenon is understood as follows: formally negatively charged carboxylate is reactive for hydrogen bond formation with the hydrogens of a benzene ring, thus leading to the peculiar perpendicular coupling between two molecules as shown in figure 4.6. This particular bonding scheme is characteristic of the dimensionality of the system, and is typically not observable in three dimensions. In fact, each molecule involved in a metal-organic bond through only one of its carboxylate group (i.e., a molecule at the rim of a cluster) forms such a hydrogen bridge with its second carboxylate group, as indicated, e.g., on the location marked by the arrow in Fig. 4.5. As a consequence, we can deduce that the deprotonation reaction is mediated by the presence of Co, and takes place for both of the carboxyl groups, but does not necessarily lead to the formation of a stable metal-ligand bond.

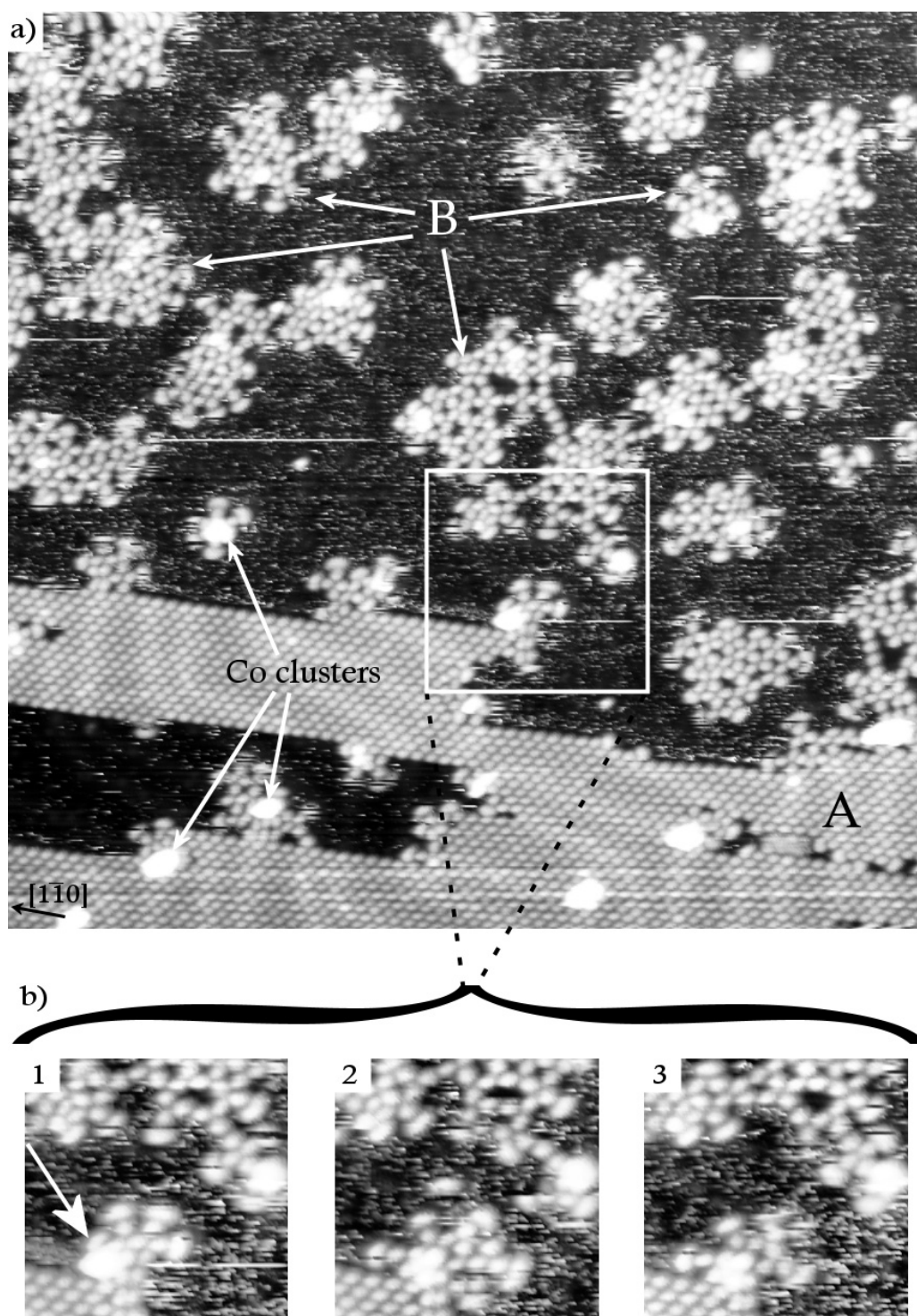


Figure 4.3: a) Deposition of 0.3 ML of TPA on Co dots (0.08 ML, corresponding to about 110 atoms per dot) on the Au(111) surface at room temperature. Hydrogen-bonded domains (A) coexist with metal-organic complexes (B) (STM image size $60 \times 60 \text{ nm}^2$, $I=0.6 \text{ nA}$, $V=-0.7 \text{ V}$). b) The same area as denoted by the white frame imaged at different times (0, 10, and 25 minutes). Some of the cobalt atoms from the core of the cluster (pointed by the arrow) react to form complexes, which then partly dissociate.

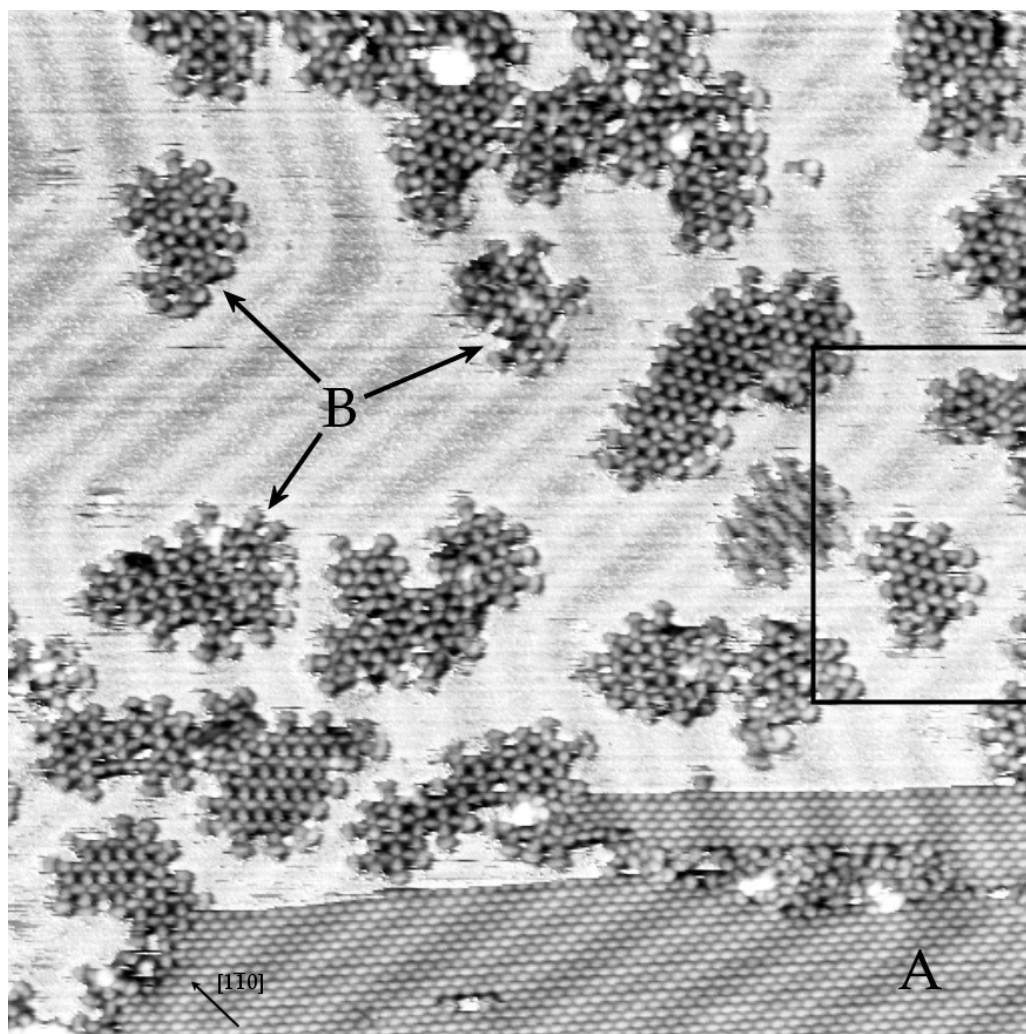


Figure 4.4: Same sample as in Fig. 4.3, after annealing at 330 K. Hydrogen-bonded domains (A) still coexist with coordination islands (B). The annealing resulted in the almost complete dissolution of the metal islands and the formation of nanoporous metal-organic nanogrids (STM image size $60 \times 60 \text{ nm}^2$, $I=0.6 \text{ nA}$, $V=-0.7 \text{ V}$).

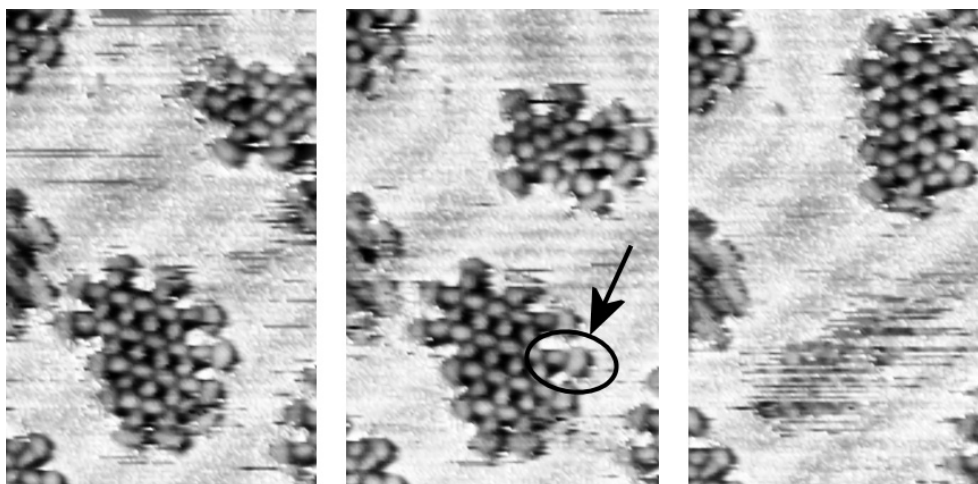


Figure 4.5: Imaging the same area (denoted by the black frame in Fig. 4.4) at different times (0, 15, and 30 minutes resp.) allows for *in situ* monitoring of the metallosupramolecular self-assembly and its formation-dissociation dynamics. The arrow points to a particular lateral hydrogen bonding, as schematically detailed Fig. 4.6 (STM image size $13 \times 20 \text{ nm}^2$, $I=0.6 \text{ nA}$, $V=-0.7 \text{ V}$).

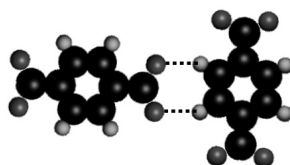


Figure 4.6: Particular hydrogen-bonding scheme between two TPA obtained as a consequence of the deprotonation of the carboxyl groups. This coupling is encountered as a typical decoration of the nanogrid borders.

Figure 4.4 shows the same sample after annealing for 20 minutes at 330 K. Domains of hydrogen-bonded TPA are still present with Co islands trapped in it (lower part). The density and the cohesion of these domains are obviously so high that the steric hindering prevents from any diffusion and reactivity with cobalt. In the upper part the metal-organic complexes are well developed and organize in square or rectangular lattices (nano-grids), surrounded by a 2D gas formed by highly mobile Co and TPA species. Here again, we can directly monitor *in situ* the metallosupramolecular self-assembly and its dynamics. The nanogrid domains can change their shape and rearrange their internal structure, and even move or dissociate completely. Figure 4.5 shows a sequence of STM images illustrating the evolution of two such domains with time.

Due to the annealing all the Co atoms from the islands were consumed in Co-carboxylate formation. It is thus thermodynamically more favorable to break the strong metallic bond in the islands, which can be of the order of several eV per atom for a free cluster [183], to form metal-carboxylate bonds. This reaction is first set off by the irreversible deprotonation of the carboxyl groups. In comparison with the system formed by the separated reactants - Co in a cluster and diterephthalate, organizing the compounds in nanogrids corresponds thus to a gain in free energy.

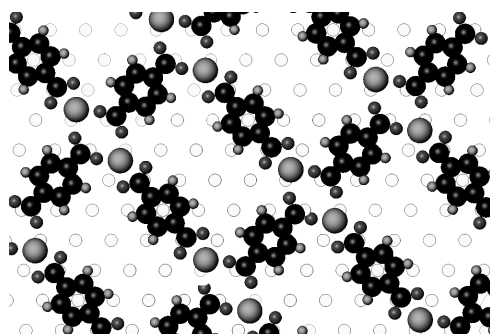


Figure 4.7: Tentative model for a commensurate rectangular metal-organic nanogrid corresponding to a Co-TPA stoichiometry of 1-1. The geometry is inspired from the structure of Fe-TPA on the Cu(100) surface (see Fig. 5.4).

Structure of the nanogrids

Because of the reduced size of the ordered domains and the various possible orientations the exact structure of the nanogrids could not be precisely elucidated. It is probably closely related to similar grids observed with TPA or other ditopic carboxylate linkers and Fe on Cu(100) [59, 130], where the repeating unit consists of two metal atoms surrounded by four molecules. The relative orientation of the metal pairs in neighboring compounds determines a rectangular (same orientation of di-iron pairs) or a square lattice (alternating orientation), as described in Fig. 5.4 on page 94. However, the hexagonal Au(111) surface is not well suited for the anchoring of a rectangular superlattice. The precise structure is therefore subject to the substrate modulations and probably not exactly periodic. A possible structure arrangement is shown in the tentative model depicted in figure 4.7. As a result of this complexity we observe the coexistence of a large number of different domains of reduced size and with various orientations. Efforts to improve ordering by different sample preparations never led to the formation of nanogrid domains larger

than a few tens of nm. The fact that the coordination compounds do not coherently adapt their structure to the substrate hexagonal symmetry strongly indicates that the shape of these Co/TPA compounds at surfaces is intrinsically square-grid. The strong directional metal-ligand bond is decisive for the determination of the precise relative geometry of its reactants, dominating over the symmetry of the poorly reactive substrate.

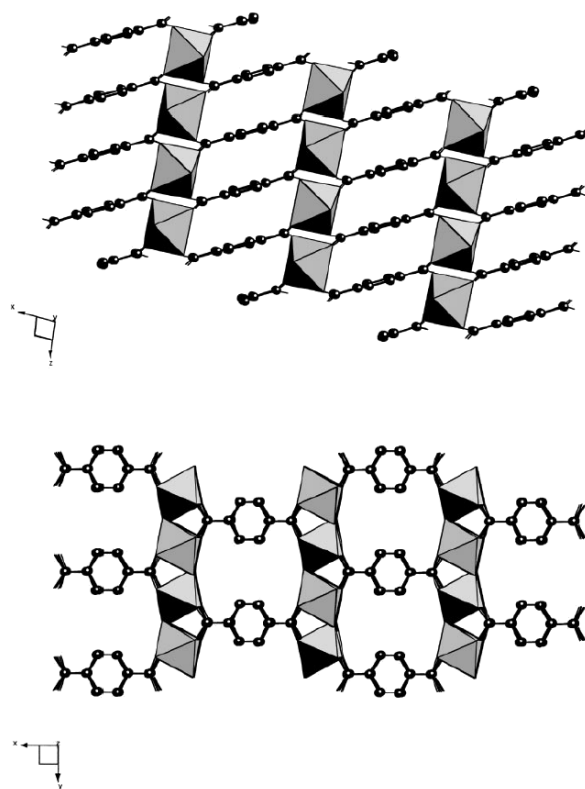


Figure 4.8: Projections of the 3D crystal structure of $\text{Co}(\text{H}_2\text{O})_2\text{TPA}$ where the Co atoms occupy octahedral sites (from Ref. [181]).

However, because of the effect of the adsorption on a substrate and the related reduced dimensionality of this system, novel geometries are obtained. For comparison, the 3D crystal structure of Co-TPA complexes (in the presence of water molecules) is represented in figure 4.8. For this compound, the typical octahedral symmetry of the metal center is encountered. This geometry is not directly adaptable on a surface, where different structures with lower coordination and lower symmetry of the metal centers evolve. The lowering of the coordination probably leads to unsaturated metallic orbitals, as it is observed with other surface compounds where the chemical reactivity of unsaturated sites have proven to be decisive for heterogeneous catalysis [184, 185]. The symmetry of

the metal centers in the nanogrids is square planar. For the one-dimensional structure presented below the symmetry is even lower. Compared with a relaxed 3D bulk structure, the symmetry reduction determines a new crystal field geometry. Even if the latter and its influence on the electronic orbital symmetry are not precisely known yet, a first characterization is proposed in the next chapter.

In contrast to the case Fe/TPA on Cu(100) [130], where the identification of the Fe atom position is straightforward, no direct topographic evidence for the position of the metal centers on Au(111) was found. The electronic structure and the precise geometry of the total system needs to be investigated to understand this feature [84].

It is also interesting to note that on the Cu(100) surface no Co-TPA metal-organic compounds evolve. The Fe-TPA system on this surface presents large homogeneous well-ordered nanogrid structures. In comparison, the system Co or Fe and TPA on Au(111) preserves its intrinsic square shape but is much more flexible and leads to the formation of a large variety of nanoarchitectures.

4.3 Metal-organic nano-texturing

By controlling the deposition parameters and the relative metal/TPA stoichiometry, it is possible to steer the formation of different nanoarchitectures on Au(111). We tried various combinations with both Co or Fe as a metal center. The same deposition conditions as described in the previous section but with Fe instead of Co lead to similar results. The structures observed are similar, and the dissolution of the Fe clusters occurs. However the Fe-ligand interaction seems to be slightly weaker than with Co and the nanogrids formed are less organized and limited to domains of smaller dimensions (see figure 4.9).

The important parameters during the deposition are the sample temperature (from room temperature to 400 K), the total and relative amount of deposited species, and whether the metal or the ligand is deposited first. Some STM measurements were performed at low temperature in order to inhibit the adsorbate mobility, but no structural change was observed with varying temperature.

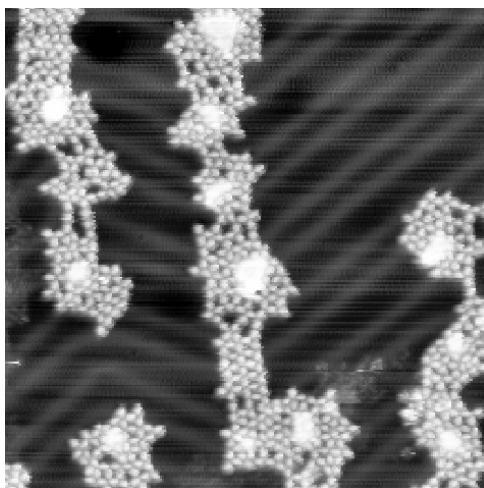


Figure 4.9: Deposition of 0.1 ML of Fe followed by deposition of 0.4 ML TPA on Au(111) kept at 330 K. In comparison with Co, and with equivalent deposition conditions, the coordination structures are similar but slightly less ordered (STM image size $43 \times 43 \text{ nm}^2$, $I=0.5 \text{ nA}$, $V=-0.5 \text{ V}$, taken at 5 K).

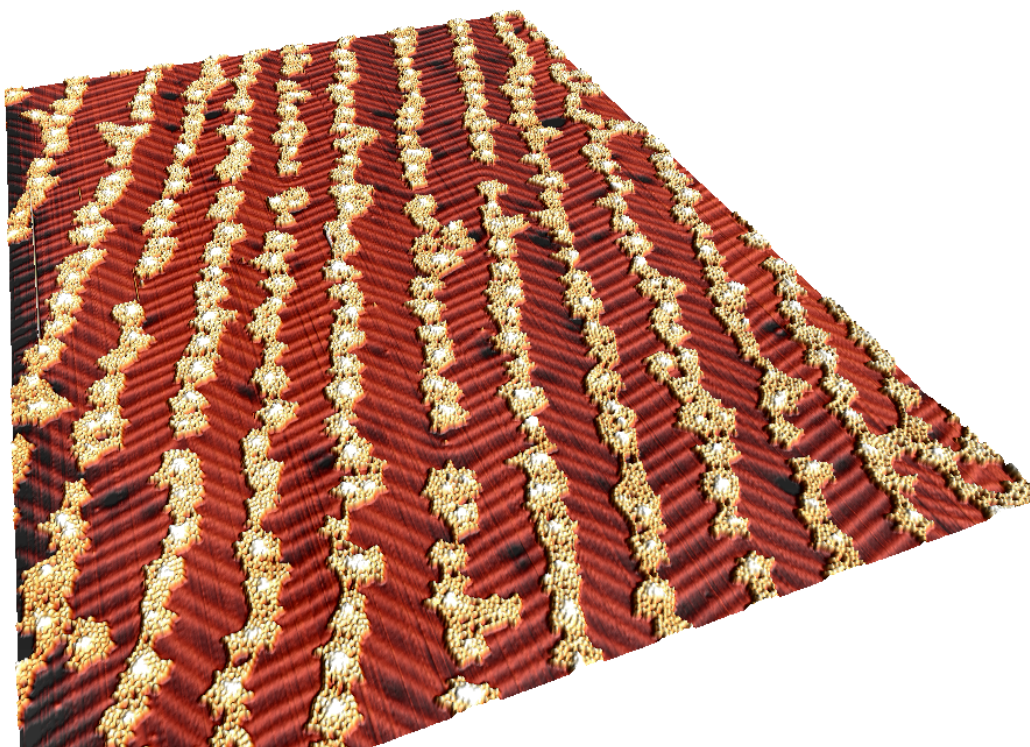


Figure 4.10: Deposition of 0.1 ML of Fe followed by deposition of 0.4 ML TPA on Au(111) kept at 330 K. The periodic pattern of the substrate reconstruction leads to the formation of mesoscopic stripes of coordination compounds (STM image size $200 \times 160 \text{ nm}^2$, $I=0.8 \text{ nA}$, $V=-1.5 \text{ V}$, taken at 5 K).

Mesoscopic stripes of coordination compounds

When the total area of the coordination structures organized around the previously deposited metal dots is increased, they start to coalesce. As the superstructure of the Au elbow sites is rectangular the coalescence takes place first unidirectionally along the smaller periodicity. Moreover, the substrate reactivity is probably higher in this direction because of the peculiar atomic structure of the reconstruction, thus leading to a preferential adhesion of the adsorbates along this direction. Stripes of metal-organic compounds are thus obtained, as shown in figure 4.10. The stripe width typically amounts about 10 nm whereas the length can be as large as the terrace size: the lines extend to several hundreds of nm.

The long-range mesoscopic order reflecting the dislocation pattern of the substrate reconstruction is thus high. However, the nanogrids themselves are poorly ordered, related

to the fact that Fe is used and that the relative stoichiometry Fe/TPA is not optimum. A higher annealing temperature does not lead to an improved ordering of the nanogrids. On the contrary, for a temperature of 350 K to 400 K rather amorphous structures are obtained (see figure 4.11). This may be due partly to the incorporation of Fe into the Au surface layer.

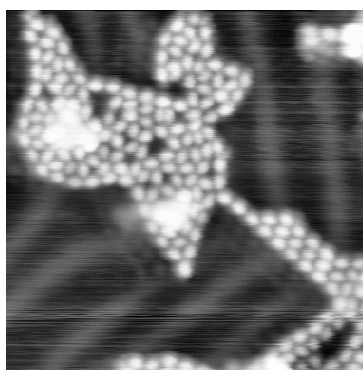


Figure 4.11: Deposition of 0.1 ML of Fe followed by deposition of 0.3 ML TPA on Au(111) kept at 380 K. For a deposition at high temperature an amorphous structure is obtained (STM image size $20 \times 20 \text{ nm}^2$, $I=0.8 \text{ nA}$, $V=-1.0 \text{ V}$, taken at 5 K).

Labyrinth-like structure

The chevron structure of the reconstructed Au(111) surface and therefore the superlattice of the metal clusters comprise usually defects, especially in the vicinity of step edges. As a consequence, bridges between the metal-organic stripes can occur on a locally non-ideal Fe/Au(111) template, leading to complex 2D patterns as the one depicted in figure 4.12. A remarkable point is that the formation of a bridge between two lines is often related to an opening of one of them, providing a labyrinth-like geometry. The bare Au surface presents free paths through the metal-organic adsorbates and virtual links between distant points are possible. Due to the kinetics of the metal-ligand bonding and the high mobility of TPA, these nano-doors and walls close and open with a time constant of a few minutes at room temperature. The labyrinth structure is thus self-evolving in real-time.

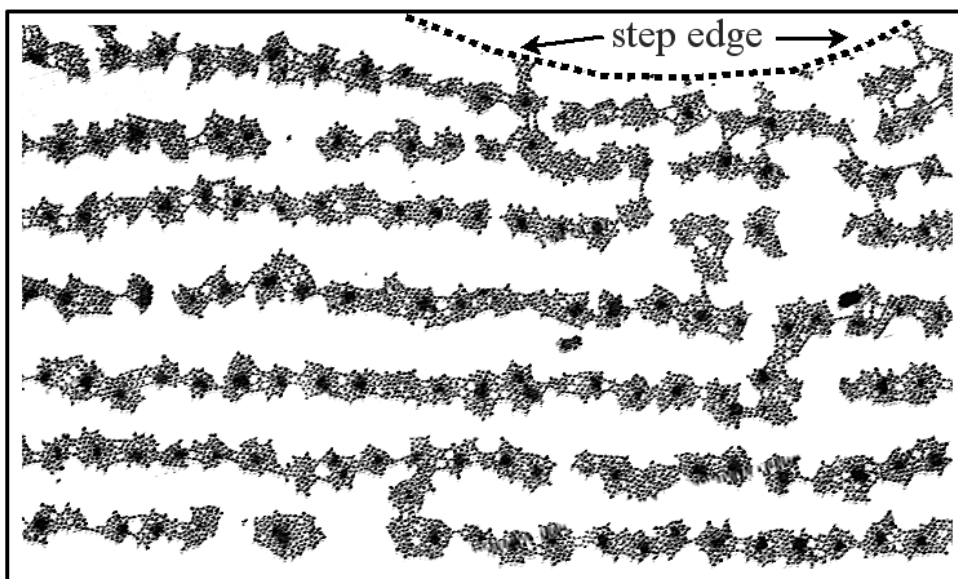


Figure 4.12: Nano-labyrinth. Same preparation conditions as in Fig. 4.10. In the vicinity of step edges and in the presence of defects in the chevron arrangement of the Au(111) reconstruction, a complex two-dimensional structure is formed (STM image size $160 \times 90 \text{ nm}^2$, $I=0.4 \text{ nA}$, $V=-1.5 \text{ V}$, taken at 5 K).

True 1D metallo-molecular link

At a lower total coverage and with inverted deposition order - first TPA, then Co, with the substrate kept at elevated temperature (350 K), true one-dimensional bridges between the metal dots are obtained. Figure 4.13 shows such a structure imaged at room temperature. A few coordinated TPA are linked through a head-to-tail coupling in order to build a mono-molecular bridge. Here again, the patterning of the Au(111) surface is conditioning the metallosupramolecular organization and the formation of the link, as the metal "anchoring pillars" are located at elbow sites of the substrate reconstruction.

The presence of the metal atoms and the coordination linkage is not directly visible (in contrast to the case of the nanogrids, where the structure is characteristic), but it is necessary for the stability of such an isolated structure. A similar line could be possibly obtained by hydrogen bonding but would be unstable and could not be imaged by STM at room temperature. Furthermore, the intermolecular distances are about 5% larger than those in hydrogen bonded domains. This feature thus corroborates the presence of Co atoms in between.

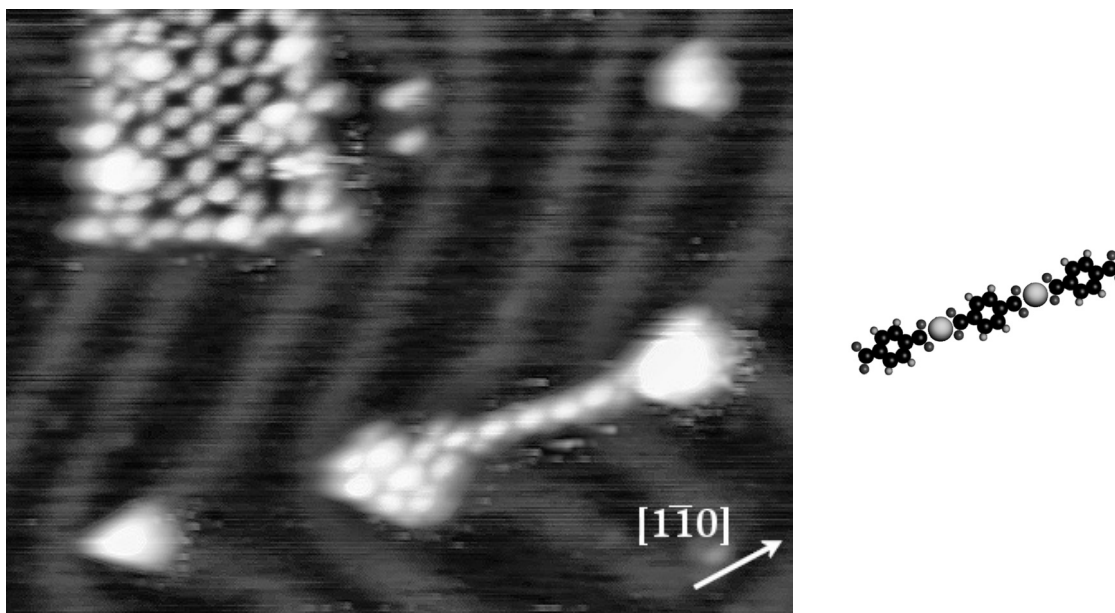


Figure 4.13: Deposition of 0.4 ML TPA followed by deposition of 0.1 ML of Co on Au(111) kept at 350 K. A true 1D metallo-molecular link is formed (STM image size $22 \times 16 \text{ nm}^2$, $I=0.6 \text{ nA}$, $V=-0.7 \text{ V}$, room temperature). On the right the schematics of such a metal-organic chain.

Conclusion

With the system Fe or Co and TPA on the Au(111) surface we demonstrate the formation of metallosupramolecular nanogrids. The appreciable metal-ligand interaction defines its square geometry contrasting with the hexagonal symmetry of the substrate. The dynamics of the formation-dissociation reaction of these coordination compounds can be monitored directly by sequential STM imaging. The dissolution of the metal clusters in the formation of metal-organic nanogrids upon annealing is shown. Metallosupramolecular organization can be steered by using nanostructured templates like the patterned Au(111) surface. The versatility of this approach allows for the formation of various nanoarchitectures, from nanogrids to a mesoscopic ordering and formation of a one-dimensional connection between Co nanoislands.

The respective influence of the ligand and the substrate on the electronic state of the metal centers in these new kind of compounds needs to be characterized. Notably, the magnetic properties of such systems attract particular interest, and the questions of whether a magnetic moment remains on the metal centers and whether a magnetic coupling between them is possible should be elucidated. This is the motivation for the

studies presented in the next chapter. For future perspectives, the electronic properties of the one-dimensional system presented should be investigated, e.g., by scanning tunneling spectroscopy (STS), in particular to try to find out whether conduction along the line and electron delocalization is obtained, as it is the case in similar 1D metallic systems on surfaces [186,187]. Furthermore, the nanolabyrinth described above could be used for percolation studies or investigations on the diffusivity of adsorbed species along random 2D paths [188].

Chapter 5

Electronic and Magnetic State of Metal Centers in Surface-Supported Coordination Architectures

As the dimensions of structures made of bulk magnetic material are drastically reduced in size, the question of the magnetic order remaining at finite temperature is raised. The elucidation of this problem has far reaching consequences both on the theoretical understanding of magnetism and on magneto-recording technologies. Low dimensional magnetic structures like colloids [189], 2D clusters [190], 1D nanowires [191] or even single atoms on metal surfaces [192] exhibit very different properties compared with 3D bulk materials, e.g., large magnetic moments and high magnetic anisotropy energy. In such structures both the intrinsic magnetic properties and the type of magnetic order depend critically on their size and geometry, as well as their composition. For atomic-scale nanostructures on surfaces, a variety of geometrical arrangements can be obtained either by patterning using self-assembly [180, 189–191, 193, 194], or by sequential manipulation with STM [195, 196]. The advent of new techniques opens up new and exciting ways to generate designed nanostructured materials that show novel functionalities. In particular, crystal engineering of coordination polymers is of great interest because of novel topologies of the compounds and the possibility of manipulating magnetic properties and electrical conductivity [170, 197, 198].

The idea is then to combine coordination chemistry with a nanoscale approach. In con-

trast with previous attempts of organizing *ex situ* synthesized magnetic metal-containing molecular entities at surfaces [57,199,200], the metal-organic structures presented in chapter 4 demonstrate the great flexibility of the *in situ* approach for the fabrication of highly ordered metallocsupramolecular architectures. The micro- and mesoscopic shape, periodicity and symmetry, as well as the ligand functionality are extensively tunable. In such systems nevertheless, a series of important questions remains to be solved. First, the electronic state of the metal center is modified by both the substrate interaction and the coordination with the ligand, and needs to be investigated. Second, due to the periodicity of the structures, a coupling between the magnetic centers may occur, mediated either by the electronic states of the molecule or by the substrate electrons. In three-dimensional coordination compounds the electronic properties of the metal centers has been widely explored and characterized [170,181,197,201–205]. There the metal-organic complexes appear in the form of isolated ions, where the charge is usually balanced by the presence of surrounding counterions. The oxidation state of the metal ion is thus related to its coordination and to the global charge of the complex. At metal surfaces the situation is different. The charge on both the metal and the ligand is strongly affected by the presence of the electrons in the conduction band of the substrate, which effectively screen any charged adsorbate. The complex should therefore not be considered as an ion but rather as a neutral species partly hybridized with the substrate. Moreover, the planar arrangement and symmetry, which are influencing to a large part the electronic state, are usually not encountered in three dimensions. The determination of the oxidation state of the central atom in surface-supported coordination compounds thus requires special consideration in comparison with 3D compounds.

The magnetic and electronic states of the metal center in surface-supported coordination structures have been investigated here for the first time by X-ray Absorption Spectroscopy (XAS) and X-ray Magnetic Circular Dichroism (XMCD). Our findings show that the electronic state is dominated by the coupling to the ligand rather than to the substrate. This opens a great variety of options to effectively modify the valence state and magnetic moment of transition metal centers at surfaces. By an appropriate choice of the ligand, its functionality, and the resulting topographic structure [59,130], it may thus become possible to finely tune the electronic properties of the metal center. This is similar to what is done in 3D coordination chemistry where the number of the various

combinations metal-ligand-structure is quasi infinite. Further experiments with different substrates and molecular functionalities are planned to test this hypothesis.

5.1 XAS and XMCD Spectroscopy

General considerations

Synchrotron radiation in the soft X-ray range allows access to the strong dipole-permitted (core $2p \rightarrow$ valence $3d$) excitations in transition-metal ferromagnets, and (core $3d, 4d \rightarrow$ valence $4f$) in rare-earth magnetic materials. For transition metals, L-edge XAS is highly sensitive to the number and configuration of $3d$ electrons, hence to the spin state and oxidation state [206,207]. Since the development of high-resolution synchrotron radiation sources in the relevant energy range, it has successfully been used to study the electronic structure and symmetry of coordination compounds [201,202,205] as well as biologically relevant complexes [208–210].

X-ray absorption experiments with polarized light allow to extract a great deal of information on the magnetic state of such systems. After the first practical demonstration of X-ray magnetic dichroism (XMD) using linearly polarized light in 1986 [211], XMD with the "C", i.e., using circularly polarized light, has been developed both experimentally [212] and theoretically [213] into a powerful quantitative magnetometry tool. XMCD is element-specific, has sub-monolayer sensitivity, and can be used to measure magnetization loops. It allows to identify the moment orientation in ultrathin films of magnetic materials and, unique among surface-sensitive magneto-optical techniques, to determine separately the spin and orbital magnetic moments of a given element together with their anisotropies. In order to achieve its high sensitivity, XMCD requires a tunable source of polarized light in the UV - soft X-ray range and an extremely intense photon beam, which can only be obtained in an advanced synchrotron radiation facility.

The emission of electrons resulting from light absorption is the base of the photoabsorption spectroscopy. In the photoelectric effect, an electron in a bound state of a solid is excited into an unbound (free-electron) state by absorption of a photon of energy $\hbar\omega$. The excitation of primary and secondary electrons escaping the solid yields a measurable photocurrent. The electronic transitions involved are closely related to the electronic structure of the sample and to the characteristics of the incident light. The corresponding

transition matrix element comprises the well-known dipole selection rules for the determination of the allowed atomic state excitations [214]. If the initial and final states are represented by $|n, l, l_z, s_z\rangle$ states, the selection rules state: $\Delta l = \pm 1$ (parity), $\Delta l_z = 0, \pm 1$ (angular momentum conservation), and $\Delta s_z = 0$. For core levels which are described in the j - j coupling scheme ($|n, l, j, m_j\rangle$ notation), these rules become: $\Delta j = 0, \pm 1$ (parity), $\Delta m_j = \pm 1$ for circularly polarized light, and $\Delta m_j = 0$ for linearly polarized light.

For $3d$ transition metals the dipole selection rules allow the following transitions:

$$\begin{aligned} \text{K:} \quad & 1s \quad \rightarrow \quad 4p_{1/2} \\ \text{L}_2: \quad & 2p_{1/2} \rightarrow 3d_{3/2}, 4s \\ \text{L}_3: \quad & 2p_{3/2} \rightarrow 3d_{3/2, 5/2}, 4s, \end{aligned}$$

where the subscript indicates the total angular momentum quantum number j .

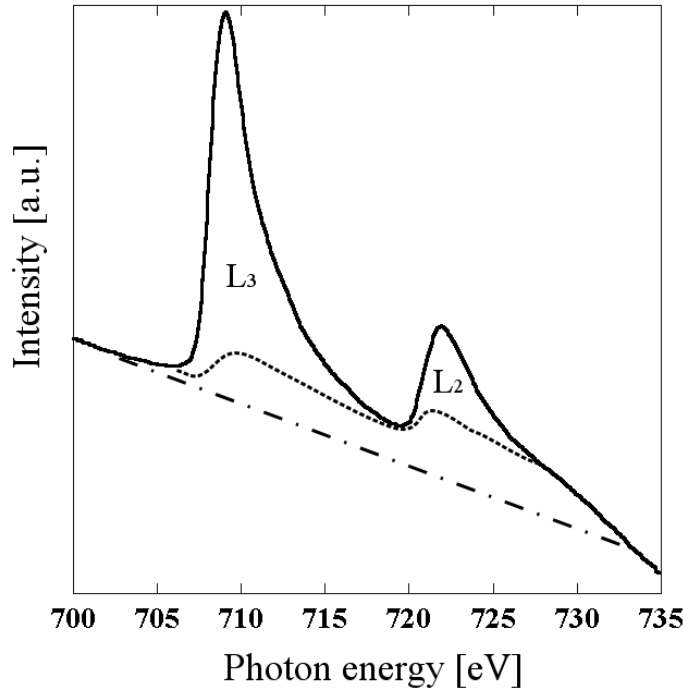


Figure 5.1: XA spectrum of 0.05 ML Fe on Cu(100) at $T=10$ K. The dash-and-dot line schematizes the (unknown) background resulting from lower energy excitations, and the dashed line the contribution due to $2p \rightarrow 4s$ transitions.

Figure 5.1 shows the $L_{2,3}$ absorption edges of a small amount of Fe adsorbed on Cu(100) obtained by measuring the current of the excited photoelectrons as a function of the energy of the incident photons. The ionization thresholds are 707 eV and 721 eV for the L_3 and L_2 core excitations respectively. The dash-and-dot line represents the

background resulting from lower energy excitations. Due to the low peak intensity related to the very low Fe coverage (0.05 ML), the background contribution due essentially to the substrate is substantial. The dashed line schematizes the contribution from the Fe $2p \rightarrow 4s$ transitions; in practice the exact form of this $2p \rightarrow 4s$ threshold is not known, even if smoothed step functions are commonly used in the literature [215] to take it into account. The $p \rightarrow d$ channel, however, largely dominates the spectrum. The sum of the L_2 , L_3 line intensities after the correction for the s transitions is proportional to the number of holes in the $3d$ band.

XMCD effect at the $L_{2,3}$ edges

The absorption of polarized light by a magnetized sample depends on the orientation of the magnetization \mathbf{M} relative to the light polarization direction. XMCD is defined as the difference in the absorption coefficients for parallel and antiparallel orientation of the magnetization direction of the sample with respect to the helicity of the circularly polarized exciting light (see figure 5.2).

Following Stöhr [212], a qualitative understanding of the physics underlying XMCD can be given in the following way: right (R) or left (L) circularly polarized photons are absorbed and transfer their angular momentum ($\Delta m = \pm 1$, respectively) to the excited photoelectron. If the photoelectron originates from a spin-orbit split level, e.g., the $p_{3/2}$ level, the angular momentum of the photon can be transferred in part to the spin through the spin-orbit coupling.¹ R polarized photons transfer the opposite momentum to the electron than L polarized photons, and hence one obtains large transition matrix elements between final states of opposite spin polarization in the two cases. In other words, for a given initial state, R and L polarized photons will excite photoelectrons having opposite spin polarization. Since the $p_{3/2}$ (L_3) and $p_{1/2}$ (L_2) levels have opposite spin-orbit coupling ($l + s$ and $l - s$, respectively), the spin polarization will be opposite at the two edges L_3 , L_2 . The magnetic properties enter in the transition of the excited photoelectron to an unfilled $3d$ -state of the valence band. In the absence of a net magnetization, the number of excited electrons for a given light polarization would be the same for any of the L_3 , L_2 edges

¹The $\Delta S = 0$ selection rule of dipole transitions holds only in the $L - S$ coupling. In the $|nljm\rangle$ base that is used to represent spin-orbit split states, the single particle spin eigenvalue s_z is not a good quantum number. Its expectation value $\langle jm|s_z|jm\rangle$ yields the spin polarization of each state $|jm\rangle$.

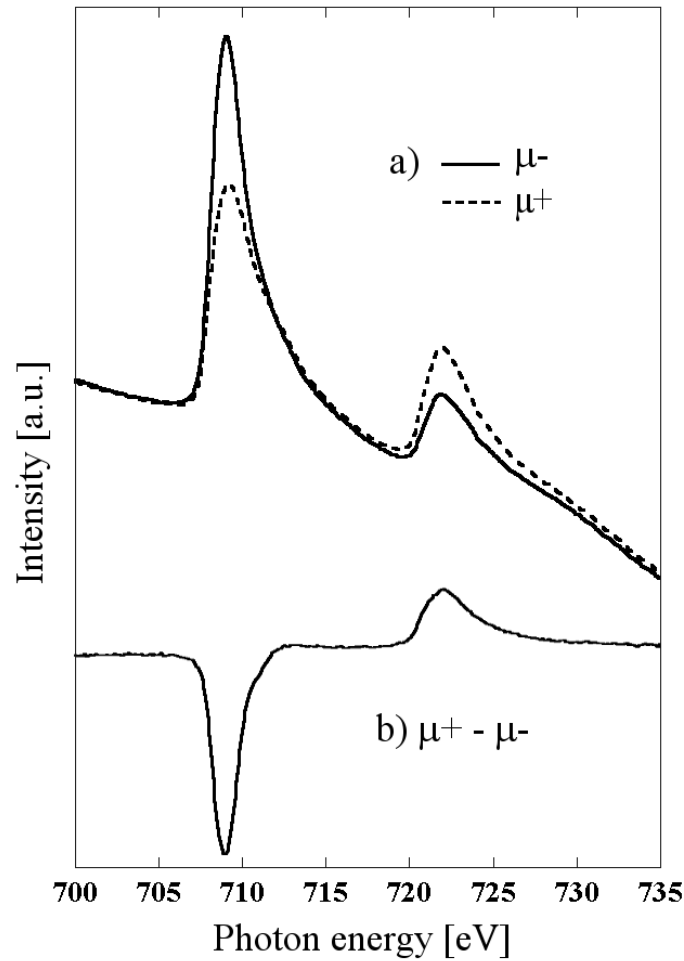


Figure 5.2: $L_{2,3}$ -absorption spectra of 0.05 ML Fe on Cu(100). $T=10$ K, $B=6$ Tesla. (a) Spectra corresponding to parallel (μ^+) and antiparallel (μ^-) orientation of the applied field relative to the polarization of the incident light; (b) XMCD spectrum.

because the total spin polarization for both the $p_{3/2}$ and $p_{1/2}$ manifolds is equal to zero. Suppose now that the $3d$ band is exchange split; the empty states have predominantly minority character. The favored transitions are those that involve the initial states with predominant minority spin character. The exchange split final states therefore act as a filter for the spin of the excited photoelectron. The quantization axis of the filter is given by the magnetization direction which, for maximum dichroism effect, needs to be aligned with the photon spin direction. From the above reasoning it follows that the XMCD signal is proportional to the unbalance between the minority and majority $3d$ states above the Fermi level of the element under consideration, which in turn is proportional to the element

magnetization. The maximum XMCD effect is obtained for a photon helicity parallel to the sample magnetization, thereby allowing to probe its orientation.

XMCD sum rules

Two important magneto-optical sum rules [216–218] relate the XAS and XMCD data to the element-specific orbital and spin magnetic moments. The sum rules have been tested by band-structure calculations [219, 220] and have been verified experimentally [215].

By noting μ^+ and μ^- the absorption coefficients for parallel and antiparallel orientation, respectively, of the sample magnetization relative to the incident light polarization, and in the case of L_3 , L_2 transitions, one calculates the d -shell angular momentum expectation value $\langle L_z \rangle$ as

$$\frac{1}{2n_h} \langle L_z \rangle = \frac{\int_{L_3+L_2} dE(\mu^+ - \mu^-)}{\int_{L_3+L_2} dE(\mu^+ + \mu^- + \mu^0)}, \quad (5.1)$$

where n_h is the number of holes in the d shell, and the denominator term is the normalization to the unpolarized (isotropic) absorption spectrum (μ^0 is the absorption coefficient for linearly polarized light and is usually taken to be the average between μ^+ and μ^-). z refers to the direction of the incident photon beam.

The second rule relates the XMCD signal to expectation values of the spin operator S_z and of the intra-atomic magnetic dipole operator T_z [218]:

$$\frac{2}{3n_h} \left(\langle S_z \rangle + \frac{7}{2} \langle T_z \rangle \right) = \frac{\int_{L_3} dE(\mu^+ - \mu^-) - 2 \int_{L_2} dE(\mu^+ - \mu^-)}{\int_{L_3+L_2} dE(\mu^+ + \mu^- + \mu^0)}. \quad (5.2)$$

The term containing $\langle T_z \rangle$ arises from the multipole expansion of the spin density and depends on the asymmetry of the atomic charge distribution.

The orbital and spin magnetic moments are related to the expectation values of the L_z , S_z operators by

$$\mu_L = -\mu_B \langle L_z \rangle \quad (5.3)$$

$$\mu_S = -2\mu_B \langle S_z \rangle. \quad (5.4)$$

Some ambiguity remains in the integration limits, the background subtraction and in the value to take for n_h when determining the absolute value of μ_L and μ_S . However the ratio μ_L/μ_S^{eff} (where $\mu_S^{eff} = -2\mu_B \langle S_z \rangle - 7\mu_B \langle T_z \rangle$) can be obtained in a straightforward way.

Experimental setup

The experiment described below has been carried out in collaboration with P. Gambardella from the Swiss Federal Institute of Technology in Lausanne and with A. Dmitriev, S. Stepanow and J. Honolka from the Max-Planck-Institute for Solid State Research in Stuttgart, and performed at beam line ID08 of the European Synchrotron Radiation Facility (ESRF) in Grenoble. The samples were prepared *in situ*, characterized by STM and transferred to the XAS/XMCD chamber without breaking the vacuum. A cryomagnet produces a variable ± 6 Tesla magnetic field collinear with the photon beam originating from an undulator source. The Cu(100) sample was cooled to low temperatures by a liquid helium cryostat and could be rotated around the (010) axis with respect to the incident light direction.

5.2 XAS/XMCD of Fe-TPA coordination compounds

The samples used for the XAS/XMCD measurements consist of different metal-organic coordination networks (MOCN) on the Cu(100) surface based on TPA and Fe as a metal center. Similar to the systems Fe/TPA and Co/TPA on Au(111) (see chapter 4), TPA and Fe co-deposited on Cu(100) form large-scale metal-organic architectures. Depending on the stoichiometry, different structures are observed, related to different coordinations of the metal centers. It is thus possible to precisely tailor the local environment of the Fe ions, which makes the system particularly suitable to study their electronic and magnetic response. This system has been previously investigated by STM by M. A. Lingenfelder and S. Stepanow in Stuttgart. A description can be found in Ref. [130], whose relevant parts are summarized in section 5.2.1 below.

The strong multiplet structure observed in the XAS spectra reveals the decisive influence of the ligand field in the electronic ground state of Fe compared to hybridization with the substrate electrons. XMCD data allows to determine the existence of a magnetic moment localized on the Fe atoms. The magnetization curves show a paramagnetic behavior, signaling a negligible or weak magnetic coupling between adjacent Fe centers at temperatures down to about 6 K.

5.2.1 Description of the structures

TPA deposited on the Cu(100) surface form large square domains with a (3×3) superstructure. The coordination structures are obtained by deposition of Fe atoms on top of a TPA precursor layer, followed by annealing at 400 K. The carboxylate groups of the TPA molecules bind to the deposited Fe atoms and well-ordered structures evolve.

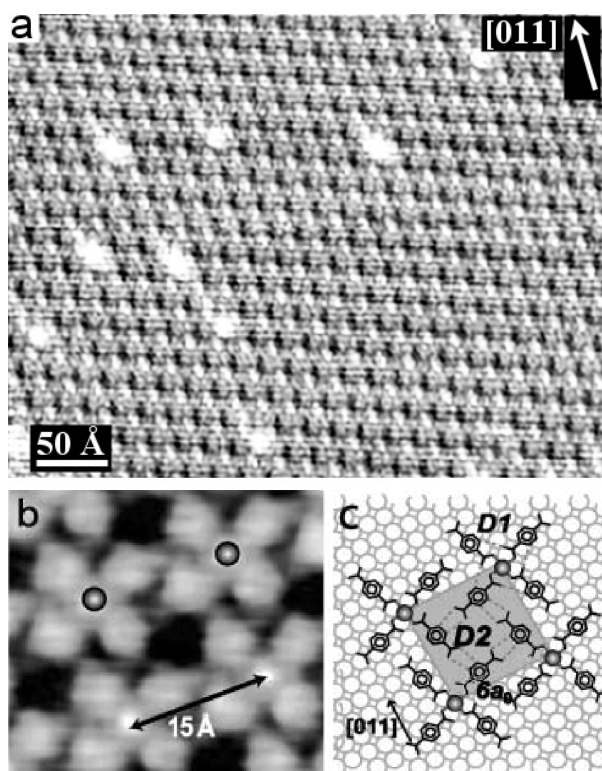


Figure 5.3: a) STM image of the cloverleaf phase of Fe/TPA on Cu(100). b) High-resolution STM image with Fe atoms marked. c) Geometrical model: each Fe atom (gray spheres) coordinates four carboxylate ligands unidentately in a square-planar configuration. The $15\times 15 \text{ \AA}^2$ superstructure unit cell is shown as a gray square (image (a) was acquired *in situ* within the XAS/XMCD setup; b) and c) from [130]).

Cloverleaf phase

This phase is obtained with a Fe:TPA ratio of 0.3. The high-resolution image in figure 5.3 reveals the composition of the individual complexes. The mononuclear complex $[\text{Fe}(\text{TPA})_4]$ consists of a central Fe atom coordinated to four TPA molecules in a square-planar structure by unidentate Fe-carboxylate bonds with an Fe–O distance of approx-

imately 2 Å. In view of the fact that the carboxylate group is a strong hydrogen bond acceptor, the $[\text{Fe}(\text{TPA})_4]$ arrangement may be further stabilized by intracomplex C–H...O hydrogen bonding. The complexes are organized in a (6×6) unit cell with respect to the substrate and form a well-ordered array covering all the terraces of the substrate. A close inspection of the high-resolution image and model reveals that a given TPA molecule in the $[\text{Fe}(\text{TPA})_4]$ complex coordinates to the central Fe atom through the "left-hand" oxygen atom of the carboxylate moiety. $[\text{Fe}(\text{TPA})_4]$ complexes with "right-hand" oxygen coordination are similarly encountered in others domains, which leads to a distinct clockwise or anticlockwise chirality of the complexes.

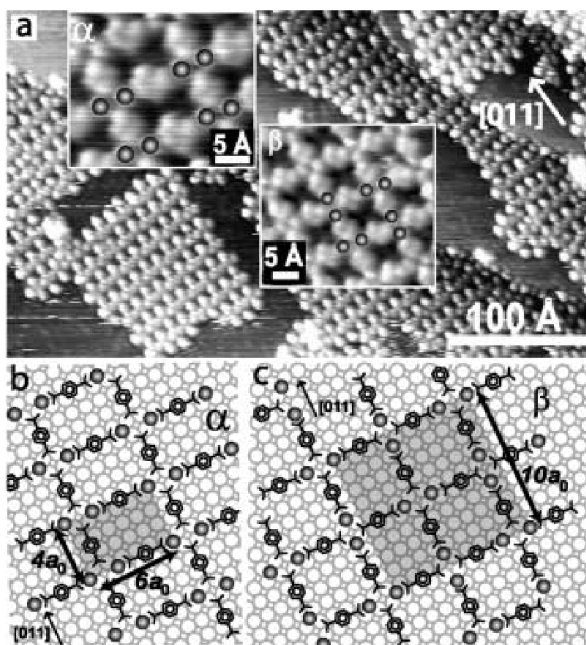


Figure 5.4: a) STM image of the 2D reticulated single-row phase of Fe/TPA on Cu(100), where four TPA are linked to two Fe atoms. High-resolution STM images reveal the geometrical arrangements in the α (upper inset) and β (bottom inset) phases, which differ in the orientation of the neighboring iron pairs. b) and c) Geometrical models depicting atomic and molecular positioning in the two isomeric structures and the corresponding unit cells (from [130]).

Single-row phase

This phase is obtained with a Fe: TPA ratio of 1.2. Here Fe pairs with an Fe–Fe spacing of 5 Å (2 times the substrate atomic periodicity a_0) are linked to four TPA molecules

through Fe–O coordination and organized in a (6×4) (α phase) or (10×10) (β phase) repeat unit (see figure 5.4).

5.2.2 XAS investigations

Figure 5.5 shows the XA spectrum obtained for the cloverleaf phase at 6 K with a normal incident photon beam. The spectrum structure is very different from the case of bulk as well as low-dimensional metallic Fe arrangements [215,221]. Both the L_3 and L_2 white lines show a pronounced multiplet substructure which is absent for equivalent amounts of Fe deposited on pristine Cu(100) at the same temperature (Fig. 5.1). This indicates the dominant influence of ligand fields on the electronic configuration of the Fe centers caused by its coordination to the carboxylate groups. The particular symmetry of the ligand field is decisive for the relative positioning and the splitting of the different energy levels [222]. Depending on its strength, correlations can occur causing inversion of symmetry levels. The resulting complex electronic structure of the multiplet d empty states allows for a series of core excitations at various energies. A broadening of these Dirac-like peaks occurs due to experimental and life-time effects, which results finally in the spectral shape of the data shown in Fig. 5.5.

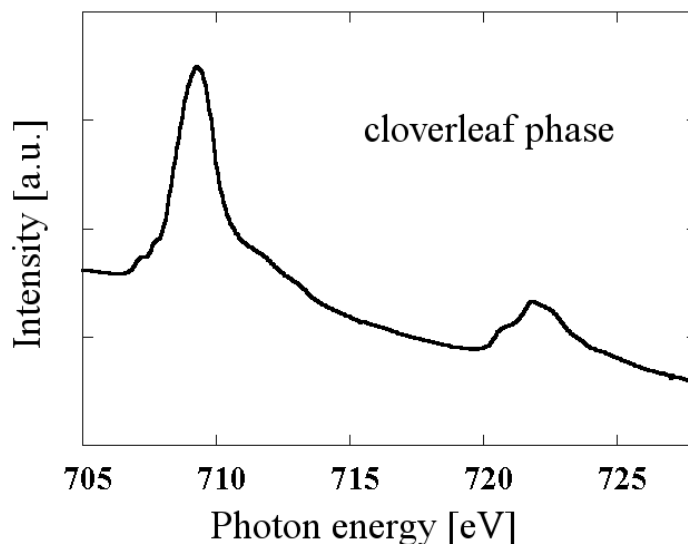


Figure 5.5: XA spectrum of the cloverleaf phase taken at 6 K at normal incidence and for an applied field of 6 Tesla.

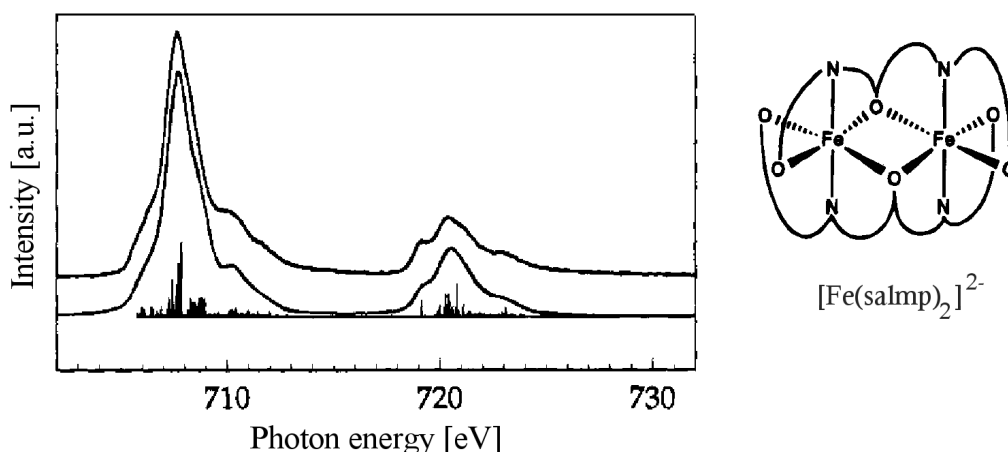


Figure 5.6: Experimental L-edge spectrum (top) together with a theoretical calculation (bottom) for the iron-oxo complex represented schematically on the right. The oxidation state of iron is in this case Fe^{II} (from Ref. [202]).

The XAS multiplet shape is thus a signature of the oxidation state of the metal center and of the symmetry of the complex. By comparing our data with XAS observations reported in the literature for 3D complexes [201,202,205,207,223,224] we can identify cases with similar line shape, as shown, e.g. in figure 5.6. The survey thus suggests that the oxidation state of iron is Fe^{II} . However, 2D and 3D complexes have obviously different symmetries, whence the comparison of the XAS is not fully conclusive. In particular, the planar symmetry of the surface-supported complexes produces an anisotropy in the electronic orbitals. As a consequence, the spectral line shape changes for different incidence angles of the photon beam, as shown for XMCD in figure 5.9. This effect is characteristic of the reduced dimensionality, and is hard to extract with three dimensional samples.

The XAS obtained for the single-row phase is shown figure 5.7. The spectrum exhibits only minor variations with respect to the cloverleaf phase (Fig. 5.5). The coordination of Fe to the oxygen atoms and the symmetry of the complex is in both phases very similar. The qualitative conclusions drawn concerning the electronic and magnetic state are therefore equally valid for both phases.

5.2.3 XMCD investigations

XMCD allows to measure magnetization loops by reporting the intensity of the L_3 peak as a function of the applied field. Our data demonstrates the existence of a magnetic

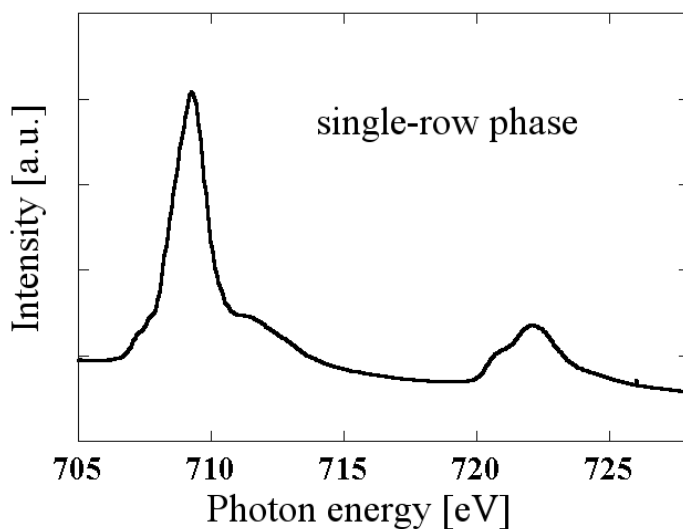


Figure 5.7: XAS spectra of the single-row phase taken at 10 K with a normal incidence for an applied field of 6 T.

moment localized on the Fe atoms. The magnetic response of Fe in the cloverleaf phase is shown in figure 5.8 for two different orientations of the photon beam relative to the sample normal. The magnetization is clearly not fully saturated at 6 Tesla. No hysteresis is found, indicating that there is no ferromagnetic coupling between Fe centers at temperatures down to about 6 K. The comparison of the shape of the magnetization curves for different incidence angles reveals the anisotropy of the magnetic moment. For a finite applied field the sample magnetization is stronger at higher incidence angle. The magnetic easy-axis thus lies close to the surface plane.

The quantitative description of the magnetization behavior is not straightforward and requires a detailed knowledge of the ground state. In a purely atomic case at finite temperature the thermal excitation determines the relative occupancies of the $|3, 2, j, m_j\rangle$ orbitals and the response of the resulting magnetic moment to an applied field follows a Brillouin function (in the case when the lowest energy lying j -level only is filled). In the coordination compound, the atomic Fe orbitals are distorted and partly mixed with the oxygen orbitals, leading to a more complex description of the magnetization as a function of field and temperature [56, 222]. The character of the Fe+TPA ground state depends on the interplay between symmetry and strength of the ligand interaction. Its elucidation by theoretical calculation is currently in progress.

Figure 5.9 shows two XMCD spectra of the same sample acquired with two different

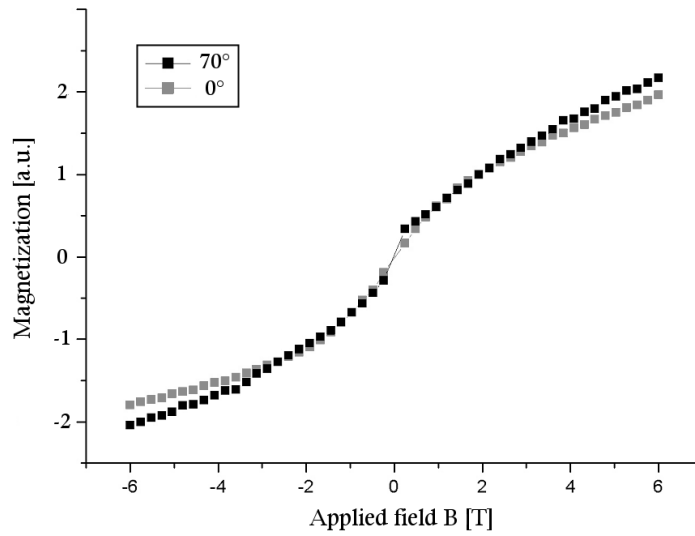


Figure 5.8: Magnetization curves at a temperature of 6 K for two different incident angles of the photon beam, obtained by measuring the intensity of the L_3 peak in function of the applied field. The difference in the two curves is indicative of a magnetic anisotropy. The sample shows a paramagnetic behavior, and is far from the saturation for an applied field of 6 T.

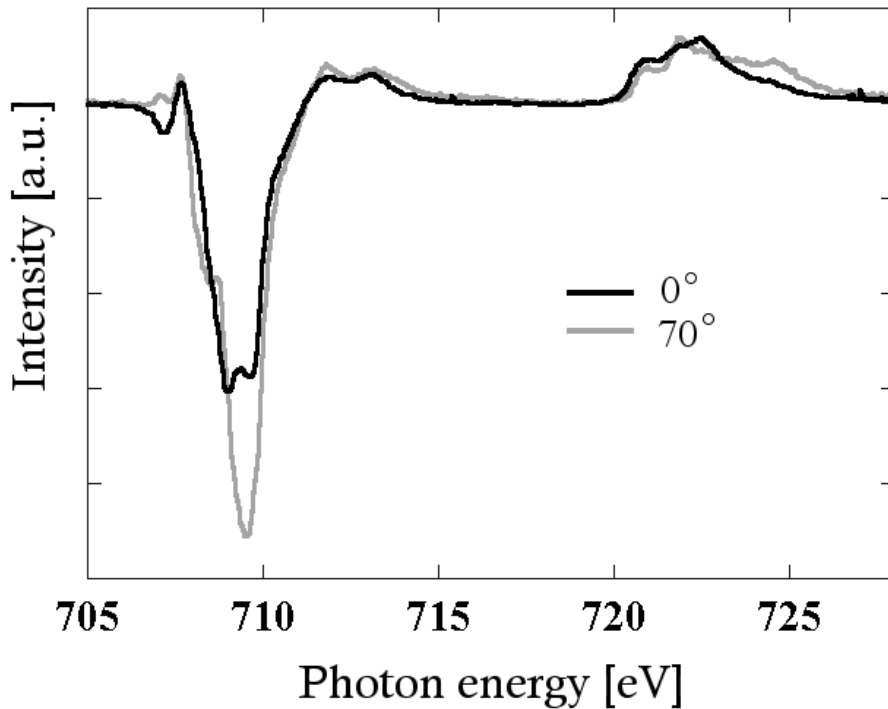


Figure 5.9: Comparison of XMCD spectra of the cloverleaf phase taken at 6 K with an incidence of 0° (normal incidence) and 70° (in plane), for an applied field of 6 T. The difference in the line shapes is due to the anisotropy of the electronic configuration of Fe.

	m_L	$(m_S + m_T)$	$r = \frac{m_L}{m_S + m_T}$
Fe+TPA/Cu(100) out-of-plane	0.32	2.16	0.15
Fe+TPA/Cu(100) in-plane	0.40	1.92	0.20
Fe/Cu(100) out-of-plane			0.13
Fe/Cu(100) in-plane			0.10
Fe/Cu(111) [221]	0.14	1.36	0.10
Fe <i>bcc</i> [225]	0.092	2.08	0.044

Table 5.1: Application of the sum rules of Eq. (5.1) and (5.2) on the Fe+TPA complexes and on pure Fe on Cu(100). For Fe+TPA we assume $n_h = 4$, as for the d^6 configuration expected on the basis of the XMCD line shape. Out-of-plane refers to a normal incidence angle, in-plane to an incidence angle of 70° with respect to the surface normal. The results are compared with previous work on Fe at low coverage on Cu(111) and on bulk Fe. On Cu(100), Fe probably segregates into clusters with possible interpenetration inside the first Cu monolayers. On Cu(111) *fcc* Fe stripes along the step edges are formed. The value of the magnetic moment of Fe in the complexes is comparable to the value in *bcc* bulk.

incidence angles. The line shapes are clearly different due to the anisotropy induced by the planar symmetry of the compounds, an issue which was already addressed in the XAS data. In fact, orienting the photon beam in-plane and out-of-plane probes states with different orbital symmetry (and orbital moment), an effect which is not observed in bulk Fe compounds.

Sum rules

The application of the sum rules as described in section 5.1 for the calculation of the spin moment m_S and the angular moment m_L leads to the values given in table 5.1. The ratio $r = m_L / (m_S + m_T)$ is given to quite a good accuracy. It is indicative of the spin-orbit character of the ground state, i.e., of the contribution of the orbital moment to the magnetic moment. However, the separate evaluation of m_S and m_L is obtained with limited accuracy, because *ad hoc* assumptions are required, such as the number of holes n_h and the value of m_T , and because the data do not correspond to saturation, as for the applied field of 6 Tesla the sample is not fully magnetized.

The values obtained for the coordination compounds are compared with the case of pure Fe on Cu(100), as well as previous work with Fe on Cu(111) and bulk Fe. The value of the magnetic moment of Fe in coordination compounds is therefore comparable to the value in *bcc* bulk. Furthermore, the findings show in first approximation the effect of the dimensionality on the magnitude of the magnetic moment. Fe in 2D clusters on a surface exhibits larger r ratio than in bulk due to the reduced coordination of the Fe atoms in the clusters compared to the bulk. For the coordination complex, where the Fe atoms are truly isolated, the r -ratio is even larger, indicating the presence of a sizeable unquenched orbital moment, as expected for Fe compounds with D_{4h} symmetry [222].

DFT calculations on the TPA single-row phase adsorbed on Cu(100) were performed by A. Seitsonen [148]. The corresponding energetically relaxed model is shown in figure 5.10. Preliminary results show that in comparison with the case of a single isolated Fe atom on Cu(100), its implication in a complex results in an elevation of its position normal to the surface plane of about 0.5 \AA away from the substrate. The metal center is thus more strongly bond to the molecules and physically partly decoupled from the substrate. These findings underline the strength of the metal-ligand bond and thus qualitatively confirm the importance of the ligand coupling for the electronic state of Fe.

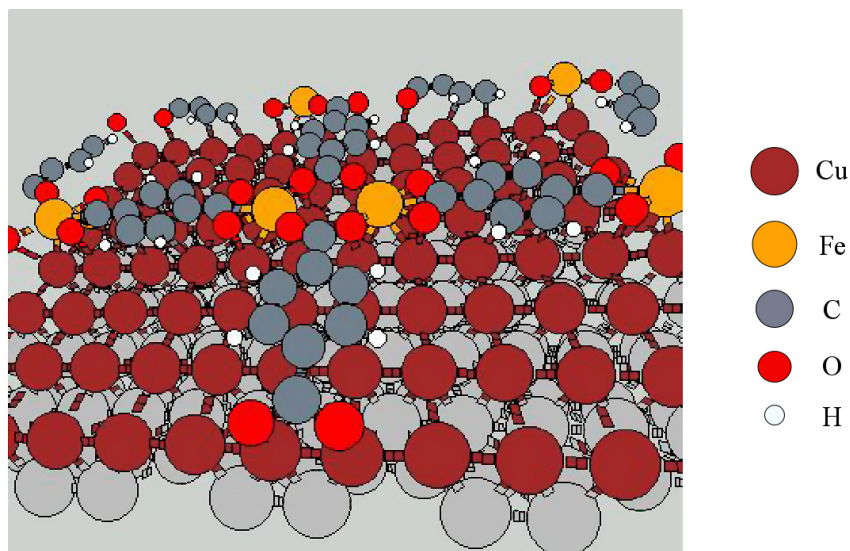


Figure 5.10: Model of the Fe+TPA single-row phase on Cu(100). The relaxation of the structure by means of DFT calculations reveals that Fe atoms are moved away from the surface of about $\sim 0.5 \text{ \AA}$ in comparison with their equilibrium position in the absence of lateral coupling (from Ref. [148]).

Further calculations were performed by the group of Prof. Sarma [226] of the Indian Institute of Science in Bangalore, India, in order to model the spectral line shape obtained experimentally. A theoretical XMCD spectrum was elaborated on the basis of a planar FeO_4 cluster model. The hopping and crystal field parameters were adjusted in order to obtain the best agreement between the calculated multiplet structure and the experimental one. The resulting spectrum is shown in figure 5.11 for the case of a normal incident photon beam. The findings thus implies that the ground state of the Fe centers is of predominant d^6 character and that the oxidation state is Fe^{II} , which is consistent with what can be proposed on the basis of the XAS spectral line shape. Furthermore, they explicitly demonstrate that the multiplet structure observed is due to the coordination to the carboxylate moities.

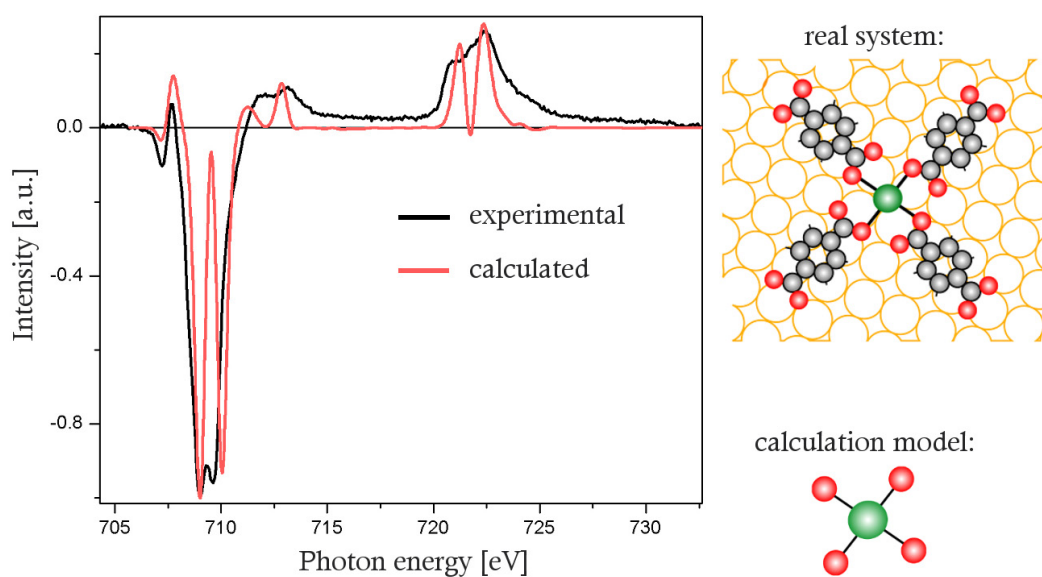


Figure 5.11: Calculated XMCD spectrum for a FeO_4 -cluster model compared with the experimental spectrum obtained on the cloverleaf phase for a normal incident photon beam (Fig. 5.9). The main input parameters are: a Fe^{II} oxidation state, an average occupancy of the $3d$ orbitals of 6.14 for the ground state (d^6 state), a square planar (D_{4h}) symmetry, and an applied field of 6 Tesla; $10D_q=0.5$ eV, $\delta_1=0.15$ eV, $\delta_2=0.10$ eV; the hopping parameters are scaled with respect to FeO hoppings (from Ref. [226]).

In conclusion, we could characterize the oxidation state of metals centers in surface-supported architectures and identify the presence of a magnetic moment localized on the Fe atoms. We have shown that the magnetic behavior and electronic ground state of Fe+TPA deposited on a Cu substrate is primarily determined by the symmetry and nature of the ligand rather than by the metallic substrate. This opens new opportunities to engineer functional coordination architectures at surfaces. Supramolecular chemistry, with its variety of functional bond combinations, can therefore be employed on surface-supported metal-organic compounds to tailor their magnetic and electronic response, similarly to what is done in bulk molecular crystals [56].

Conclusions and Future Directions

In the present thesis Low-Temperature Scanning Tunneling Microscopy (LT-STM) was used to study supramolecular ensembles at well-defined metal surfaces. A major part of the work was dedicated to the design and construction of a new experimental setup. The performance and the excellent stability of the instrument is demonstrated. The investigations presented concern the two-dimensional supramolecular bonding and ordering of terephthalic acid (TPA). The intermolecular interaction is governed by the formation of hydrogen bonds through the dimerization of the carboxyl groups, similar to the bulk crystal phase. The stability of the resulting supramolecular sheet is strongly influenced by the peculiar structure of the surface plane. In the case of Au(111), the surface reconstruction causes distortions in the regular atomic arrangement which are transmitted to the molecular layer. In particular, this induces appreciable variations in the hydrogen bond length, which underlines the versatility of this non-covalent interaction for the formation of supramolecular architectures. In the case of Cu(111) the commensurability to the surface is not strictly possible and defects in the self-assembled layer are created.

Furthermore, we present the formation of surface-supported coordination compounds. By taking advantage of the mesoscopic patterning of the reconstructed Au(111) surface we succeed in creating nanoarchitectures governed by metal-ligand interactions. Nano- and mesoscopic ordering is achieved by metallosupramolecular engineering. In addition, the dynamics of the formation of metallosupramolecular nanogrids could be monitored *in situ*, showing in particular their high thermodynamical stability in comparison with the biphasic system made out of separated metal clusters and molecular 2D gas phase.

These results attest to the usefulness of STM as a tool for elucidating molecule-based nanoarchitectures at surfaces. Its high resolution imaging ability allows for resolving the precise organization of such systems, thus revealing key principles on the delicate balance between molecule-molecule and molecule-substrate interactions which govern supramolec-

ular assemblies on surfaces.

The magnetic and electronic properties of coordination compounds on the Cu(100) surface were investigated by means of X-ray Absorption Spectroscopy (XAS) and X-ray Magnetic Circular Dichroism (XMCD). The oxidation and valence state of Fe in metal-organic compounds could be elucidated, showing the decisive influence of the ligand in the ground state configuration of the metal center. The presence of a magnetic moment located on the Fe atoms and the paramagnetic behavior of the system is demonstrated. This result illustrates the great variety of options to effectively tailor the valence state and magnetic moment of transition metal atoms at surfaces by the choice of appropriate ligands and substrates.

Two principle ways can be envisioned for the further development of supramolecular engineering on surfaces. On the one hand the continuation of structural studies, where the rich arsenal of organic linkers and metals, accumulated by conventional solution and solid state metal-organic chemistry, can be explored to construct novel supramolecular architectures. In particular, the strong directionality of the metal-ligand bond could be exploited further, together with molecules of different symmetry, size and functionality. Furthermore, various kinds of surface pre-patterning can be obtained by stress-induced metallic heteroepitaxial growth [227, 228]. Its utilization for directing supramolecular organization is very encouraging, as was shown with Co and Fe on Au(111). A systematic development of the genuine bottom-up strategy for the fabrication of novel self-assembled structures is in this way expected to provide subtle control over the resulting topologies at the nanoscale.

On the other hand a deeper understanding of the nature of the intermolecular bonds at surfaces can be obtained. For this, the spectroscopic ability of STM can bring precious information on the electronic state of self-assembled systems on a local scale. In particular, inelastic spectroscopy (IETS) could deliver direct insight into the chemical nature of the interactions involved at a single-bond level [229–233]. Moreover, when STM is employed in combination with integral methods like X-ray absorption or X-ray photoemission spectroscopy, a comprehensive description can be gained. Additionally, the determination of the electronic structure, the associated energies and the exact coordination geometries for low-dimensional supramolecular architectures can be rationalized in depth by theoretical calculations [84, 234].

The metal-organic coordination networks presented in chapter 4 and related systems are especially promising for future studies. In particular, their magnetic properties can be better controlled. For the system Fe+TPA on Cu(100), the paramagnetic behavior was shown. However, by an accurate choice of the molecule, the distance between the magnetic centers could be reduced, thus possibly leading to a ferro- or antiferromagnetic coupling. Another solution would be the use of molecular magnets which could mediate magnetic coupling. Furthermore, the electronic properties of the one-dimensional Co-TPA chain need to be investigated in details, by STS and IETS. In addition, the chemical reactivity of the metal centers in coordination networks should be tested for applications in heterogeneous catalysis. Finally, the functionality of the nano-cavities obtained can be further developed in order to use them as chemically active sites for selective guest accommodation.

Supramolecular science at surfaces is thus well positioned at the fertile border between experimental physics, theoretical physics, material science, chemistry and biology. A close interdisciplinary cooperation is required to make this field move forward!

Acknowledgements

I would like to thank my thesis director Prof. Johannes Barth for having given me the opportunity to be his first Ph.D. student. I am very grateful in particular for his involvement in the design of the new setup; his ideas and large competencies have been very useful during my whole thesis work. I would like to thank furthermore Prof. Harald Brune and Prof. Klaus Kern for the collaborations and their implication in the project.

I also want to thank the members of the jury, Prof. Michael Grätzel, Prof. Nacho Pascual and Prof. Louis Porte for judging this thesis.

The whole technical team from the workshops at IPN in Lausanne, Pascal Cattin, Gilles Grandjean, Philippe Guex, Philippe Zürcher, André Guisolan, Claude Blanc, Philippe Cordey, Martial Doy, José Grandjean and Michel Fazan as well as Wolfgang Stiepany from MPI in Stuttgart are gratefully acknowledged. Their respective skills have been really appreciated and the quality of their work was decisive for the construction of the experimental setup. Thanks also to Claire-Lise Bandelier, André Schläfli, Françoise Jenny and Florence Choulat for the administrative support.

The synchrotron measurement week at ESRF became even pleasant thanks to the presence of Pietro Gambardella, Sasha Dmitriev, Sebastian Stepanow and Jan Honolka, as well as our local contacts Peter Bancock and Stefan Stanescu. Thanks in particular to Pietro for his powerful skills on magnetism and X-ray things. I would also like to thank Ari Seitsonen of the University Zürich for the DFT calculations, as well as my best assistant Stéphane Pons with whom I made all the STM measurements in Lausanne.

Getting to know about STM and nanoscience was done thanks to many other colleagues at IPN, among which Imad Arfaoui, Tristan Cren, Katharina Franke, Sarah Longwitz, Stefano Rusponi, Nicolas Weiss and my office mates Marta Cañas, Erik Delvigne, Christian Klinke and Agustín Schriffrin. A special thank you goes to Olga for her help in the English language.

Finally I would like to thank my family and friends who successfully managed to give me regular and highly appreciated visits during my whole stay in Lausanne.

Bibliography

- [1] C. M. Niemeyer, *Angew. Chem. Int. Ed.* **40**, 4128 (2001).
- [2] P. Moriarty, *Rep. Prog. Phys.* **64**, 297 (2001).
- [3] J.-M. Lehn, *Supramolecular Chemistry* (VCH, Weinheim, 1995).
- [4] T. A. Jung, R. R. Schlittler, and J. K. Gimzewski, *Nature* **386**, 696 (1997).
- [5] M. Böhringer, K. Morgenstern, W.-D. Schneider, R. Berndt, F. Mauri, A. de Vita, and R. Car, *Phys. Rev. Lett.* **83**, 324 (1999).
- [6] J. V. Barth, J. Weckesser, C. Cai, P. Günter, L. Bürgi, O. Jeandupeux, and K. Kern, *Angew. Chem. Int. Ed.* **39**, 1230 (2000).
- [7] T. Yokoyama, S. Yokoyama, T. Kamikado, Y. Okuno, and S. Mashiko, *Nature* **413**, 619 (2001).
- [8] M. Schunack, L. Petersen, A. Kühnle, E. Laegsgaard, I. Stensgaard, I. Johannsen, and F. Besenbacher, *Phys. Rev. Lett.* **86**, 456 (2001).
- [9] F. Rosei, M. Schunack, P. Jiang, A. Gourdon, E. Laegsgaard, I. Stensgaard, C. Joachim, and F. Besenbacher, *Science* **296**, 328 (2002).
- [10] K. W. Hipps, L. Scudiero, D. E. Barlow, and J. M. P. Cooke, *J. Am. Chem. Soc.* **124**, 2126 (2002).
- [11] J. A. Theobald, N. S. Oxtoby, M. A. Phillips, N. R. Champness, and P. H. Beton, *Nature* **424**, 1029 (2003).
- [12] G. P. Lopinski, D. J. Moffatt, D. D. Wayner, and R. A. Wolkow, *Nature* **392**, 909 (1998).

- [13] A. Kühnle, T. R. Linderoth, B. Hammer, and F. Besenbacher, *Nature* **415**, 891 (2002).
- [14] J. V. Barth, J. Weckesser, G. Trimarchi, M. Vladimirova, A. de Vita, C. Cai, H. Brune, P. Günter, and K. Kern, *J. Am. Chem. Soc.* **124**, 7991 (2002).
- [15] T. Zambelli, J. V. Barth, J. Wintterlin, and G. Ertl, *Nature* **390**, 495 (1997).
- [16] G. A. Somorjai, *J. Phys. Chem. B* **106**, 9201 (2002).
- [17] M. Dürr, A. Biedermann, Z. Hu, U. Höfer, and T. F. Heinz, *Science* **296**, 1838 (2002).
- [18] G. S. MacCarty and P. S. Weiss, *J. Phys. Chem. B* **106**, 8005 (2002).
- [19] W. Ho, *J. Chem. Phys.* **117**, 11033 (2002).
- [20] X.-C. Guo and R. J. Madix, *J. Phys. Chem. B* **107**, 3105 (2003).
- [21] M. O. Lorenzo, C. Baddeley, C. Muryn, and R. Raval, *Nature* **404**, 376 (2000).
- [22] J. Wintterlin, *Adv. Catal.* **45**, 131 (2000).
- [23] J. S. Lindsey, *New J. Chem.* **15**, 153 (1991).
- [24] G. M. Whitesides, P. J. Mathias, and C. T. Seto, *Science* **154**, 1312 (1991).
- [25] M. M. Conn and J. J. Rebek, *Chem. Rev.* **97**, 1647 (1997).
- [26] M. C. T. Fyfe and J. F. Stoddart, *Coord. Chem. Rev.* **183**, 139 (1999).
- [27] G. R. Desiraju, *Crystal engineering : The design of organic solids* (Elsevier, Amsterdam, 1989).
- [28] B. Moulton and M. J. Zaworotko, *Chem. Rev.* **101**, 1629 (2001).
- [29] D. Braga, *Chem. Commun.* **22**, 2751 (2003).
- [30] F. Vögtle, *Supramolecular Chemistry* (Wiley, New York, 1991).
- [31] *Comprehensive Supramolecular Chemistry*, edited by J. L. Atwood, J. E. D. Davies, D. D. MacNicol, F. Vögtle, and J.-M. Lehn (Pergamon, New York, 1996).

- [32] G. A. Jeffrey and W. Saenger, *Hydrogen Bonding in Biological Systems* (Springer, Berlin, 1991).
- [33] L. J. Prins, D. N. Reinhoudt, and P. Timmerman, *Angew. Chem. Int. Ed.* **40**, 2382 (2001).
- [34] J.-H. Fournier, T. Maris, J. D. Wuest, W. Guo, and E. Galoppini, *J. Am. Chem. Soc.* **125**, 1002 (2003).
- [35] T. Kawai, H. Tanaka, and T. Nakagawa, *Surf. Sci.* **386**, 124 (1997).
- [36] M. Furukawa, H. Tanaka, K.-I. Sugiura, Y. Sakata, and T. Kawai, *Surf. Sci. Lett.* **445**, L58 (2000).
- [37] J. Weckesser, A. de Vita, J. V. Barth, C. Cai, and K. Kern, *Phys. Rev. Lett.* **87**, 096101 (2001).
- [38] J. N. O'Shea, J. Schnadt, P. A. Brühwiler, H. Hillesheimer, N. Mårtensson, L. Patthey, J. Krempasky, C. Wang, Y. Luo, and H. Ågren, *J. Phys. Chem. B* **105**, 1917 (2001).
- [39] T.-Q. Nguyen, M. L. Bushey, L. E. Brus, and C. Nuckolls, *J. Am. Chem. Soc.* **124**, 15051 (2002).
- [40] A. McNutt, S. Haq, and R. Raval, *Surf. Sci.* **531**, 131 (2003).
- [41] S. de Feyter and F. C. de Schryver, *Chem. Soc. Rev.* **32**, 139 (2003).
- [42] A. Werner, *Z. Anorg. Chem.* **3**, 267 (1893).
- [43] *Comprehensive Coordination Chemistry*, edited by G. Wilkinson, R. D. Gillard, and J. A. McCleverty (Pergamon, Oxford, 1987).
- [44] B. J. Holliday and C. A. Mirkin, *Angew. Chem. Int. Ed.* **40**, 2022 (2001).
- [45] M. Fujita, *Chem. Soc. Rev.* **27**, 417 (1998).
- [46] B. Olenyuk, J. A. Whiteford, A. Fechtenkötter, and P. J. Stang, *Nature* **398**, 796 (1999).

- [47] M. E. Davis, *Nature* **417**, 813 (2002).
- [48] A. Stein, *Adv. Mater.* **15**, 763 (2003).
- [49] R. Vilar, *Angew. Chem. Int. Ed.* **42**, 1460 (2003).
- [50] V. Balzani, M. Venturi, and A. Credi, *Molecular Devices and Machines* (Wiley-VCH, Weinheim, 2003).
- [51] P. Ball, *Nature* **381**, 648 (1996).
- [52] D. Braga, F. Grepioni, and G. R. Desiraju, *Chem. Rev.* **98**, 1375 (1998).
- [53] J. M. Brown and S. G. Davies, *Nature* **342**, 631 (1989).
- [54] P. Serp and P. Kalck, *Chem. Rev.* **102**, 3085 (2002).
- [55] C. Copéret, M. Chabanas, R. P. Saint-Arroman, and J.-M. Basset, *Angew. Chem. Int. Ed.* **42**, 156 (2003).
- [56] O. Kahn, *Molecular Magnetism* (Wiley-VCH, New York, 1993).
- [57] A. Semenov, J. P. Spatz, M. Möller, J.-M. Lehn, B. Sell, D. Schubert, C. H. Weidl, and U. S. Schubert, *Angew. Chem. Int. Ed.* **38**, 2547 (1999).
- [58] D. G. Kurth, N. Severin, and J. P. Rabe, *Angew. Chem. Int. Ed.* **41**, 3681 (2002).
- [59] S. Stepanow, M. Lingenfelder, A. Dmitriev, H. Spillmann, E. Delvigne, N. Lin, X. Deng, C. Cai, J. V. Barth, and K. Kern, *Nat. Mat.* **3**, 229 (2004).
- [60] C. J. Chen, *Introduction to Scanning Tunneling Microscopy* (Oxford University Press, New York, 1993).
- [61] *Scanning Tunneling Microscopy and Spectroscopy*, edited by D. A. Bonnell (VCH, New York, 1993).
- [62] R. Wiesendanger, *Scanning Probe Microscopy and Spectroscopy* (Cambridge University Press, Cambridge, 1994).
- [63] F. Besenbacher, *Rep. Prog. Phys.* **59**, 1737 (1996).

- [64] S.-W. Hla and K.-H. Rieder, *Annu. Rev. Phys. Chem.* **54**, 307 (2003).
- [65] G. Binnig, H. Rohrer, C. Gerber, and E. Weibel, *Phys. Rev. Lett.* **49**, 57 (1982).
- [66] I. Giaever, *Phys. Rev. Lett.* **5**, 147 (1960).
- [67] J. Bardeen, *Phys. Rev. Lett.* **6**, 57 (1961).
- [68] J. Tersoff and D. H. Hamann, *Phys. Rev. Lett.* **50**, 1998 (1983).
- [69] A. Selloni, P. Carnevali, E. Tosatti, and C. D. Chen, *Phys. Rev. B* **31**, 2602 (1985).
- [70] N. D. Lang, *Phys. Rev. B* **34**, 5947 (1986).
- [71] G. Hörmandinger, *Phys. Rev. B* **49**, 13897 (1994).
- [72] Y. Hasegawa and P. Avouris, *Phys. Rev. Lett.* **71**, 1071 (1993).
- [73] J. K. Gimzewski, E. Stoll, and R. R. Schlittler, *Surf. Sci.* **181**, 267 (1987).
- [74] H. Ohtani, R. J. Wilson, S. Chiang, and C. M. Mate, *Phys. Rev. Lett.* **60**, 2398 (1988).
- [75] P. H. Lippel, R. J. Wilson, M. D. Miller, C. Wöll, and S. Chiang, *Phys. Rev. Lett.* **62**, 171 (1989).
- [76] C. J. Chen, *J. Vac. Sci. Tec. A* **9**, 44 (1991).
- [77] M. Tsukada, H. Kageshima, N. Isshiki, and K. Kobayashi, *Surf. Sci.* **266**, 253 (1992).
- [78] M. Tsukada, K. Kobayashi, N. Isshiki, H. Kageshima, T. Uchiyama, S. Watanabe, and T. Schimizu, *Surf. Sci.* **287**, 1004 (1993).
- [79] G. Doyen, D. Drakova, J. V. Barth, R. Schuster, T. Gritsch, R. J. Behm, and G. Ertl, *Phys. Rev. B* **48**, 1738 (1993).
- [80] P. Sautet and C. Joachim, *Phys. Rev. B* **38**, 12238 (1988).
- [81] R. F. Lin, G. S. Blackmann, M. A. van Hove, and G. A. Somorjai, *Acta Cryst.* **B43**, 368 (1987).
- [82] P. Sautet and C. Joachim, *Chem. Phys. Lett.* **185**, 23 (1991).

- [83] V. Hallmark, S. Chiang, K.-P. Mainhardt, and K. Hafner, *Phys. Rev. Lett.* **70**, 3740 (1993).
- [84] P. Sautet, *Chem. Rev.* **97**, 1097 (1997).
- [85] S. A. Elrod, L. de Lozanne, and C. F. Quate, *Appl. Phys. Lett.* **45**, 1240 (1984).
- [86] O. Marti, G. Binnig, H. Rohrer, and H. Salemink, *Surf. Sci.* **181**, 230 (1987).
- [87] H. F. Hess, R. B. Robinson, R. C. Dynes, J. M. Valles, and J. V. Waszczak, *Phys. Rev. Lett.* **62**, 214 (1989).
- [88] R. Gaisch, J. K. Gimzewski, B. Reihl, R. R. Schlittler, M. Tschudy, and W.-D. Schneider, *Ultramicroscopy* **42-44**, 1621 (1992).
- [89] S. Behler, M. K. Rose, J. C. Dunphy, D. F. Ogletree, M. Salmeron, and C. Chapelier, *Rev. Sci. Instr.* **68**, 2479 (1997).
- [90] A. Hirstein, Ph.D. thesis, École Polytechnique Fédérale de Lausanne, Switzerland, 1998.
- [91] B. C. Stipe, M. A. Rezaei, and W. Ho, *Rev. Sci. Instr.* **70**, 137 (1999).
- [92] L. Petersen, M. Schunack, B. Schaefer, T. R. Linderoth, P. B. Rasmussen, P. T. Sprunger, E. Laegsgaard, I. Stensgaard, and F. Besenbacher, *Rev. Sci. Instr.* **72**, 1438 (2001).
- [93] H.-P. Rust, M. Doering, J. I. Pascual, T. P. Pearl, and P. S. Weiss, *Rev. Sci. Instr.* **72**, 4393 (2001).
- [94] G. Meyer, *Rev. Sci. Instr.* **67**, 2960 (1996).
- [95] SPS-CreaTec GmbH, <http://www.lt-stm.com/>.
- [96] Solidworks software, <http://www.solidworks.com/>.
- [97] Melles Griot, <http://www.mellesgriot.com/>.
- [98] Newport Corporation, <http://www.newport.com/>.

- [99] O. Jeandupeux, L. Bürgi, A. Hirstein, H. Brune, and K. Kern, *Phys. Rev. B* **59**, 15926 (1999).
- [100] S. Pons, P. Mallet, L. Magaud, and J.-Y. Veillen, *Europhys. Lett.* **61**, 375 (2003).
- [101] VAb Vakuumanlagenbau GmbH, <http://www.vab-vakuum.de/>.
- [102] *Turbovac 340M*, Leybold Vakuum GmbH, <http://www.leyboldvac.de/>.
- [103] *St707 strips*, SAES Getter SpA, <http://www.saesgetters.com/>.
- [104] *EFM 3*, Omicron NanoTechnology GmbH, <http://www.omicron.de/>.
- [105] A. Schiffrin, Ph.D. thesis, in prep.
- [106] Cryovac GmbH & CoKG, <http://www.cryovac.de/>.
- [107] Victor Kyburz AG, <http://www.kyburz-sapphire.ch/>.
- [108] Lake Shore Cryotronics, Inc., <http://www.lakeshore.com/>.
- [109] K. Besocke, *Surf. Sci.* **181**, 145 (1987).
- [110] J. Frohn, J. Wolf, K. Besocke, and M. Teske, *Rev. Sci. Instr.* **60**, 1200 (1989).
- [111] Epoxy Technology, <http://www.epotek.com/>.
- [112] Staveley NDT Technologies, <http://www.staveleyndt.com/>.
- [113] California Fine Wire Company, <http://www.calfinewire.com/>.
- [114] Advent Research Materials Ltd, <http://www.advent-rm.com/>.
- [115] S. Behler, M. K. Rose, D. F. Ogletree, and M. Salmeron, *Rev. Sci. Instr.* **68**, 124 (1997).
- [116] RHK Technology, Inc., <http://www.rhk-tech.com/>.
- [117] Nanotec Electronica, <http://www.nanotec.es/>.
- [118] S. D. Kevan and R. H. Gaylord, *Phys. Rev. B* **36**, 5809 (1987).
- [119] M. F. Crommie, C. P. Lutz, and D. M. Eigler, *Nature* **363**, 524 (1993).

- [120] J. Li, W.-D. Schneider, R. Berndt, and S. Crampin, *Phys. Rev. Lett.* **80**, 3332 (1998).
- [121] S. Pons, P. Mallet, and J.-Y. Veuillen, *Phys. Rev. B* **64**, 193408 (2001).
- [122] L. Diekhöner, M. A. Schneider, A. N. Baranov, V. S. Stepanyuk, P. Bruno, and K. Kern, *Phys. Rev. Lett.* **90**, 236801 (2003).
- [123] N. Memmel, *Surf. Sci. Rep.* **32**, 91 (1998).
- [124] O. M. Yaghi, M. O’Keeffe, N. W. Ockwing, H. K. Chae, M. Eddaoudi, and J. Kim, *Nature* **423**, 705 (2003).
- [125] Y.-G. Kim, S.-L. Yau, and K. Itaya, *Langmuir* **15**, 7810 (1999).
- [126] N. Lin, A. Dmitriev, J. Weckesser, J. V. Barth, and K. Kern, *Angew. Chem. Int. Ed.* **41**, 4779 (2002).
- [127] A. Dmitriev, N. Lin, J. Weckesser, J. V. Barth, and K. Kern, *J. Phys. Chem. B* **106**, 6907 (2002).
- [128] S. Griessl, M. Lackinger, M. Edelwirth, M. Hietschold, and W. M. Heckl, *Single Molecules* **3**, 25 (2002).
- [129] A. Dmitriev, H. Spillmann, N. Lin, J. V. Barth, and K. Kern, *Angew. Chem. Int. Ed.* **42**, 2670 (2003).
- [130] M. A. Lingenfelder, H. Spillmann, A. Dmitriev, S. Stepanow, N. Lin, J. V. Barth, and K. Kern, *Chem. Eur. J.* **10**, 1913 (2004).
- [131] B. Bailey and C. J. Brown, *Acta Cryst.* **22**, 387 (1967).
- [132] M. Sledz, J. Janczak, and R. Kubiak, *J. Mol. Struct.* **595**, 77 (2001).
- [133] B. Parker, B. Immaraporn, and A. J. Gellman, *Langmuir* **17**, 6638 (2001).
- [134] J. V. Barth, H. Brune, R. J. Behm, and G. Ertl, *Phys. Rev. B* **42**, 9307 (1990).
- [135] D. S. Martin, R. J. Cole, and S. Haq, *Phys. Rev. B* **66**, 155427 (2002).

- [136] J. V. Barth, J. Weckesser, N. Lin, A. Dmitriev, and K. Kern, *Appl. Phys. A* **76**, 645 (2003).
- [137] F. Mittendorfer and J. Hafner, *Surf. Sci.* **472**, 133 (2001).
- [138] P. A. Redhead, *Vacuum* **12**, 203 (1962).
- [139] S. M. Wetterer, D. J. Lavrich, T. Cummings, S. L. Bernasek, and G. Scoles, *J. Phys. Chem. B* **102**, 9266 (1998).
- [140] A. R. Sandy, S. G. J. Mochrie, D. M. Zehner, K. G. Huang, and D. Gibbs, *Phys. Rev. B* **43**, 4667 (1991).
- [141] S. Narasimhan and D. Vanderbilt, *Phys. Rev. Lett.* **69**, 1564 (1992).
- [142] J. V. Barth, R. J. Behm, and G. Ertl, *Surf. Sci.* **341**, 62 (1995).
- [143] D. Friebel, T. Mangen, B. Obliers, C. Schlaup, P. Broekmann, and K. Wandelt, *Langmuir* **20**, 2803 (2004).
- [144] H. L. Meyerheim and T. Gloege, *Chem. Phys. Lett.* **326**, 45 (2000).
- [145] H. L. Meyerheim, T. Gloege, M. Sokolowski, E. Umbach, and P. Bäuerle, *Europhys. Lett.* **52**, 144 (2000).
- [146] M. Vladimirova, G. Trimarchi, A. Baldereschi, J. Weckesser, K. Kern, J. V. Barth, and A. de Vita, *Acta Mat.* **52**, 1589 (2004).
- [147] S. Clair, S. Pons, A. P. Seitsonen, H. Brune, K. Kern, and J. V. Barth, *J. Phys. Chem. B* (2004), in press.
- [148] A. P. Seitsonen (unpublished).
- [149] G. Kresse and J. Furthmüller, *Phys. Rev. B* **54**, 11169 (1996).
- [150] P. E. Blöchl, *Phys. Rev. B* **50**, 17953 (1994).
- [151] G. Kresse and D. Joubert, *Phys. Rev. B* **59**, 1758 (1999).
- [152] G. R. Desiraju and T. Steiner, *The Weak Hydrogen Bond* (Oxford University Press, Oxford, 1999).

- [153] T. Steiner, *Angew. Chem. Int. Ed.* **41**, 48 (2002).
- [154] G. R. Desiraju, *Acc. Chem. Res.* **35**, 565 (2002).
- [155] H. Spillmann, A. Dmitriev, N. Lin, P. Messina, J. V. Barth, and K. Kern, *J. Am. Chem. Soc.* **125**, 10725 (2003).
- [156] J. V. Barth, R. J. Behm, and G. Ertl, *Surf. Sci. Lett.* **302**, L319 (1994).
- [157] Q. Chen and N. V. Richardson, *Prog. Surf. Sci.* **73**, 59 (2003).
- [158] S. Stepanow, T. Strunskus, M. Lingenfelder, A. Dmitriev, H. Spillmann, N. Lin, J. V. Barth, C. Wöll, and K. Kern, (2004), submitted.
- [159] J. I. Pascual, J. V. Barth, G. Ceballos, G. Trimarchi, A. de Vita, K. Kern, and H.-P. Rust, *J. Chem. Phys.* **120**, 11367 (2004).
- [160] C. C. Perry, S. Haq, B. G. Frederick, and N. V. Richardson, *Surf. Sci.* **409**, 512 (1998).
- [161] M. Wühn, J. Weckesser, and C. Wöll, *Langmuir* **17**, 7605 (2001).
- [162] M. Böhringer, R. Berndt, and W.-D. Schneider, *Phys. Rev. B* **55**, 1384 (1997).
- [163] X. Zhao, Z. Gai, R. G. Zhao, W. S. Yang, and T. Sakurai, *Surf. Sci. Lett.* **424**, L347 (1999).
- [164] X. Zhao, *J. Am. Chem. Soc.* **122**, 12584 (2000).
- [165] Q. Chen, D. J. Frankel, and N. V. Richardson, *Langmuir* **17**, 8276 (2001).
- [166] G. Frenking and N. Fröhlich, *Chem. Rev.* **100**, 717 (2000).
- [167] L. R. MacGillivray, R. H. Groeneman, and J. L. Atwood, *J. Am. Chem. Soc.* **120**, 2676 (1998).
- [168] S. R. Batten and R. Robson, *Angew. Chem. Int. Ed.* **37**, 1460 (1998).
- [169] Y. Cui, O. R. Evans, H. L. Ngo, P. S. White, and W. Lin, *Angew. Chem. Int. Ed.* **41**, 1159 (2002).

- [170] D. Maspoch, D. Ruiz-Molina, K. Wurst, N. Domingo, M. Cavallini, F. Biscarini, J. Tejada, C. Rovira, and J. Veciana, *Nat. Mat.* **2**, 190 (2003).
- [171] C. P. Collier, E. W. Wong, M. Belohradský, F. M. Raymo, J. F. Stoddart, P. J. Kuekes, R. S. Williams, and J. R. Heath, *Science* **285**, 391 (1999).
- [172] G. P. Lopinski, D. D. M. Wayner, and R. A. Wolkow, *Nature* **406**, 48 (2000).
- [173] C. Joachim, C. Gimzewski, and A. Aviram, *Nature* **408**, 541 (2000).
- [174] J. A. Meyer, I. D. Baikie, E. Kopatzki, and R. J. Behm, *Surf. Sci. Lett.* **365**, L647 (1996).
- [175] B. Voigtländer, G. Meyer, and N. M. Amer, *Surf. Sci. Lett.* **255**, L529 (1991).
- [176] D. D. Chambliss, R. J. Wilson, and S. Chiang, *Phys. Rev. Lett.* **66**, 1721 (1991).
- [177] B. Voigtländer, G. Meyer, and N. M. Amer, *Phys. Rev. B* **44**, 10354 (1991).
- [178] J. Repp, F. Moresco, G. Meyer, and K.-H. Rieder, *Phys. Rev. Lett.* **85**, 2981 (2000).
- [179] N. Knorr, H. Brune, M. Epple, A. Hirstein, M. A. Schneider, and K. Kern, *Phys. Rev. B* **65**, 115420 (2002).
- [180] F. Silly, M. Pivetta, M. Ternes, F. Patthey, J. P. Pelz, and W.-D. Schneider, *Phys. Rev. Lett.* **92**, 016101 (2004).
- [181] M. Kurmoo, H. Kumagai, M. A. Green, B. W. Lovett, S. J. Blundell, A. Ardavan, and J. Singleton, *J. Solid State Chem.* **159**, 343 (2001).
- [182] X.-L. Zhou, J. M. White, and B. E. Koel, *Surf. Sci.* **218**, 201 (1989).
- [183] L. C. Cune and M. Apostol, *Phys. Lett. A* **273**, 117 (2000).
- [184] H. Over, Y. D. Kim, A. P. Seitsonen, S. Wendt, E. Lundgren, M. Schmid, P. Varga, A. Morgante, and G. Ertl, *Science* **287**, 1474 (2000).
- [185] J. Wang, C. Y. Fan, Q. Sun, K. Reuter, K. Jacobi, M. Scheffler, and G. Ertl, *Angew. Chem. Int. Ed.* **42**, 2151 (2003).
- [186] T. M. Wallis, N. Nilius, and W. Ho, *Phys. Rev. Lett.* **89**, 236802 (2002).

- [187] S. Fölsch, P. Hyldgaard, R. Koch, and K. H. Ploog, *Phys. Rev. Lett.* **92**, 056803 (2004).
- [188] A. de Vita, private communication.
- [189] V. F. Puntès, K. M. Krishnan, and P. Alivisatos, *Appl. Phys. Lett.* **78**, 2187 (2001).
- [190] S. Rusponi, T. Cren, N. Weiss, M. Epple, P. Bulushek, L. Claude, and H. Brune, *Nat. Mat.* **2**, 546 (2003).
- [191] P. Gambardella, *J. Phys.-Condens. Mat.* **15**, S2533 (2003).
- [192] P. Gambardella, S. Rusponi, M. Veronese, S. S. Dhesi, C. Grazioli, A. Dallmeyer, I. Cabria, R. Zeller, P. H. Dederichs, K. Kern, C. Carbone, and H. Brune, *Science* **300**, 1130 (2003).
- [193] C. T. Black, C. B. Murray, R. Sandstrom, and S. Sun, *Science* **290**, 1131 (2000).
- [194] H. Zeng, J. Li, J. P. Liu, Z. L. Wang, and S. Sun, *Nature* **420**, 395 (2002).
- [195] H. C. Manoharan, C. P. Lutz, and D. M. Eigler, *Nature* **403**, 512 (2000).
- [196] N. Nilius, T. M. Wallis, and W. Ho, *Science* **297**, 1853 (2002).
- [197] B. Moulton, J. Lu, R. Hajndl, S. Hariharan, and M. J. Zaworotko, *Angew. Chem. Int. Ed.* **41**, 2821 (2002).
- [198] H. Srikanth, R. Hajndl, B. Moulton, and M. J. Zaworotko, *J. Appl. Phys.* **93**, 7089 (2003).
- [199] U. Ziener, J.-M. Lehn, A. Mourran, and M. Möller, *Chem. Eur. J.* **8**, 951 (2002).
- [200] A. Cornia, A. C. Fabretti, M. Pacchioni, L. Zobbi, D. Bonacchi, A. Caneschi, D. Gatteschi, R. Biagi, U. del Pennino, V. de Renzi, L. Gurevich, and H. S. J. van der Zant, *Angew. Chem. Int. Ed.* **42**, 1645 (2003).
- [201] F. M. F. de Groot and J. C. Fuggle, *Phys. Rev. B* **42**, 5459 (1990).
- [202] G. Peng, J. van Elp, H. Jang, L. Que, W. H. Armstrong, and S. P. Cramer, *J. Am. Chem. Soc.* **117**, 2515 (1995).

- [203] E. Breuning, M. Ruben, J.-M. Lehn, F. Renz, Y. Garcia, V. Ksenofontov, P. Gütlich, E. Wegelius, and K. Rissanen, *Angew. Chem. Int. Ed.* **39**, 2504 (2000).
- [204] J. R. Galán-Mascarós and K. R. Dunbar, *Angew. Chem. Int. Ed.* **42**, 2289 (2003).
- [205] E. C. Wasinger, F. M. F. de Groot, B. Hedman, K. O. Hodgson, and E. I. Solomon, *J. Am. Chem. Soc.* **125**, 12894 (2003).
- [206] G. van der Laan, B. T. Thole, G. A. Sawatzky, and M. Verdaguer, *Phys. Rev. B* **37**, 6587 (1988).
- [207] G. van der Laan and I. W. Kirkman, *J. Phys.-Condens. Mat.* **4**, 4189 (1992).
- [208] J. M. McCormick, R. C. Reem, and E. I. Solomon, *J. Am. Chem. Soc.* **113**, 9066 (1991).
- [209] S. J. George, J. van Elp, J. Chen, Y. Ma, C. T. Chen, J.-B. Park, M. W. W. Adams, B. G. Searle, F. M. F. de Groot, J. C. Fuggle, and S. P. Cramer, *J. Am. Chem. Soc.* **114**, 4426 (1992).
- [210] H. Wang, G. Peng, L. M. Miller, E. M. Scheuring, S. J. George, M. R. Chance, and S. P. Cramer, *J. Am. Chem. Soc.* **119**, 4921 (1997).
- [211] G. van der Laan, B. Thole, G. Sawatzky, J. B. Goedkoop, J. Fuggle, J. Esteva, R. Karnatak, J. P. Remeika, and H. Dabkowska, *Phys. Rev. B* **34**, 6529 (1986).
- [212] J. Stöhr, *J. Magn. Magn. Mater.* **200**, 470 (1999).
- [213] R. Wu and A. J. Freeman, *J. Magn. Magn. Mater.* **200**, 498 (1999).
- [214] C. Cohen-Tannoudji, B. Diu, and F. Laloë, *Quantum Mechanics* (Wiley, New York, 1997).
- [215] C. T. Chen, Y. U. Idzerda, H.-J. Lin, N. V. Smith, G. Meigs, E. Chaban, G. H. Ho, E. Pellegrin, and F. Sette, *Phys. Rev. Lett.* **75**, 152 (1995).
- [216] B. Thole, P. Carra, F. Sette, and G. van der Laan, *Phys. Rev. Lett.* **68**, 1943 (1992).
- [217] M. Altarelli, *Phys. Rev. B* **47**, 597 (1993).

- [218] P. Carra, B. Thole, M. Altarelli, and X. Wang, *Phys. Rev. Lett.* **70**, 694 (1993).
- [219] R. Wu, D. Wang, and A. Freeman, *Phys. Rev. Lett.* **71**, 3581 (1993).
- [220] R. Wu and A. Freeman, *Phys. Rev. Lett.* **73**, 1994 (1994).
- [221] P. Ohresser, G. Ghiringhelli, O. Tjernberg, and N. B. Brookes, *Phys. Rev. B* **62**, 5803 (2000).
- [222] B. N. Figgis and M. A. Hitchman, *Ligand Field Theory and Its Applications* (Wiley-VCH, New-York, 2000).
- [223] G. van der Laan and B. T. Thole, *Phys. Rev. B* **43**, 13401 (1991).
- [224] J. Lüning, F. Nolting, A. Scholl, H. Ohldag, J. W. Seo, J. Fompeyrine, J.-P. Locquet, and J. Stöhr, *Phys. Rev. B* **67**, 214433 (2003).
- [225] D. Bonnenberg, K. A. Hempel, and H. P. J. Wijn, in *Landolt-Börnstein, New series*, edited by K.-H. Hellwege and O. Madelung (Springer-Verlag, Berlin, 1986), Vol. III/19a, p. 178.
- [226] S. S. Gupta and D. D. Sarma (unpublished).
- [227] H. Brune, M. Giovannini, K. Bromann, and K. Kern, *Nature* **394**, 451 (2000).
- [228] V. Repain, G. Baudot, H. Ellmer, and S. Rousset, *Europhys. Lett.* **58**, 730 (2002).
- [229] B. Stipe, M. Rezaei, and W. Ho, *Phys. Rev. Lett.* **82**, 1724 (1999).
- [230] F. Moresco, G. Meyer, and K.-H. Rieder, *Mod. Phys. Lett. B* **13**, 709 (1999).
- [231] J. I. Pascual, J. J. Jackiw, Z. Song, P. S. Weiss, H. Conrad, and H.-P. Rust, *Phys. Rev. Lett.* **86**, 1050 (2001).
- [232] Y. Kim, T. Komeda, and M. Kawai, *Phys. Rev. Lett.* **89**, 126104 (2002).
- [233] N. Lorente, *Appl. Phys. A* **78**, 799 (2004).
- [234] J. Hafner, *Acta Mat.* **48**, 71 (2000).

Curriculum Vitae

Name: Sylvain Clair

Date of Birth: November 18, 1975

Nationality: French

October 2004 Ph.D. Thesis, EPFL, Lausanne

2001–2004 Research and teaching assistant in the group of Prof. K. Kern at the Institute of Nanostructure Physics of the Swiss Federal Institute of Technology in Lausanne, Switzerland

1999–2000 Civil service as an engineer in the group of Dr. C. Benvenuti at the European Organization for Nuclear Research (CERN) in Geneva, Switzerland

July 1999 Master thesis under the supervision of Prof. P. Schattschneider at the Institute of Applied Physics of the Vienna University of Technology, Austria

1997–1999 Physics degree at the Vienna University of Technology, Austria

1995–1997 Engineering science degree at École Centrale Paris, France

1993–1995 Preparation for competitive entrance examinations to scientific and engineering Grandes Écoles at Lycée Saint-Louis, Paris, France

June 1993 Baccalauréat C series